

MSc: « Photonics and Nanoelectronics »

“Autofocusing accelerating optical beams”

Thesis submitted to the Physics department of University of Crete
in partial fulfillment of the requirements
for the Master Degree in Photonics and Nanoelectronics

IOANNIS FILIPPAKIS

BSc in Electrical and Computer Engineering

University of Crete

Heraklion, Crete

Greece

2015-2016

Approved by:

1. Rakitzis Petros

Associate Professor, Physics Department, UoC

2. Papazoglou Dimitrios

Assistant Professor, Materials Science and Technology Department, UoC

3. Kafesaki Maria

Associate Professor, Materials Science and Technology Department, UoC

Acknowledgements

The completion of this thesis signals the end of my studies for the acquisition of the Master Degree of Science in Photonics and Nanoelectronics at the University of Crete. At the same time, it gives me the opportunity to express my gratitude to all those people who supported me throughout my studies, as well as to those who helped me, both directly and indirectly, to complete my thesis.

First of all, I would like to thank my supervisor, Prof. Dimitrios Papazoglou, for his continuous guidance throughout the conduction of my study. It was a great honor for me to work with Prof. Papazoglou, who apart from being an excellent scientist, distinguished by his special ability to communicate his knowledge to his students; he is also a man of rare quality. In effect, through his profound knowledge, his inspiring comments and his useful advice, he offered me great guidance and at the same time he stimulated my interest in this research area.

I would also like to thank the two other members of the committee of my thesis, Dr. Petros Rakitzis and Dr. Maria Kafesaki.

Thanks go to Attosecond Science Group at IESL Forth Heraklion for the financial support that they offered me throughout of my studies.

Many thanks go to my colleagues and friends from the Master Programme, with whom I shared moments of stress and anxiety, but mostly moments of great joy.

Last but not least, I would like to express my deep gratitude to my parents Stavros and Maria, and especially to my wife Maria, for their love and their support, and for all the great things they have offered me throughout all these years of my studies.

TABLE OF CONTENTS

Abstract

Chapters:

1. Modeling the propagation of optical waves
 - 1.1. Helmholtz equation
 - 1.2. Angular spectrum representation of optical fields
 - 1.3. Paraxial kernel propagator
 - 1.4. Numerical implementation for the modeling of wave propagation in the paraxial regime
 2. Gaussian Beams
 - 2.1. Theory
 - 2.2. Simulating the propagation of Gaussian beams
 3. Simulating the propagation of accelerating Ring –Airy beams
 - 3.1. Theory
 - 3.2. Descretization effects in Ring-Airy propagation
 - 3.3. Ring-Airy propagation in free space
 4. Propagation in the presence of obstacles
 - 4.1. Perfectly absorbing propagation of a Gaussian beam in the presence of a circular block
 - 4.2. Perfectly refracting propagation of a Gaussian beam in the presence of a circular glass
 - 4.3. Perfectly absorbing propagation of a Ring-Airy beam in the presence of a circular block
 - 4.4. Perfectly refracting propagation of a Ring-Airy beam in the presence of a circular glass
 5. Conclusions
- Appendices
- Bibliography

Abstract

Autofocusing accelerating beams are novel optical beams that abruptly autofocus as they propagate. This unique property results from their non-trivial amplitude and phase distribution. Interestingly, although they are diffracting, they inherit some of the attributes of the non-diffracting 1D accelerating beams they originate from. Thus they exhibit self-healing and are able to bypass obstacles, advantages that make them exciting for a broad range of applications such as telecommunications and materials processing.

This thesis focuses on the numerical and theoretical study of the self-healing action of such beams in the presence of refracting and absorbing obstacles. In more detail, the effect of the obstacle size, the effect of the longitudinal obstacle position as well as the effect of the transverse obstacle position are thoroughly analyzed. Finally, the results are compared with those of classical Gaussian beams.

Περίληψη

Οι αυτοεστιαζόμενες, επιταχυνόμενες δέσμες είναι ένας νέος τύπος οπτικών δεσμών που αυτό-εστιάζουν απότομα καθώς διαδίδονται. Αυτή η μοναδική ιδιότητα οφείλεται στην μη τετριμμένη κατανομή πλάτους και φάσης. Είναι ενδιαφέρον ότι αν και περιθλώνται, κληρονομούν μερικά από τα χαρακτηριστικά των 1D επιταχυνόμενων δεσμών Airy από τις οποίες προέρχονται. Έτσι εμφανίζουν αυτο-ίαση και είναι σε θέση να παρακάμψουν εμπόδια, πλεονεκτήματα που τις καθιστούν ενδιαφέρουσες για ένα ευρύ φάσμα εφαρμογών, όπως οι τηλεπικοινωνίες και επεξεργασία υλικών

Η παρούσα εργασία επικεντρώνεται στην αριθμητική και την θεωρητική μελέτη της δράσης της αυτο-ίασης αυτών των δεσμών παρουσία εμποδίων που απορροφούν ή διαθλούν. Αναλυτικότερα, εξετάζεται η επίδραση του μεγέθους καθώς και της θέσης των εμποδίων. Τέλος τα αποτελέσματα συγκρίνονται με αυτά των κλασικών Γκαουσιανών δεσμών.

1. Modeling the propagation of optical waves

1.1 Helmholtz equation

The waves that have a single frequency f are monochromatic waves [8]. As

$$k = \frac{\omega}{c} = \frac{2\pi f}{c} \quad (1.1)$$

the wavelength λ is also fixed. We can write the plane wave solution for monochromatic waves as

$$u(\vec{r}, t) = A(\vec{r}) \cos(\omega t + \Theta(\vec{r})) \quad (1.2)$$

where $A(\vec{r})$ is the amplitude of the wave, and $\Theta(\vec{r})$ is the phase of the wave at \vec{r} . In phasor representation, Equation (1.2) can be written as

$$u(\vec{r}, t) = \text{Re} \left[U(\vec{r}) e^{j\omega t} \right] \quad (1.3)$$

where the phasor $U(\vec{r})$ also called the complex amplitude. The complex amplitude equals $A(\vec{r})e^{j\Theta(\vec{r})}$. We can write Equation (1.3) without explicitly writing the real part for the sake of simplicity as well as simplicity of computation as in the following equation.

$$(\nabla^2 + k^2)U(\vec{r}) = 0 \quad (1.4)$$

where the wavenumber k equals ω/c . The Equation (1.4) called the Helmholtz equation [10]. The Helmholtz equation is valid for all waves satisfying the non-dispersive wave equation.

If $U(\vec{r}, t)$ is not monochromatic, we can write it in terms of its time Fourier transform as

$$U(\vec{r}, t) = \int_{-\infty}^{\infty} U_f(\vec{r}, f) e^{j2\pi ft} df \quad (1.5)$$

where

$$U_f(\vec{r}, f) = \int_{-\infty}^{\infty} U(\vec{r}, t) e^{-j2\pi ft} dt \quad (1.6)$$

1.2 Angular spectrum representation of optical fields

We consider the wave field $U(x, y, z)$ which propagates in the z -direction. For example, $U(x, y, z)$ can be the solution of an optical scattering problem as shown in Figure (1.1)

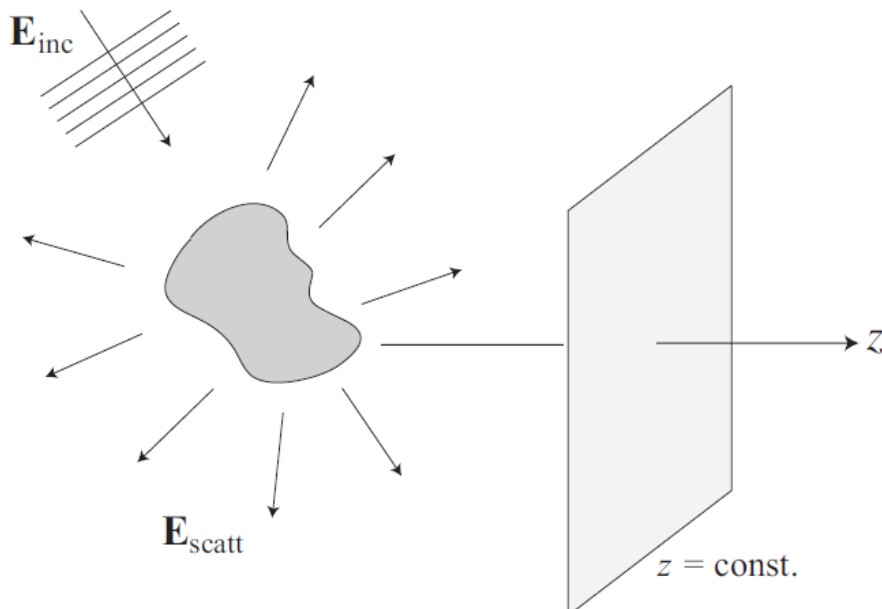


Figure 1.1: In the angular spectrum representation, the fields are evaluated in planes ($z=\text{const.}$) perpendicular to an arbitrarily chosen axis z [11].

Let's assume that the propagation takes place at a wavelength λ such that the wavenumber k equals to $2\pi/\lambda$. If $z = 0$ initially, the 2-D Fourier representation of $U(x,y,0)$ is given in terms of its spatial Fourier transform $A(f_x, f_y, 0)$ by

$$U(x, y, 0) = \iint A(f_x, f_y, 0) e^{j2\pi(f_x x + f_y y)} df_x df_y \quad (1.7)$$

where

$$A(f_x, f_y, 0) = \iint U(x, y, 0) e^{-j2\pi(f_x x + f_y y)} dx dy \quad (1.8)$$

and f_x, f_y are spatial frequencies.

If we include time variation, the plane wave at $z=0$ is given by $A(f_x, f_y, 0) e^{j2\pi(f_x x + f_y y + ft)}$ where $A(f_x, f_y, 0)$ is the angular spectrum of $U(x, y, 0)$.

The angular spectrum $A(f_x, f_y, z)$ of the wave field $U(x, y, z)$ is given by

$$A(f_x, f_y, z) = \iint U(x, y, z) e^{-j2\pi(f_x x + f_y y)} dx dy \quad (1.9)$$

The Fourier representation of the wave field $U(x, y, z)$ in terms of its angular spectrum is given by

$$U(x, y, z) = \iint A(f_x, f_y, z) e^{j2\pi(f_x x + f_y y)} df_x df_y \quad (1.10)$$

$U(x, y, z)$ has to satisfy the vector Helmholtz equation at all points without sources, namely,

$$\nabla^2 U(x, y, z) + k^2 U(x, y, z) = 0 \quad (1.11)$$

where k is determined by $k = (n \cdot \omega / c)$ and $n = (\mu \cdot \epsilon)^{1/2}$ is the index of refraction. Inserting the result of Equation (1.10) into Equation (1.11) we finally find

$$\iint \left[\frac{d^2}{dz^2} A(f_x, f_y, z) + (k^2 - 4\pi^2(f_x x + f_y y)) A(f_x, f_y, z) \right] \cdot e^{j2\pi(f_x x + f_y y)} df_x df_y = 0 \quad (1.12)$$

The previous relationship is true for all waves only if the integrand is zero:

$$\frac{d^2}{dz^2} A(f_x, f_y, z) + (k^2 - 4\pi^2(f_x x + f_y y)) A(f_x, f_y, z) = 0 \quad (1.13)$$

The differential Equation (1.13) has the solution

$$A(f_x, f_y, z) = A(f_x, f_y, 0) e^{j\mu z} \quad (1.14)$$

where

$$\mu = \sqrt{k^2 - 4\pi^2(f_x^2 + f_y^2)} = k_z \quad (1.15)$$

If $4\pi^2(f_x^2 + f_y^2) < k^2$, the μ is then real, and turns the phase factor $e^{j\mu z}$ into an oscillatory function. The wave components satisfying this condition are known as plane waves [8].

If $4\pi^2(f_x^2 + f_y^2) > k^2$, the μ is then imaginary and can be written as

$$\mu = j\sqrt{4\pi^2(f_x^2 + f_y^2) - k^2} \quad (1.16)$$

and Equation (1.14) becomes

$$A(f_x, f_y, z) = A(f_x, f_y, 0) e^{-\mu z} \quad (1.17)$$

This result indicates that the amplitudes of such wave components have an exponential decay along the z axis and are known as evanescent waves.

If $4\pi^2(f_x^2 + f_y^2) = k^2$, $A(f_x, f_y, z)$ is the same as $A(f_x, f_y, 0)$. Such components correspond to plane waves traveling perpendicular to the z-axis.

Hence, we find that the angular spectrum is indeed a superposition of plane waves and evanescent waves. Figure 1.2 shows that the larger the angle between the k -vector and the z axis is, the larger the oscillations in the transverse plane will be. A plane wave propagating in direction of z has no oscillations in the transverse plane $4\pi^2(f_x^2 + f_y^2) = 0$, whereas, in the other limit, a plane wave propagating at a right angle to z shows the highest spatial oscillations in the transverse plane $4\pi^2(f_x^2 + f_y^2) = k^2$. Even higher spatial frequencies can be achieved by evanescent waves. In principle, an infinite bandwidth of spatial frequencies can be achieved. However, the higher the spatial frequencies of an evanescent wave are, the stronger the field decays along the z axis. Thus evanescent waves are not correlated with propagating waves. When studying propagating waves only the finite part of the bandwidth $f_x^2 + f_y^2 \leq \lambda^{-2}$ is important.

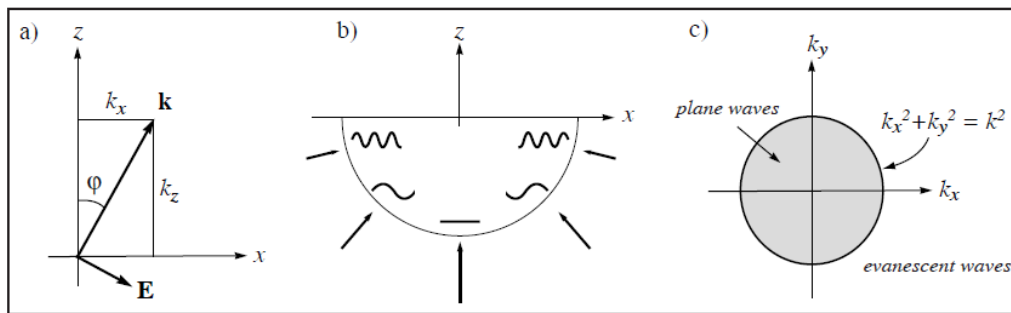


Figure 1.2: a) Representation of a plane wave propagating at an angle φ to the z axis. b) Illustration of the transverse spatial frequencies of plane waves incident from different angles. The transverse wavenumber $[(k_x)^2 + (k_y)^2]^{1/2}$ depends on the angle of incidence and is limited to the interval $[0..k]$. c) The transverse wavenumbers k_x, k_y of plane waves are restricted to a circular area with radius k . Evanescent waves fill the space outside the circle [12].

If we know $A(f_x, f_y, z)$ in terms of $A(f_x, f_y, 0)$, we can find the wave field at (x, y, z) . Inserting the result of Equation (1.14) into Equation (1.10) we finally find:

$$U(x, y, z) = \iint A(f_x, f_y, 0) e^{jz\sqrt{k^2 - 4\pi^2(f_x^2 + f_y^2)}} e^{j2\pi(f_x x + f_y y)} df_x df_y \quad (1.18)$$

Thus, if we know $U(x,y,0)$, we can compute $A(f_x, f_y, 0)$, followed by the computation of $U(x,y,z)$. The limits of integration in Equation (1.18) can be limited to a circular area with radius k given by

$$4\pi^2(f_x^2 + f_y^2) \leq k^2 \quad (1.19)$$

provided that the distance z is at least several wavelengths long so that the evanescent waves may be neglected.

The filter function describes the propagation of an arbitrary spectrum through space [10]. The filter H is an oscillating function for $4\pi^2(f_x^2 + f_y^2) < k^2$ and an exponentially decreasing function for $4\pi^2(f_x^2 + f_y^2) > k^2$. Under these conditions, the filter function is given by

$$H(f_x, f_y) = e^{jz\sqrt{k^2 - 4\pi^2(f_x^2 + f_y^2)}} \text{ for } 4\pi^2(f_x^2 + f_y^2) \leq k^2 \quad (1.20)$$

The propagation of the angular spectrum in the near field as well as the far field describes the propagation of a wavefield in the z -direction in a homogeneous, isotropic, linear and source-free medium.

Let $F[\bullet]$ and $F^{-1}[\bullet]$ denote the forward and inverse Fourier transform operators, respectively. In terms of these operators, Equation (1.18) can be written as

$$U(x, y, z) = F^{-1} \left[F[U(x, y, 0)] e^{jkz\sqrt{1 - a_x^2 - a_y^2}} \right] \quad (1.21)$$

$A(f_x, f_y, 0) = F[U(x, y, 0)]$ is the Fourier transform of $U(x, y, 0)$. It represents the complex envelop of plane wave components at $z=0$ in the directions cosines $a_x = \lambda f_x$, $a_y = \lambda f_y$. The effect of propagation is to modify the relative phases of the various plane waves by a factor $e^{jkz\sqrt{1 - a_x^2 - a_y^2}}$, which is called the transfer function of free space, without changing their amplitudes.

1.3 Paraxial kernel propagator

There are several implementations [8, 9] of the diffraction expressions to simulate optical propagation. These propagation methods are used extensively in research and industry for modeling laser beam propagation. The concentration is on methods that use the fast Fourier transform (FFT) and only monochromatic light will be considered here. When designing a simulation there are a variety of issues related to discrete sampling that need to be considered.

The non-paraxial description of the wave equation is given by the following equation:

$$\nabla^2 U - \varepsilon \cdot \mu \cdot \frac{\partial^2 U}{\partial t^2} = 0 \quad (1.22)$$

The solutions of the previous Equation are linear combinations of plane waves travelling at the speed

$$v = \frac{1}{\sqrt{\varepsilon \cdot \mu}} \quad (1.23)$$

If the Laplacian operator is expanded, it is obtained:

$$\nabla^2 = \left[\frac{\partial^2}{\partial x^2} + \frac{\partial^2}{\partial y^2} + \frac{\partial^2}{\partial z^2} \right] = \left[\nabla_{\perp}^2 + \frac{\partial^2}{\partial z^2} \right] \quad (1.24)$$

where $\nabla_{\perp}^2 \equiv \frac{\partial^2}{\partial x^2} + \frac{\partial^2}{\partial y^2}$ is the transverse part of the Laplacian equation. From equations (1.22), (1.23), (1.24), it is taken

$$\left[\nabla_{\perp}^2 + \frac{\partial^2}{\partial z^2} \right] \cdot U - \frac{1}{v^2} \cdot \frac{\partial^2 U}{\partial t^2} = 0 \quad (1.25)$$

In paraxial approximation the complex magnitude of the electric field $U(x,y,z,t)$ becomes

$$U(x, y, z, t) = f(x, y, z) \cdot e^{jk \cdot n \cdot z - j \cdot \omega t} \quad (1.26)$$

where n is the value of the refractive index, k is the free space wavenumber related to the free space wavelength λ , ω is the angular frequency and the complex valued function $f(x,y,z)$ is a slowly varying function of z on a scale of $1/k \cdot n$. The phase of f describes the departure of the phase front of the wave from that of a plane wave. And

so the longitudinal derivative $\frac{\partial^2}{\partial z^2}$ is equal to:

$$\frac{\partial^2 U}{\partial z^2} = \frac{\partial^2 f}{\partial z^2} \cdot e^{j \cdot k \cdot n \cdot z - j \cdot \omega t} + 2 \cdot j \cdot k \cdot n \cdot \frac{\partial f}{\partial z} \cdot e^{j \cdot k \cdot n \cdot z - j \cdot \omega t} - k^2 \cdot n^2 \cdot f \cdot e^{j \cdot k \cdot n \cdot z - j \cdot \omega t} \quad (1.27)$$

Additionally:

$$\frac{\partial^2 U}{\partial t^2} = \frac{\partial^2 (f \cdot e^{j \cdot k \cdot n \cdot z - j \cdot \omega t})}{\partial t^2} = -\omega^2 \cdot f \cdot e^{j \cdot k \cdot n \cdot z - j \cdot \omega t} \quad (1.28)$$

Substituting (1.26), (1.27) and (1.28) into Equation (1.25), it is obtained the following:

$$\begin{aligned} & \left[\nabla_{\perp}^2 + \frac{\partial^2}{\partial z^2} \right] \cdot f(x, y, z) \cdot e^{j \cdot k \cdot n \cdot z - j \cdot \omega t} + \frac{\omega^2}{v^2} \cdot e^{j \cdot k \cdot n \cdot z - j \cdot \omega t} = 0 \Rightarrow (1.27) \Rightarrow \\ & \left(\frac{\partial^2 f}{\partial x^2} + \frac{\partial^2 f}{\partial y^2} \right) \cdot e^{j \cdot k \cdot n \cdot z - j \cdot \omega t} + \frac{\partial^2 f}{\partial z^2} \cdot e^{j \cdot k \cdot n \cdot z - j \cdot \omega t} + 2 \cdot j \cdot k \cdot n \cdot \frac{\partial f}{\partial z} \cdot e^{j \cdot k \cdot n \cdot z - j \cdot \omega t} - \\ & - k^2 \cdot n^2 \cdot f \cdot e^{j \cdot k \cdot n \cdot z - j \cdot \omega t} + \frac{\omega^2}{v^2} \cdot f \cdot e^{j \cdot k \cdot n \cdot z - j \cdot \omega t} = 0 \Rightarrow \\ & \nabla_{\perp}^2 f + \frac{\partial^2 f}{\partial z^2} + 2 \cdot j \cdot k \cdot n \cdot \frac{\partial f}{\partial z} - k^2 \cdot n^2 \cdot f + \frac{\omega^2}{v^2} \cdot f = 0 \end{aligned} \quad (1.29)$$

The paraxial approximation places certain upper limits on the variation of the amplitude function $f(x,y,z)$ with respect to longitudinal distance z .

A variation of f can be written as: $\delta A = \frac{\partial A}{\partial z} \cdot \delta z \ll A, \delta z \sim \lambda$ (λ is the wavelength) so

that: $\frac{\partial f}{\partial z} \ll \frac{f}{\lambda} \sim k \cdot f$ and also:

$$\frac{\partial^2 f}{\partial z^2} \ll k \cdot \frac{\partial f}{\partial z} \ll k^2 \cdot f \quad (1.30)$$

Because of the paraxial inequalities stated above (1.30), the term $\frac{\partial^2 f}{\partial z^2}$ can be

neglected in comparison to $\frac{\partial f}{\partial z}$. This yields the paraxial approximation of the wave

equation (1.22):

$$\nabla_{\perp}^2 f + 2 \cdot j \cdot k \cdot n \cdot \frac{\partial f}{\partial z} - k^2 \cdot n^2 \cdot f + \frac{\omega^2}{v^2} \cdot f = 0 \quad (1.31)$$

The paraxial kernel propagator is often the approach of choice for simulations since it applies to a wide range of propagation scenarios and is relatively straightforward to compute. A common propagation routine is based on the following equation

$$U(x, y, z) = F^{-1} \left[F[U(x, y, 0)] H(a_x, a_y) \right] \quad (1.32)$$

and uses the transfer function H given by

$$H(a_x, a_y) = \exp \left[-j \left(\frac{\pi}{\lambda} \right) z (a_x^2 + a_y^2) \right] \quad (1.33)$$

where $a_x = \lambda f_x$, $a_y = \lambda f_y$ and z denotes the propagation distance.

As we mentioned in the previous section, the effect of propagation is to modify the relative phases of the various plane waves by a factor

$$e^{jkz\sqrt{1-a_x^2-a_y^2}} \quad (1.34)$$

which is called the transfer function of free space, without changing their amplitudes.

The Equation (1.33) is obtained by the Equation (1.34) if we substitute that $a_x^2 + a_y^2 \ll 1$ and $\sqrt{1-x} \cong 1 - \frac{x}{2}$, $\forall x \ll 1$ and if the term e^{jkz} is ignored. This term is

ignored because it does not affect the transverse spatial structure of the observation plane result.

1.4 Numerical implementation for the modeling of wave propagation in the paraxial regime

In this thesis numerical code was developed in order to estimate the propagation of monochromatic waves using the concept of the angular spectrum in the paraxial approximation regime. The numerical code was implemented in Python, an open source programming language. The python code is given in Appendix B but a short description of its operation will be given here.

The python code that was developed can estimate the propagation of Gaussian or Airy Ring beams in free space or in the presence of obstacles using the concept of the angular spectrum in the paraxial approximation regime. In order to numerically study the effect of obstacles in the propagation of these beams we can use two kinds of obstacles, absorbing and refracting. In the case of absorbing obstacles, the obstacle is a thin piece of circular block. On the other hand in the case of refractive obstacles, the obstacle is a thin piece of circular glass. In this case, we have the capability to change the thickness of the glass through an ini file in order to induce different phase jumps. We can change also the value of the refractive index of the glass. In all cases, we can change the size of every obstacle and its position on the transverse plane (x) and along the propagation axis (z). The values of initial conditions of propagation can be changed through the ini file (wavelength and propagation distance). We can set values also to the number of sampling points in x , y and the propagation z direction. Finally, we can change through the ini file the values of the width of the Gaussian beam and the values of radius, width and exponential decay factor of the Airy Ring beam.

The numerical code that was implemented in Python, takes the source field which is defined in the array DBeam and produces the observation field which is defined in the array PrBeam. The initial beam, after proper manipulation of required values of parameters, is spatially Fourier transformed. The effect of propagation of each plane wave component of the angular spectrum is evaluated by a multiplication by the paraxial Kernel transfer function. The new field is then evaluated by inverse Fourier transforming in space domain.

In the following Figure we present the discretization effects in the cases where the transfer function of an Airy Ring beam with radius which is equal to $r_0=1\text{mm}$, width which is equal to $w_0=0.19\text{mm}$ and exponential decaying factor which is equal to

$a=0.05$ is undersampled ($N_x=N_y=128$) and oversampled ($N_x=N_y=512$). The number of sampling points in the propagation z direction is the same for the two cases and is equal to $N_z=200$.

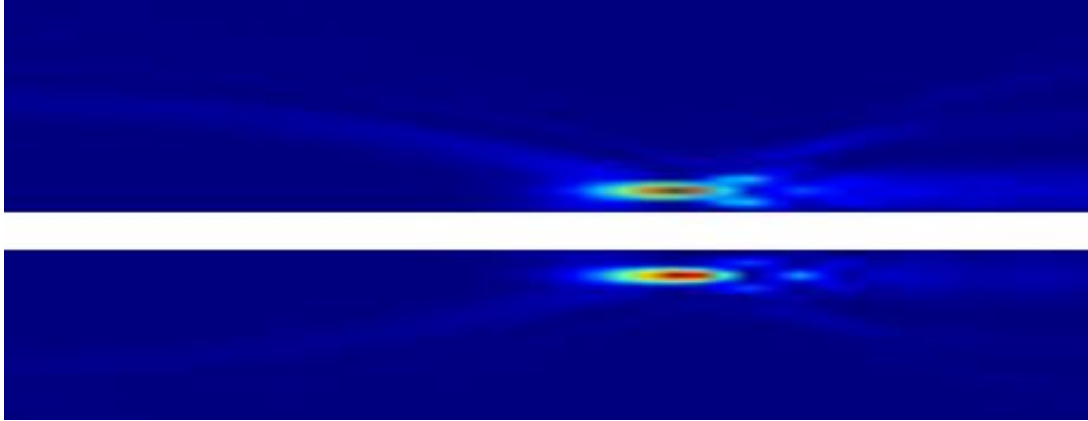


Figure 1.3: Discretization effects in the cases where the transfer function of the Airy Ring is undersampled ($N_x=N_y=128$) and oversampled ($N_x=N_y=512$).

Figure 1.3 depicts the intensity profile of an Airy Ring beam with radius which is equal to $r_0=1\text{mm}$, width which is equal to $w_0=0.19\text{mm}$ and exponential decaying factor which is equal to $a=0.05$ for the case where the transfer function of this beam is under-sampled ($N_x=N_y=128$) and for the case where the transfer function of this beam is oversampled ($N_x=N_y=512$). We observe that in the case where the transfer function of the Airy Ring beam is oversampled, there are some lobes after the focus point of the beam in the propagation direction but in the case where the transfer function of the Airy Ring beam is undersampled, there are not lobes after the focus point of the beam in the propagation direction.

In the following Figure we present the discretization effects in the cases where the transfer function of an Airy Ring beam with radius which is equal to $r_0=1\text{mm}$, width which is equal to $w_0=0.19\text{mm}$ and exponential decaying factor which is equal to $a=0.05$ is under-sampled in the propagation z direction ($N_z=10$) and oversampled in the propagation z direction ($N_z=200$). The number of sampling points in x , y directions is the same for the two cases and is equal to $N_x=N_y=512$.

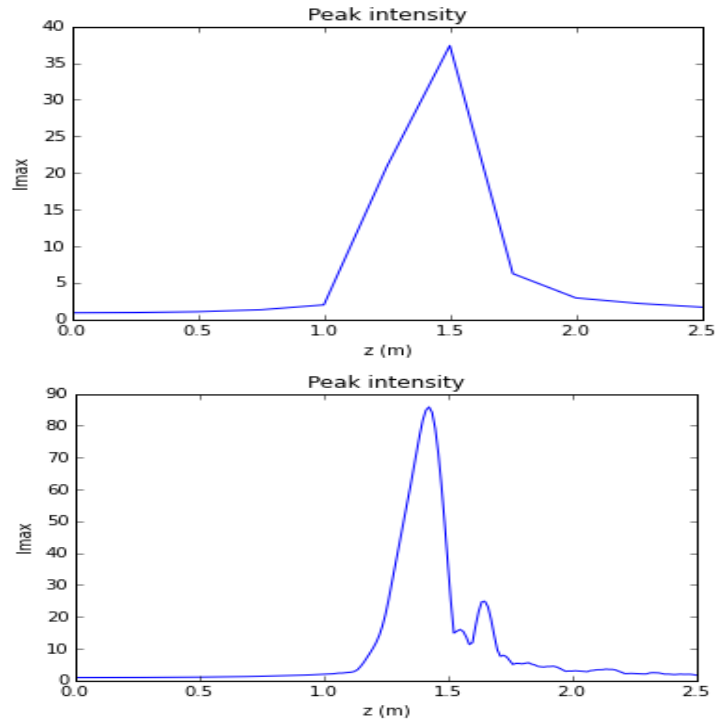


Figure 1.4: Discretization effects in the cases where the transfer function of the Airy Ring is undersampled in the propagation z direction ($N_z=10$) and oversampled in the propagation z direction ($N_z=200$).

Figure 1.4 depicts the maximum intensity profile of an Airy Ring beam with radius which is equal to $r_0=1\text{mm}$, width which is equal to $w_0=0.19\text{mm}$ and exponential decaying factor which is equal to $a=0.05$ for the case where the transfer function of this beam is undersampled in the propagation z direction ($N_z=10$) and for the case where the transfer function of this beam is oversampled in the propagation z direction ($N_z=200$). We observe that in the case where the transfer function of the Airy Ring beam is oversampled in the propagation z direction, the discrepancy between the numerical and the theoretical maximum intensity profile is high but in the case where the transfer function of the Airy Ring beam is under-sampled in the propagation z direction, the discrepancy between the numerical and the theoretical maximum intensity profile is low.

In the following Figure we present the window size effects in the cases where the window size in free propagation simulation of an Airy Ring beam with radius which is equal to $r_0=3\text{mm}$, width which is equal to $w_0=0.07\text{mm}$ and exponential decaying factor which is equal to $a=0.05$, is equal to $W=10\text{mm}$ in the first case and in the second case is equal to $W=20\text{mm}$. The number of sampling points in x, y directions is

is equal to $N_x=N_y=512$ in the first case and equal to $N_x=N_y=1024$ in the second case. The number of sampling points in the propagation z direction is the same for the two cases and is equal to $N_z=200$.

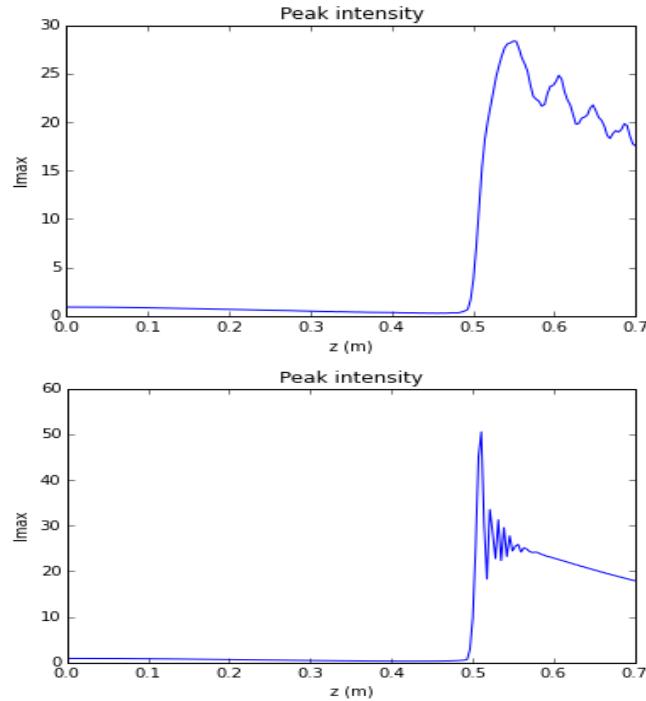


Figure 1.5: Window size effects in the case where the window size in free propagation simulation of the Airy Ring beam is equal to $W=10\text{mm}$ and in the case where the window size is equal to $W=20\text{mm}$.

Figure 1.5 depicts the maximum intensity profile of an Airy Ring beam with radius which is equal to $r_0=3\text{mm}$, width which is equal to $w_0=0.07\text{mm}$ and exponential decaying factor which is equal to $a=0.05$ for the case where the window size in free propagation simulation of the Airy Ring beam is equal to $W=10\text{mm}$ and in the case where the window size is equal to $W=20\text{mm}$. We observe that in the case where the window size in free propagation simulation of the Airy Ring beam is equal to $W=10\text{mm}$, the discrepancy between the numerical and the theoretical maximum intensity profile is high but in the case where the window size is equal to $W=20\text{mm}$, the discrepancy between the numerical and the theoretical maximum intensity profile is low.

2. Gaussian Beams

2.1 Theory

Gaussian beams are a well-known beam of electromagnetic radiation. Their transverse electric field and intensity (irradiance) distributions can be approximated by Gaussian functions. Laser beams are a good approximation of Gaussian beams. They are a solution of paraxial approximation with initial condition for 2 dimensions (for $E(x,y,z)$ being the complex amplitude of beam's electric field and z being the direction of propagation):

$$E(x, y, 0) = E_0 \cdot \exp\left(-\frac{(x^2 + y^2)}{w_0^2}\right)$$

(2.1)

where E_0 is the electric field in the center of the beam and w_0 is the waist of the beam.

For a Gaussian beam, the complex electric field amplitude in homogenous medium is described by the function:

$$E(x, y, z) = E_0 \cdot \frac{w_0}{w(z)} \cdot \exp\left(-\frac{x^2 + y^2}{w^2(z)} - i \frac{\pi}{\lambda} \frac{x^2 + y^2}{R(z)} - i[kz + \psi(z)]\right) \quad (2.2)$$

where the beam waist, the radius of curvature, the Gouy phase and the diffraction length, respectively, are given by:

$$w(z) = w_0 \sqrt{1 + \left(\frac{\lambda z}{\pi w_0^2}\right)^2} = w_0 \sqrt{1 + \left(\frac{z}{z_R}\right)^2} \quad (2.3)$$

$$R(z) = z \left[1 + \left(\frac{\pi w_0^2}{\lambda z} \right)^2 \right] = z \left[1 + \left(\frac{z_R}{z} \right)^2 \right] \quad (2.4)$$

$$\psi(z) = \arctan \left(\frac{\lambda z}{\pi w_0^2} \right) = \arctan \left(\frac{z}{z_R} \right) \quad (2.5)$$

$$z_R = \frac{\pi w_0^2}{\lambda} \quad (2.6)$$

The relationship between all these characteristics of a Gaussian beam is shown in Figure 2.1.

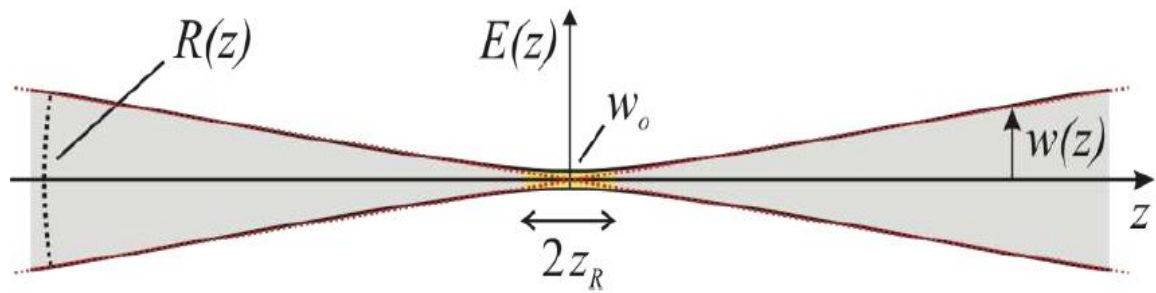


Figure 2.1: Representation of Gaussian Beam [13]

The irradiance distribution of the Gaussian beam is given by:

$$I(x, y, z) = |E(x, y, z)|^2 = I_0 \cdot \exp \left(-\frac{2 \cdot (x^2 + y^2)}{w^2(z)} \right) \quad (2.7)$$

where I_0 is the irradiance in the center of the beam. Usually, the Gaussian shape is truncated at some diameter either by the internal dimensions of the laser beam or by some limiting aperture. In order to discuss the propagation characteristics of a laser beam, it is necessary to define its diameter. There are two ways of defining its diameter, the first one is the diameter at which the beam irradiance (intensity) has fallen to $1/e^2$ (13,5%) of its peak (waist) and the second one is the one at which the

intensity of the beam has fallen to 50% of its peak. The second one is called Full Width at Half Maximum (FWHM).

2.2 Simulating the propagation of Gaussian beams

In order to check the numerical accuracy of the propagation algorithm, which is implemented in Python, we compare the simulation results with the analytical solution of the propagation of the Gaussian beam.

We consider a Gaussian beam with waist $w_0=5\text{mm}$, where $\lambda=0,8\ \mu\text{m}$. The propagation distance z is 400 m. In all our simulations the transverse coordinates (x,y) are discretized to N_x*N_y sampling points while N_z steps are used for the propagation along z direction. The discretization of the propagation problem is listed in Table 2.1.

$N_x=N_y=128,$ $N_z=10$	$N_x=N_y=128,$ $N_z=50$	$N_x=N_y=128,$ $N_z=100$	$N_x=N_y=128,$ $N_z=200$
$N_x=N_y=256,$ $N_z=10$	$N_x=N_y=256,$ $N_z=50$	$N_x=N_y=256,$ $N_z=100$	$N_x=N_y=256,$ $N_z=200$
$N_x=N_y=512,$ $N_z=10$	$N_x=N_y=512,$ $N_z=50$	$N_x=N_y=512,$ $N_z=100$	$N_x=N_y=512,$ $N_z=200$
$N_x=N_y=1024,$ $N_z=10$	$N_x=N_y=1024,$ $N_z=50$	$N_x=N_y=1024,$ $N_z=100$	$N_x=N_y=1024,$ $N_z=200$

Table 2.1: Discretization schemes of the Gaussian beam propagation simulations.

The results of numerical simulation of the propagation of Gaussian beam for all the cases of Table 2.1 are represented in the following Figures.

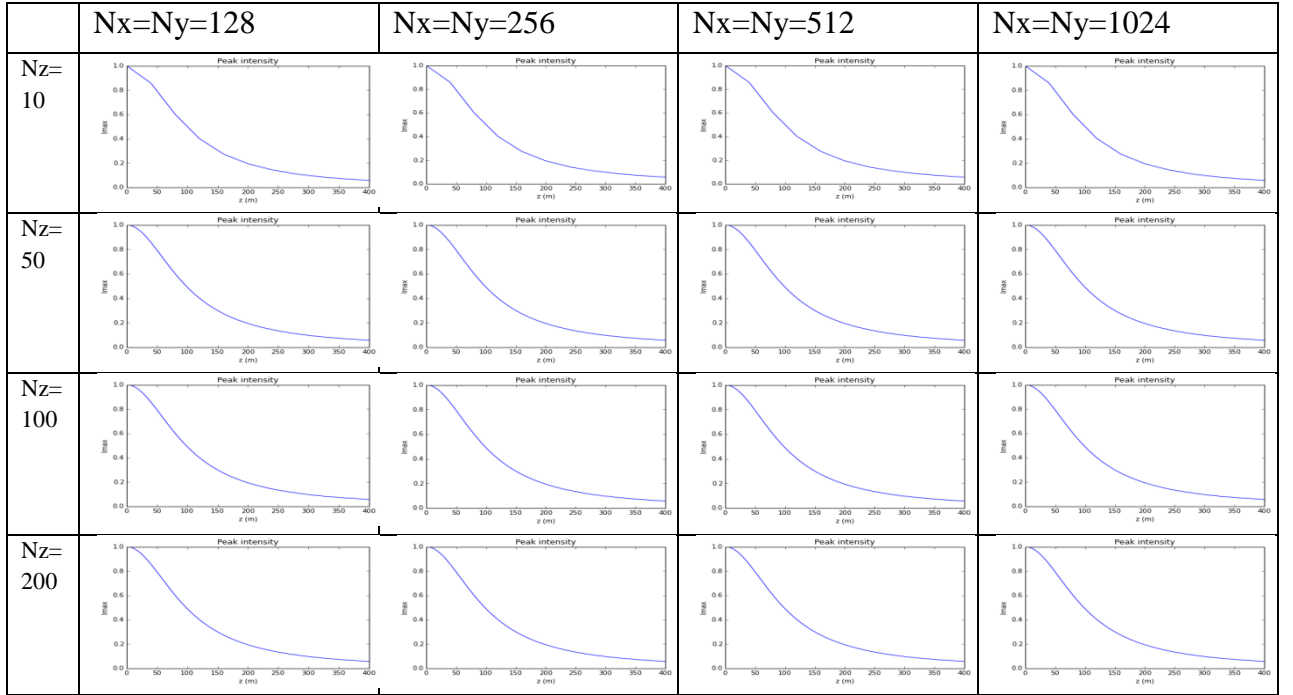


Figure 2.2: Simulated maximum intensity profiles as a function of the propagation distance z for Gaussian beam ($w_0=5\text{mm}$).

Figure 2.2 depicts simulated maximum intensity profiles as a function of the propagation distance z for a Gaussian beam with beam waist which is equal to $w_0=5\text{mm}$, for all the discretization schemes of the Gaussian beam propagation simulations which are listed in Table 2.1. We observe that for lower values of number of sampling points at x , y and propagation z direction, the numerical and the theoretical maximum intensity profiles have large discrepancy. On the other hand, for higher values of number of sampling points at x , y and propagation z direction, the numerical and the theoretical maximum intensity profiles have small discrepancy.

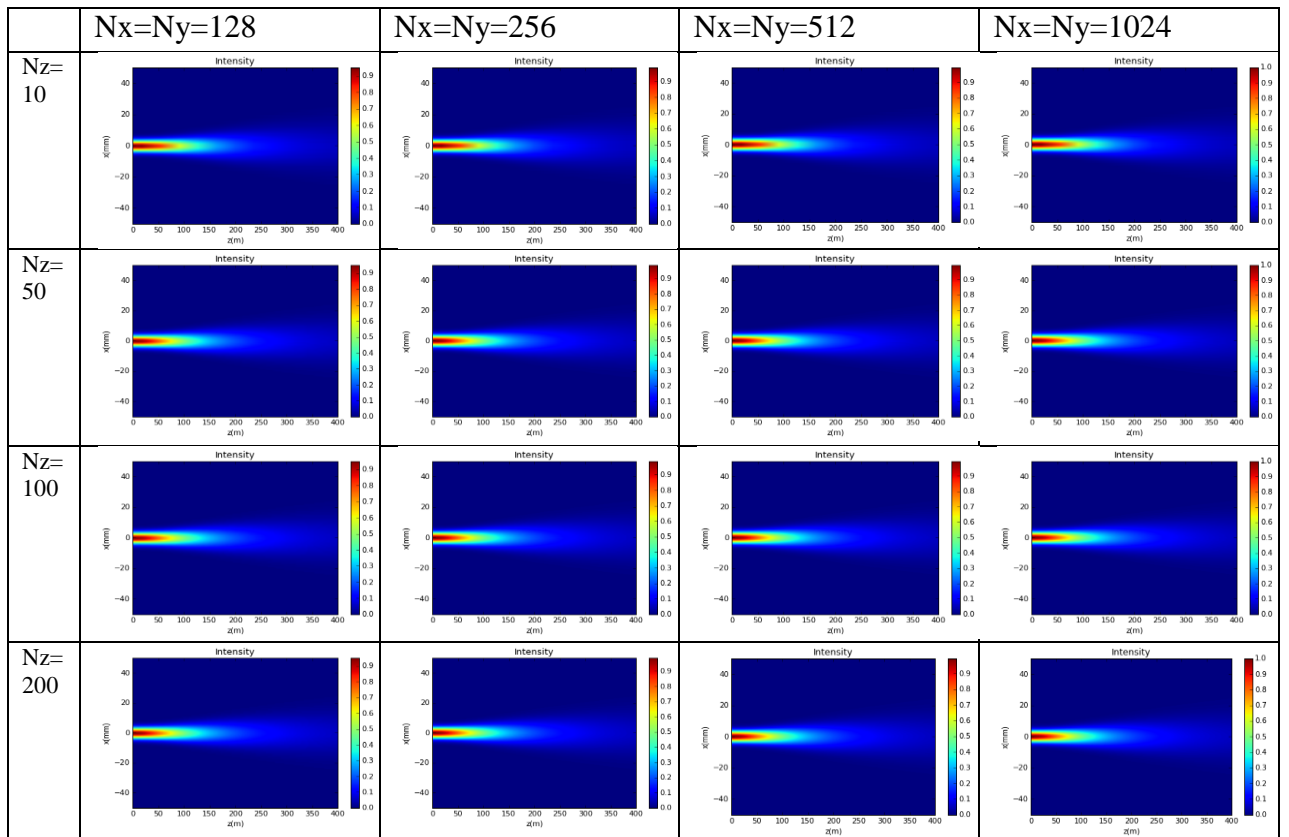


Figure 2.3: Simulated intensity profiles as a function of the propagation distance z for Gaussian beam ($w_0=5\text{mm}$).

Figure 2.3 depicts simulated intensity profiles as a function of the propagation distance z for a Gaussian beam with beam waist which is equal to $w_0=5\text{mm}$, for all the discretization schemes of the Gaussian beam propagation simulations which are listed in Table 2.1. We observe that for all the values of number of sampling points at x , y and propagation z direction, the simulated intensity profiles are little bit the same so the changes are small.

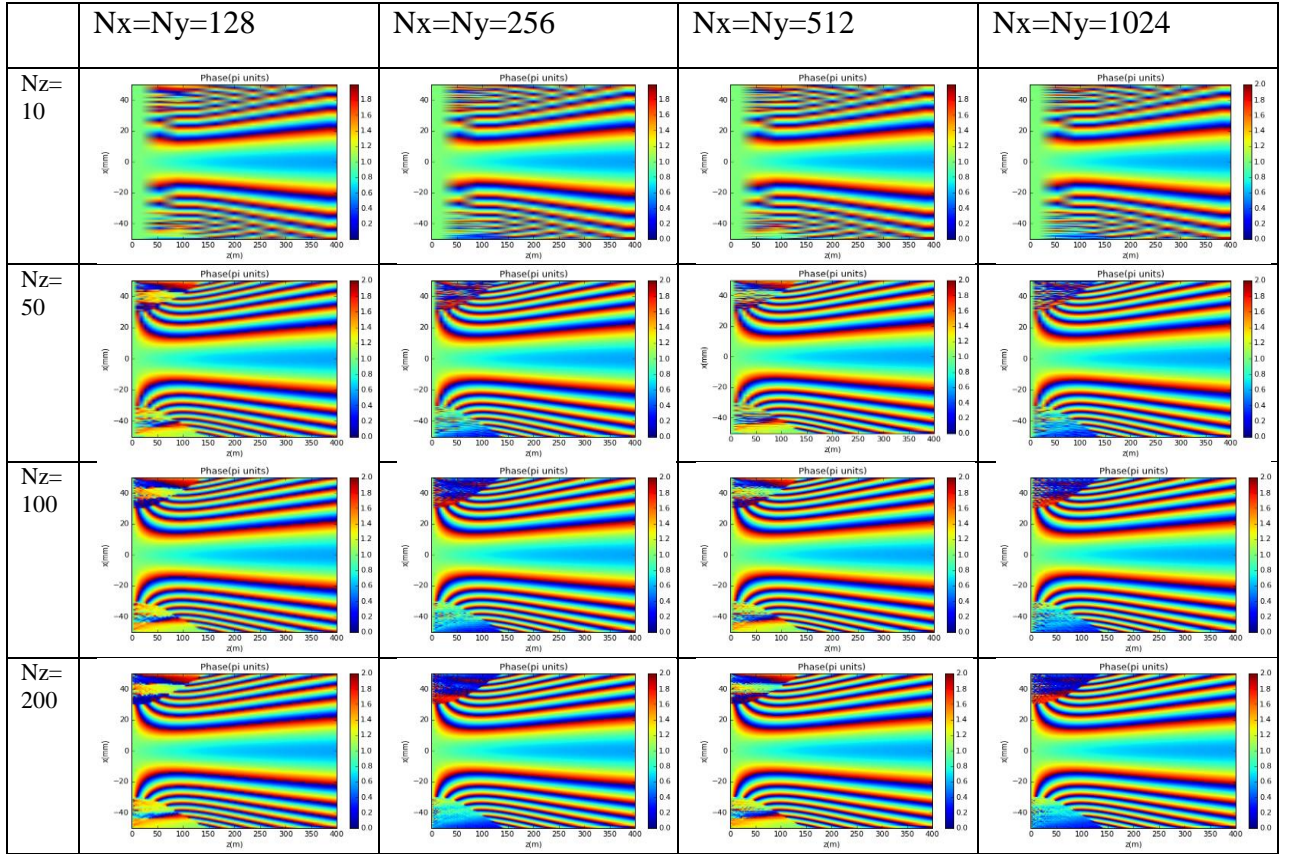


Figure 2.4: Simulated phase profiles as a function of the propagation distance z for Gaussian beam ($w_0=5\text{mm}$).

Figure 2.4 depicts simulated phase profiles as a function of the propagation distance z for a Gaussian beam with beam waist which is equal to $w_0=5\text{mm}$, for all the discretization schemes of the Gaussian beam propagation simulations which are listed in Table 2.1. We observe that for lower values of number of sampling points at x , y and propagation z direction, there are enough artifacts at phase profiles of the Gaussian beam. On the other hand, for higher values of number of sampling points at x , y and propagation z direction, there are not enough artifacts at phase profiles of the Gaussian beam.

In order to check the numerical accuracy of the propagation algorithm we compared the simulation results with the analytical solution of the propagation of the Gaussian beam. The normalized intensity, retrieved from analytic calculations and the numerical simulation, for a Gaussian beam with waist $w_0=5\text{mm}$, for all the cases of Table 2.1, are shown in Figure 2.5.

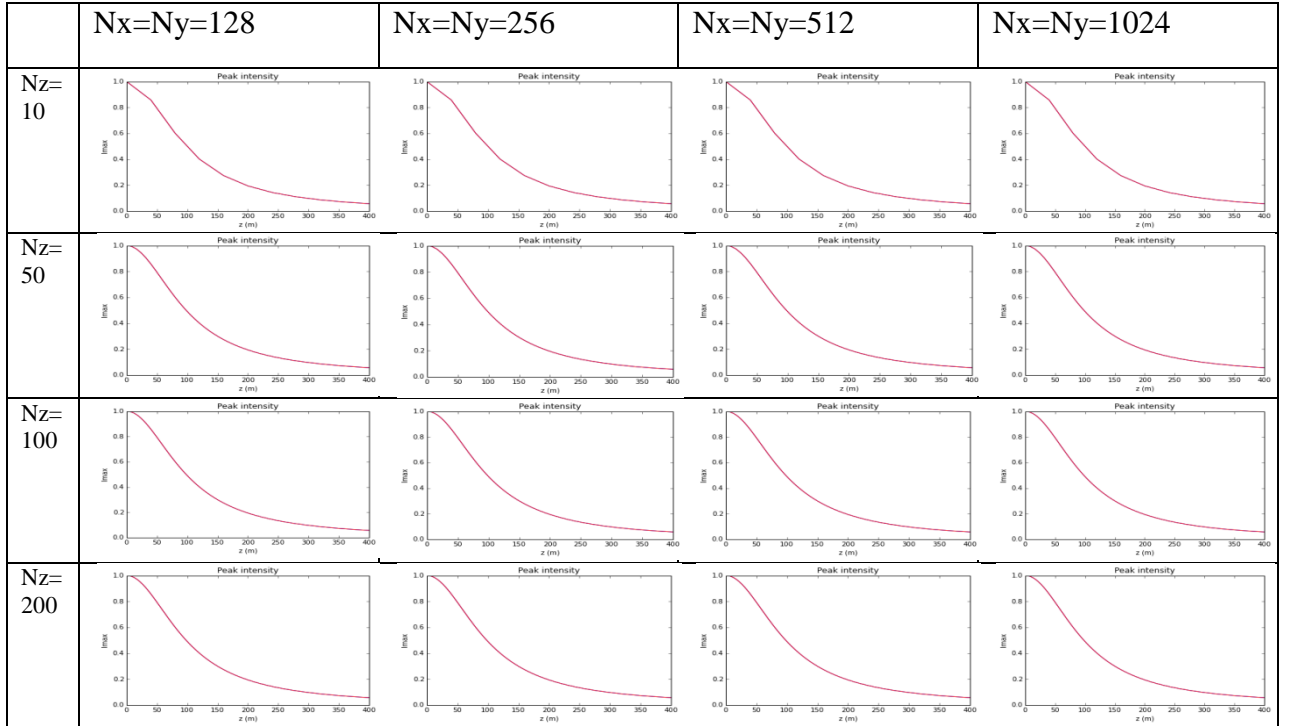


Figure 2.5: Comparison of numerical results retrieved using the propagation code, to analytic prediction for a Gaussian beam with waist $w_0=5\text{mm}$.

Figure 2.5 depicts the normalized maximum intensity profiles, retrieved from analytic calculations and the numerical simulations, for a Gaussian beam with waist $w_0=5\text{mm}$, for all the cases of Table 2.1. We observe that in all cases the discrepancy between the normalized maximum intensity profiles, retrieved from analytic calculations and the numerical simulations is very small.

At following graph (Figure 2.6), we present the results of numerical simulation of the propagation of 3 Gaussian beams with different beam waists ($w_0=5\text{mm}$, $w_0=10\text{mm}$, $w_0=20\text{mm}$) in free space. In these simulations the transverse coordinates (x,y) are discretized to 1024×1024 sampling points while 200 steps are used for the propagation along z direction.

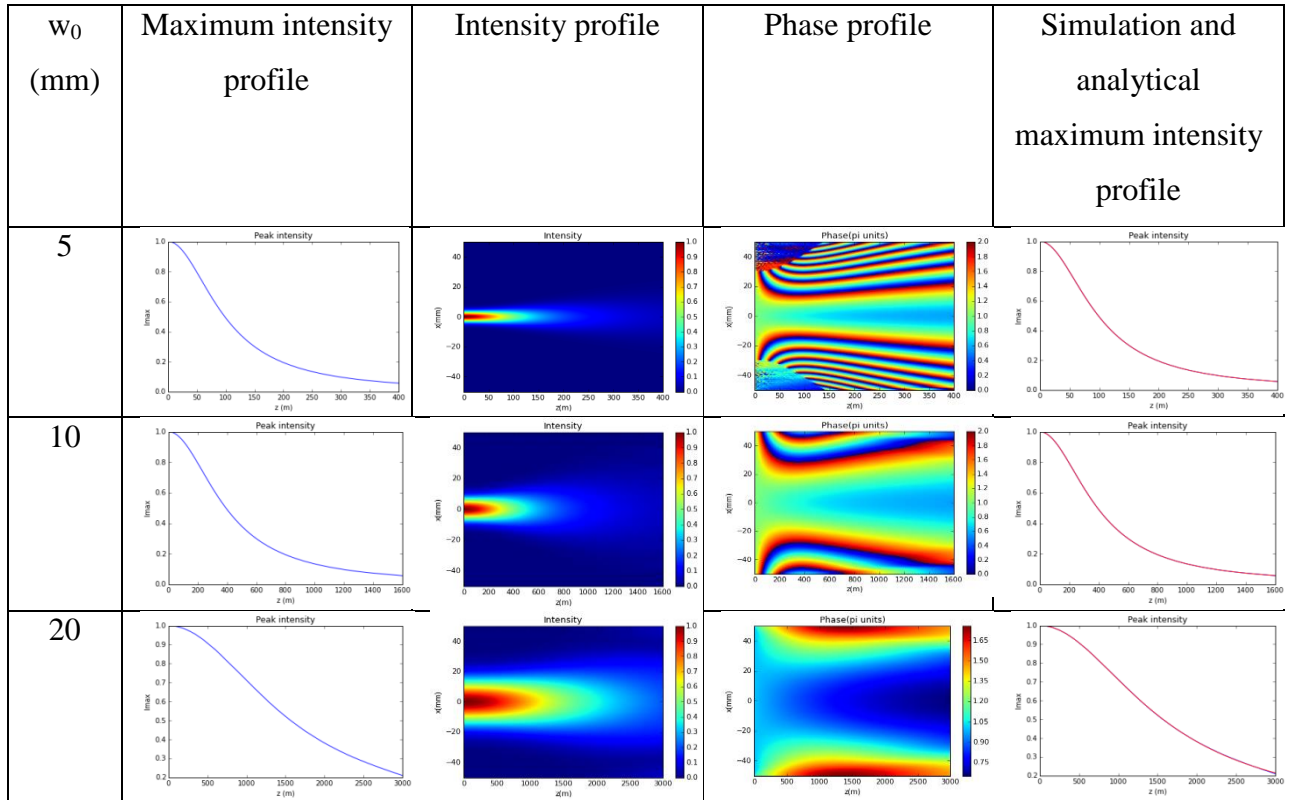


Figure 2.6: The results of numerical simulation for 3 Gaussian beams with different beam waists. ($w_0=5\text{mm}$, $w_0=10\text{mm}$, $w_0=20\text{mm}$).

Figure 2.6 depicts simulated maximum intensity profiles, intensity profiles, phase profiles and the normalized maximum intensity profiles, retrieved from analytic calculations and the numerical simulations as a function of the propagation distance z for 3 Gaussian beams with different beam waists ($w_0=5\text{mm}$, $w_0=10\text{mm}$, $w_0=20\text{mm}$) in free space. The values of the following Table are obtained from the simulation results of this Figure.

Finally, we present the theoretical values of Rayleigh length, the numerical values of Rayleigh length and the percentage change (%) between them for the 3 different Gaussian beams ($w_0=5\text{mm}$, $w_0=10\text{mm}$, $w_0=20\text{mm}$). These values are shown in Table 2.2.

w_0 (mm)	z_R (m) Numerical	z_R (m) Theoretical	Difference (%)
5	98.175	98.125	0.05
10	392.720	392.5	0.056
20	1570.405	1570.0	0.026

Table 2.2: Theoretical values of Rayleigh length, numerical values of Rayleigh length and the percentage change (%) between them for 3 Gaussian beams with different beam waists. ($w_0=5\text{mm}$, $w_0=10\text{mm}$, $w_0=20\text{mm}$).

Table 2.2 depicts the theoretical and numerical values of Rayleigh length and the difference (%) between them for 3 Gaussian beams with different beam waists ($w_0=5\text{mm}$, $w_0=10\text{mm}$, $w_0=20\text{mm}$). We observe that in all cases the numerical and the theoretical values of Rayleigh length have small difference (%) between them which is less than 0.1%.

3. Simulating the propagation of accelerating Ring –Airy beams

3.1 Theory

Airy Ring beams are a recently introduced type of abruptly autofocusing waves [1, 3]. Generally speaking, any beam with proper manipulation of the initial phase or amplitude focuses or scatters and deforms. In some cases, for example in medical use, it's extremely necessary for a beam to focus in a particular target, preserving low intensity before the focus. For this reason, it is important for medical applications to use a new category of optical beams in which the energy flows constantly and with an accelerating way accumulates at the focus point. Airy Ring beams are radially symmetric waves, whose peak intensity remains practically constant during propagation, although, near the focal point, they autofocus and as a result, their maximum intensity can abruptly increase by orders of magnitude just at the focus. In this thesis, the radial Airy profile is used.

The rotationally symmetrical Airy distribution for 2D is represented by:

$$u(r,0) = u_o Ai\left(\frac{r_o - r}{w}\right) \exp\left[\alpha\left(\frac{r_o - r}{w}\right)\right] \quad (3.1)$$

where Ai is the airy function and it is defined i.e. for real values of x by the integral:

$$Ai(x) = \frac{1}{\pi} \cdot \int_0^{\infty} \cos\left(\frac{1}{3} \cdot t^3 + x \cdot t\right) dt \quad (3.2)$$

r_o is the radius of the primary ring, w is a scaling factor and α is the exponential decaying factor.

In the following Figure we present the radial intensity profile of a Ring Airy beam with radius of the primary ring $r_o=1\text{mm}$, scaling factor $w_o=0.13\text{mm}$ and exponential decaying factor $\alpha=0.1$.

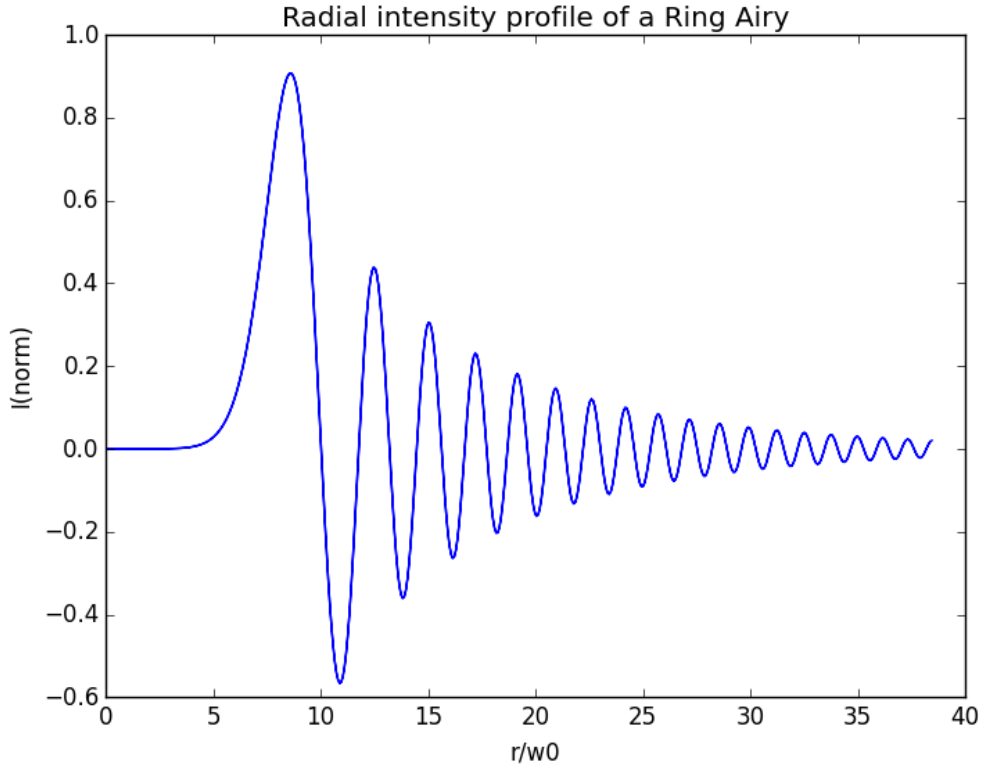


Figure 3.1: Radial intensity profile of a Ring Airy beam with radius $r_0=1\text{mm}$ and the corresponding constants are $w_0=0.13\text{mm}$ and $\alpha=0.1$

3.2 Descretization effects in Ring-Airy propagation

We consider an Airy Ring beam with radius $r_0=1\text{mm}$ and the corresponding constants are $w_0=0.19\text{mm}$ and $\alpha=0.05$, where $\lambda=0.8\ \mu\text{m}$. The propagation distance z is $2.5\ \text{m}$. The discretization of the propagation problem is listed in Table 3.1.

$N_x=N_y=128,$ $N_z=10$	$N_x=N_y=128,$ $N_z=50$	$N_x=N_y=128,$ $N_z=100$	$N_x=N_y=128,$ $N_z=200$
$N_x=N_y=256,$ $N_z=10$	$N_x=N_y=256,$ $N_z=50$	$N_x=N_y=256,$ $N_z=100$	$N_x=N_y=256,$ $N_z=200$
$N_x=N_y=512,$ $N_z=10$	$N_x=N_y=512,$ $N_z=50$	$N_x=N_y=512,$ $N_z=100$	$N_x=N_y=512,$ $N_z=200$

Table 3.1: Discretization schemes of the Airy Ring beam propagation simulations.

The results of numerical simulation of the propagation of Gaussian beam for all the cases of Table 3.1 are represented in the following Figures.

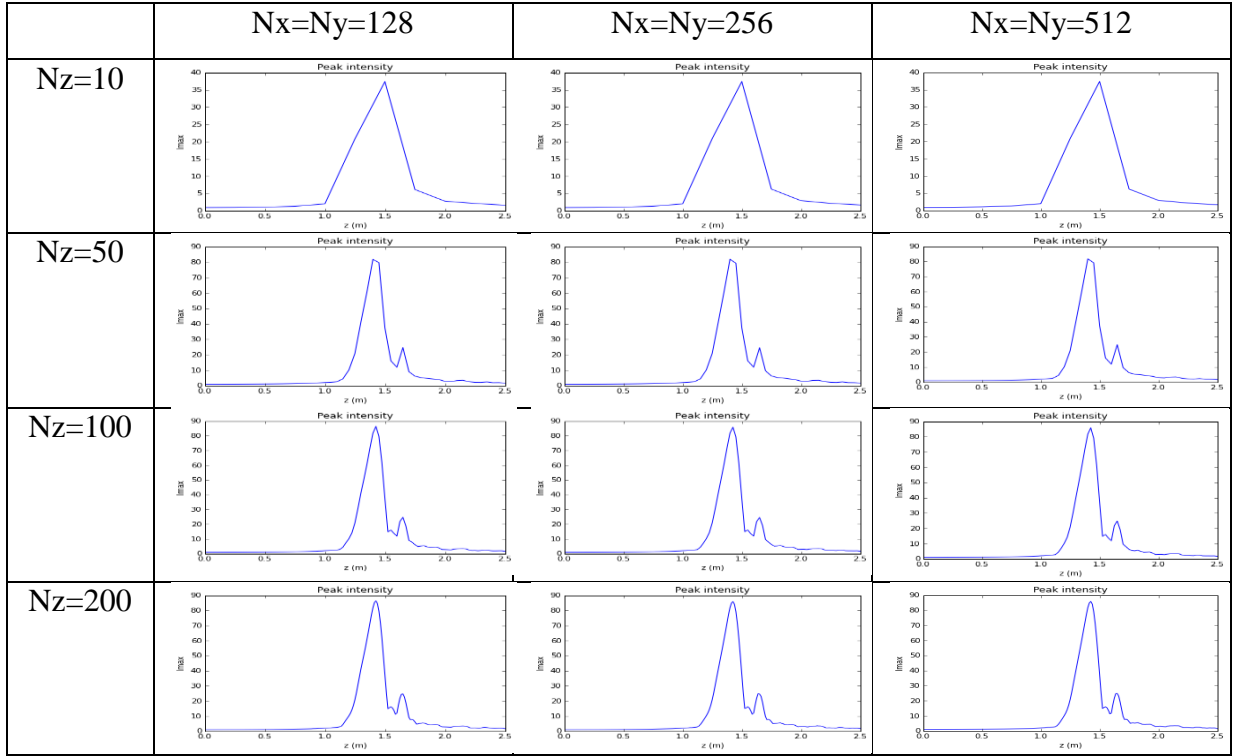


Figure 3.1: Simulated maximum intensity profiles as a function of the propagation distance z for Airy Ring beam ($r_0=1\text{mm}$, $w_0=0.19\text{mm}$, $\alpha=0.05$).

Figure 3.1 depicts simulated maximum intensity profiles as a function of the propagation distance z for an Airy Ring beam with radius which is equal to $r_0=1\text{mm}$, width which is equal to $w_0=0.19\text{mm}$ and exponential decaying factor which is equal to $a=0.05$ for all the discretization schemes of the Airy Ring beam propagation simulations which are listed in Table 3.1. We observe that for lower values of number of sampling points at x , y and propagation z direction, the numerical and the theoretical maximum intensity profiles have large discrepancy. On the other hand, for higher values of number of sampling points at x , y and propagation z direction, the numerical and the theoretical maximum intensity profiles have small discrepancy.

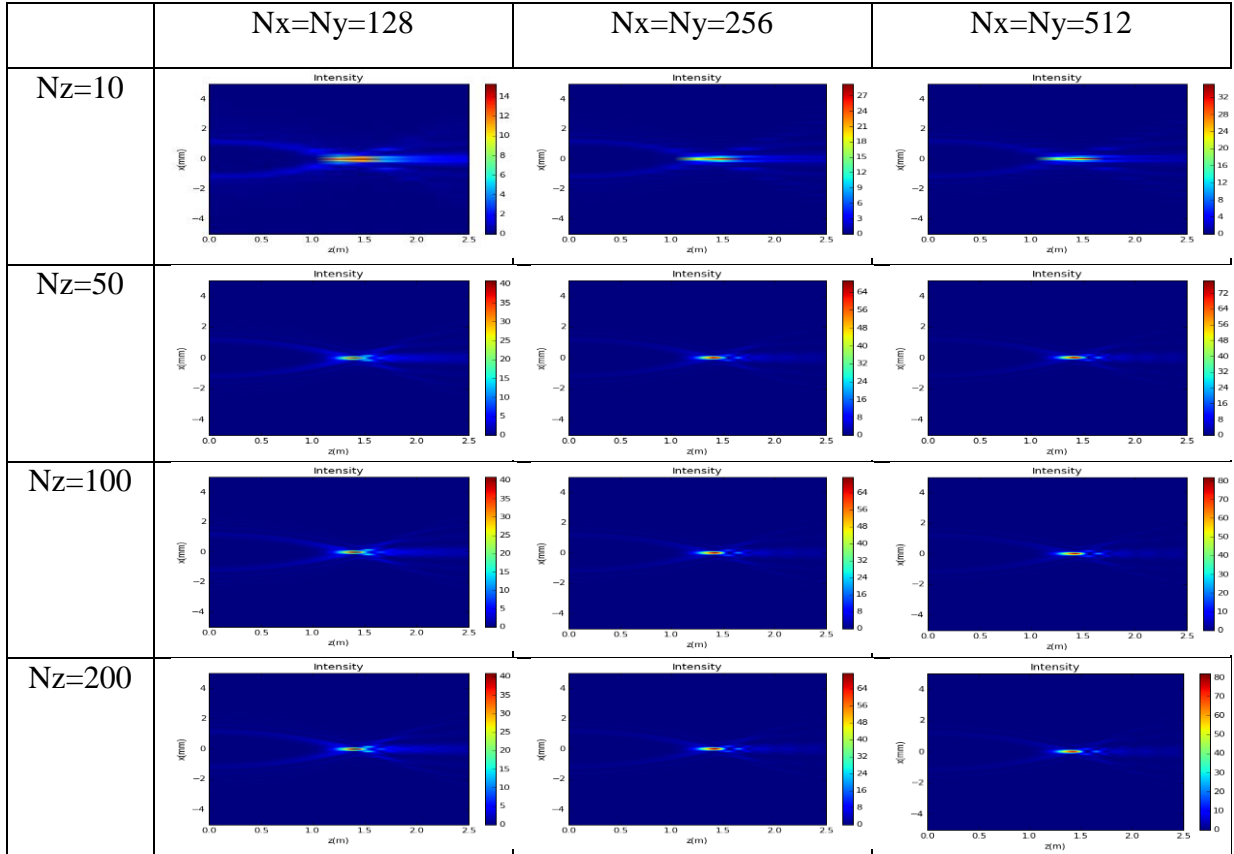


Figure 3.2: Simulated intensity profiles as a function of the propagation distance z for Airy Ring beam ($r_0=1\text{mm}$, $w_0=0.19\text{mm}$, $\alpha=0.05$).

Figure 3.2 depicts simulated intensity profiles as a function of the propagation distance z for an Airy Ring beam with radius which is equal to $r_0=1\text{mm}$, width which is equal to $w_0=0.19\text{mm}$ and exponential decaying factor which is equal to $a=0.05$ for all the discretization schemes of the Airy Ring beam propagation simulations which are listed in Table 3.1. We observe that for lower values of number of sampling points at x , y and propagation z direction, the beam scatters and deforms. On the other hand, for higher values of number of sampling points at x , y and propagation z direction, the beam focuses. In this case we observe also that the intensity value at the focus point of the beam has a high value if we compare it with the previous case where the intensity value at the focus point of the beam is low.

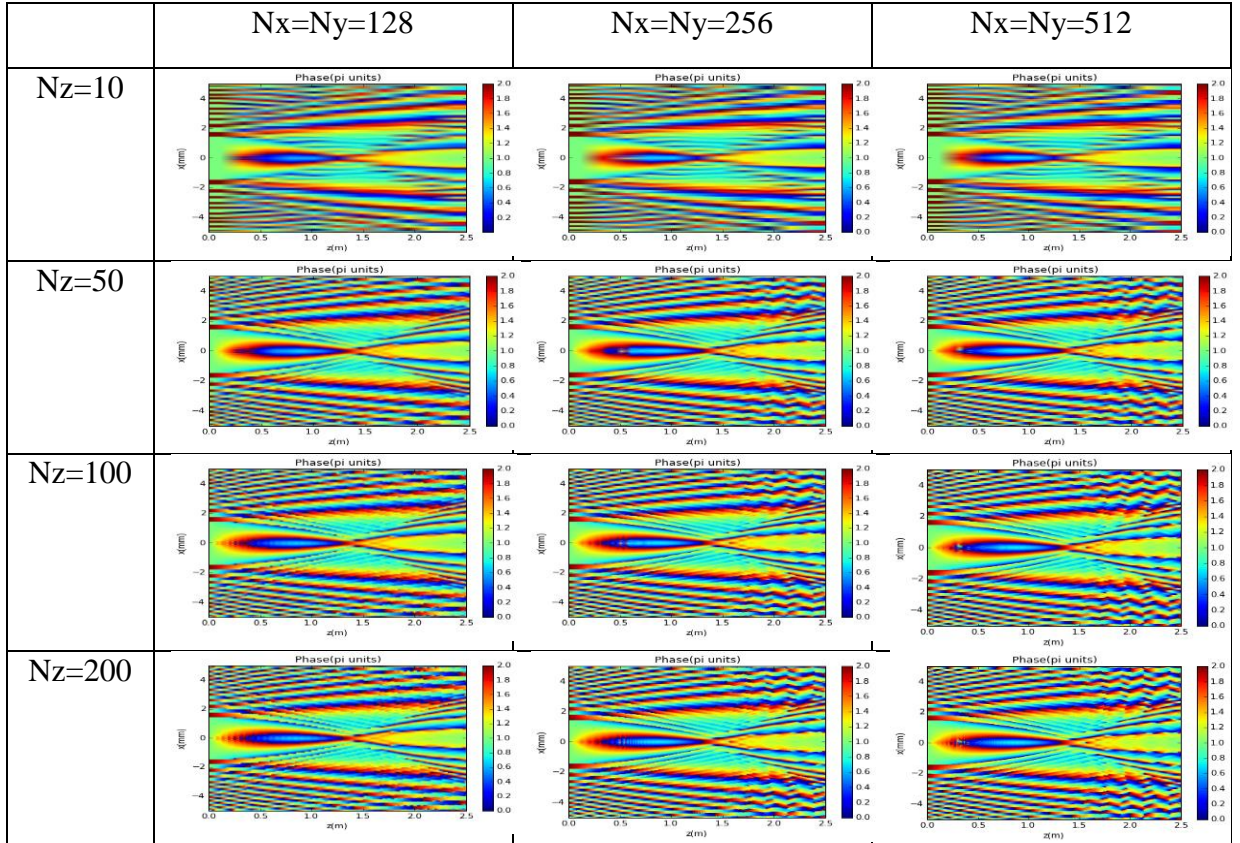


Figure 3.3: Simulated phase profiles as a function of the propagation distance z for Airy Ring beam ($r_0=1\text{mm}$, $w_0=0.19\text{mm}$, $\alpha=0.05$).

Figure 3.3 depicts simulated phase profiles as a function of the propagation distance z for an Airy Ring beam with radius which is equal to $r_0=1\text{mm}$, width which is equal to $w_0=0.19\text{mm}$ and exponential decaying factor which is equal to $a=0.05$ for all the discretization schemes of the Airy Ring beam propagation simulations which are listed in Table 3.1. We observe that for lower values of number of sampling points at x , y and propagation z direction, there are enough artifacts at phase profiles of the Airy Ring beam. On the other hand, for higher values of number of sampling points at x , y and propagation z direction, there are not enough artifacts at phase profiles of the Airy Ring beam.

3.3 Ring-Airy propagation in free space

At following graph (Figure 3.4), we present the results of numerical simulation of the propagation of 5 Airy Ring beams with constant ring width $w_0=0.07\text{mm}$ but different radii ($r_0=1\text{mm}$, $r_0=1.5\text{mm}$, $r_0=2\text{mm}$, $r_0=2.5\text{mm}$, $r_0=3\text{mm}$) in free space. For

the cases where the Airy Ring beam radius is equal to $r_0=1\text{mm}$ and $r_0=1.5\text{mm}$, the transverse coordinates (x,y) are discretized to 512×512 sampling points and the window size is equal to $W=10\text{mm}$. On the other hand for the cases where the Airy Ring beam radius is equal to $r_0=2\text{mm}$, $r_0=2.5\text{mm}$ and $r_0=3\text{mm}$, the transverse coordinates (x,y) are discretized to 1024×1024 sampling points and the window size is equal to $W=20\text{mm}$. In all cases 200 steps are used for the propagation along z direction.

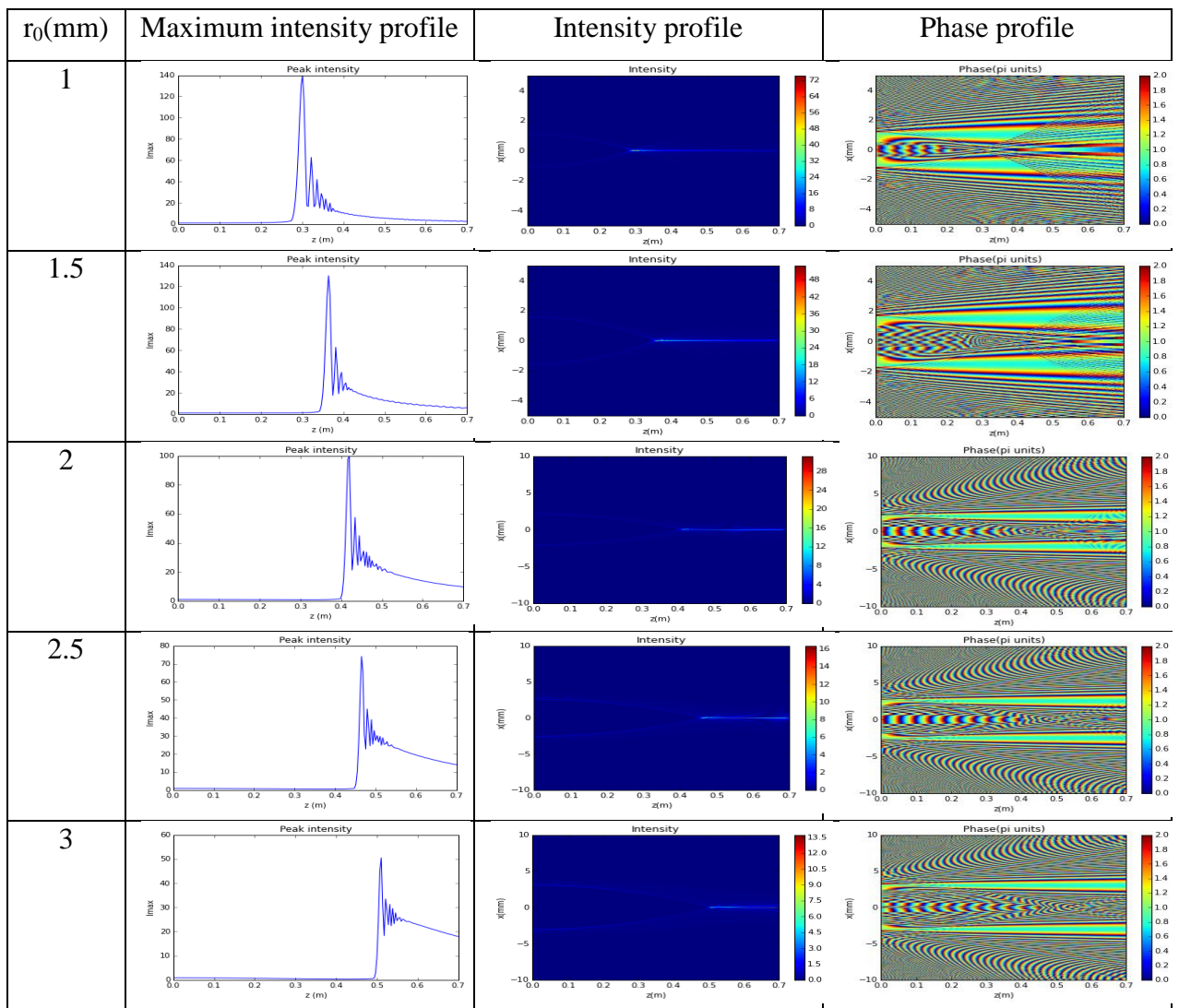


Figure 3.4: The results of numerical simulation for 5 Airy Ring beams with constant ring width $w_0=0.07\text{mm}$ but different radii ($r_0=1\text{mm}$, $r_0=1.5\text{mm}$, $r_0=2\text{mm}$, $r_0=2.5\text{mm}$, $r_0=3\text{mm}$) in free space.

Figure 3.4 depicts simulated maximum intensity profiles, intensity profiles and phase profiles as a function of the propagation distance z for 5 Airy Ring beams with

constant ring width $w_0=0.07\text{mm}$ but different radii ($r_0=1\text{mm}$, $r_0=1.5\text{mm}$, $r_0=2\text{mm}$, $r_0=2.5\text{mm}$, $r_0=3\text{mm}$) in free space. In order to extract the correct simulation results, the transverse coordinates (x, y) are discretized to 512×512 sampling points and the window size is equal to $W=10\text{mm}$ for the cases where the Airy Ring beam radius is equal to $r_0=1\text{mm}$ and $r_0=1.5\text{mm}$. On the other hand for the cases where the Airy Ring beam radius is equal to $r_0=2\text{mm}$, $r_0=2.5\text{mm}$ and $r_0=3\text{mm}$, the transverse coordinates (x, y) are discretized to 1024×1024 sampling points and the window size is equal to $W=20\text{mm}$. In all cases 200 steps are used for the propagation along z direction. The values of the following Table are obtained from the simulation results of this Figure.

For that 5 different Airy Ring beams with constant ring width $w_0=0.07\text{mm}$, we present the theoretical values of Ring Airy focus position, the numerical values of Ring Airy focus position, the percentage change (%) between them and the numerical values of Ring Airy focus contrast. These values are shown in Table 3.2.

$r_0(\text{mm})$	Numerical value of Ring Airy focus position (m)	Theoretical value of Ring Airy focus position (m)	Difference (%)	Numerical value of Ring Airy focus contrast
1.0	0.301	0.3	0.33	139.656
1.5	0.364	0.365	0.27	130.113
2.0	0.42	0.419	0.24	99.669
2.5	0.4655	0.466	0.11	74.044
3.0	0.511	0.51	0.2	50.506

Table 3.2: Theoretical and numerical values of Ring Airy focus position, the percentage change (%) between them and numerical value of Ring Airy focus contrast for 5 Ring Airy beams with constant ring width $w_0=0.07\text{mm}$ but different radii ($r_0=1\text{mm}$, $r_0=1.5\text{mm}$, $r_0=2\text{mm}$, $r_0=2.5\text{mm}$, $r_0=3\text{mm}$) in free space.

Table 3.2 depicts the theoretical and numerical values of Ring Airy focus position, the difference (%) between them and the numerical values of Ring Airy focus contrast for 5 Airy Ring beams with constant ring width $w_0=0.07\text{mm}$ but different radii ($r_0=1\text{mm}$, $r_0=1.5\text{mm}$, $r_0=2\text{mm}$, $r_0=2.5\text{mm}$, $r_0=3\text{mm}$) in free space. We observe that in all cases the numerical and the theoretical values of Rayleigh length have small

difference (%) between them which is less than 0.5%. We observe also that as the Airy Ring radius increases, the numerical value of Airy Ring focus position is increased but the numerical value of Airy Ring focus contrast is decreased.

In the case of constant radius of Airy Ring beams $r_0=1\text{mm}$, we present in Figure 3.5 the results of numerical simulation of the propagation of 5 Airy Ring beams with different ring widths ($w_0=0.07\text{mm}$, $w_0=0.09\text{mm}$, $w_0=0.13\text{mm}$, $w_0=0.16\text{mm}$, $w_0=0.19\text{mm}$) in free space. In these simulations the transverse coordinates (x,y) are discretized to 512×512 sampling points while 200 steps are used for the propagation along z direction.

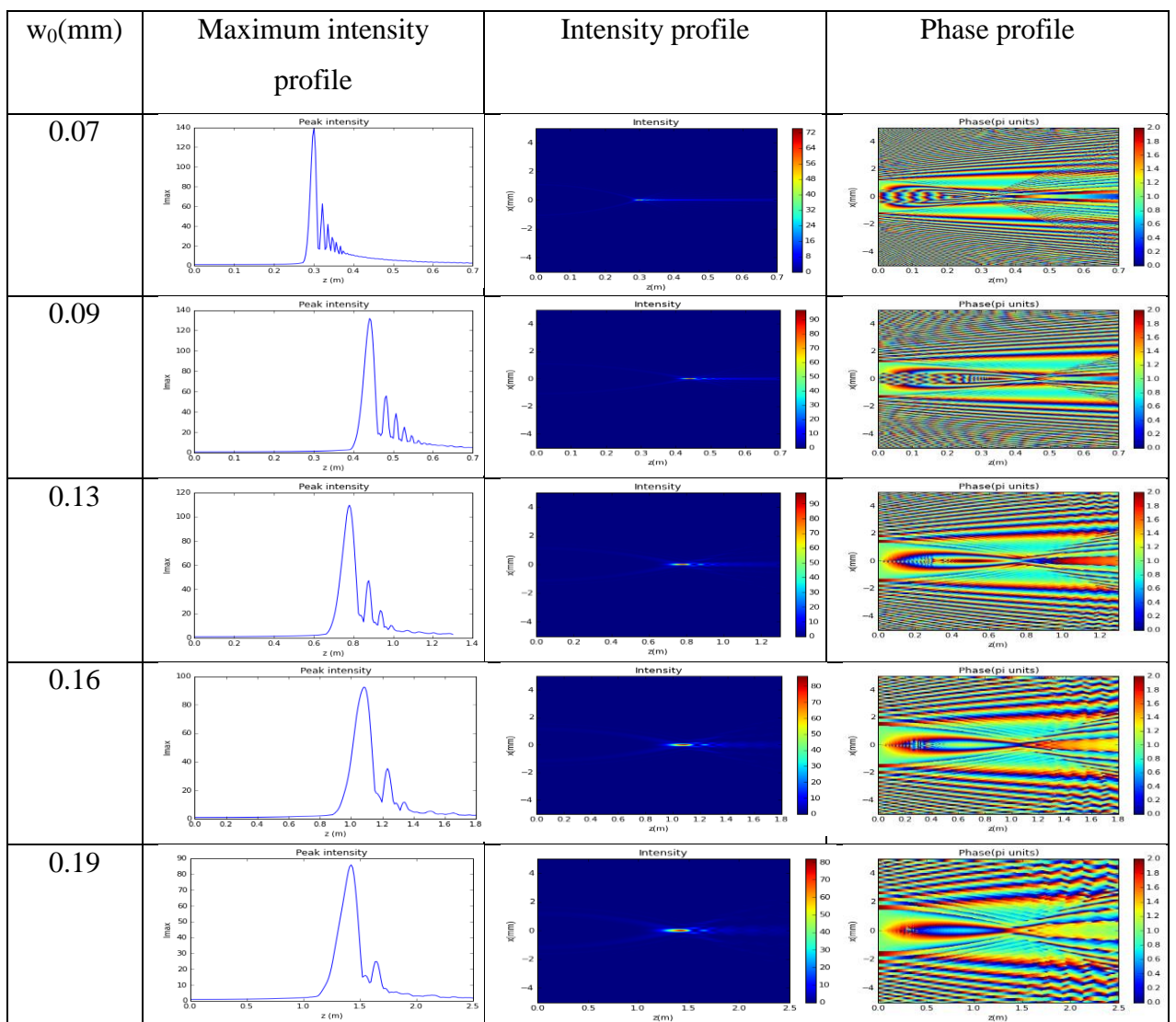


Figure 3.5: The results of numerical simulation for 5 Airy Ring Beams with constant radius $r_0=1\text{mm}$ but different ring width ($w_0=0.07\text{mm}$, $w_0=0.09\text{mm}$, $w_0=0.13\text{mm}$, $w_0=0.16\text{mm}$, $w_0=0.19\text{mm}$) in free space.

Figure 3.5 depicts simulated maximum intensity profiles, intensity profiles and phase profiles as a function of the propagation distance z for 5 Airy Ring beams with constant radius $r_0=1\text{mm}$ but different ring width ($w_0=0.07\text{mm}$, $w_0=0.09\text{mm}$, $w_0=0.13\text{mm}$, $w_0=0.16\text{mm}$, $w_0=0.19\text{mm}$) in free space. The values of the following Table are obtained from the simulation results of this Figure.

Finally, we present the theoretical values of Ring Airy focus position, the numerical values of Ring Airy focus position, the percentage change (%) between them and the numerical values of Ring Airy focus contrast for 5 Airy Ring beams with constant radius $r_0=1\text{mm}$ but different ring widths ($w_0=0.07\text{mm}$, $w_0=0.09\text{mm}$, $w_0=0.13\text{mm}$, $w_0=0.16\text{mm}$, $w_0=0.19\text{mm}$) in free space.

$w_0(\text{mm})$	Numerical value of Ring Airy focus position (m)	Theoretical value of Ring Airy focus position (m)	Difference (%)	Numerical value of Ring Airy focus contrast
0.07	0.301	0.3	0.33	139.656
0.09	0.441	0.443	0.45	131.86
0.13	0.78	0.783	0.38	109.516
0.16	1.08	1.083	0.28	92.27
0.19	1.425	1.419	0.42	85.86

Table 3.3: Theoretical and numerical values of Ring Airy focus position, the percentage change (%) between them and numerical value of Ring Airy focus contrast for 5 Ring Airy beams with constant radius $r_0=1\text{mm}$ but different ring widths ($w_0=0.07\text{mm}$, $w_0=0.09\text{mm}$, $w_0=0.13\text{mm}$, $w_0=0.16\text{mm}$, $w_0=0.19\text{mm}$) in free space.

Table 3.3 depicts the theoretical and numerical values of Ring Airy focus position, the difference (%) between them and the numerical values of Ring Airy focus contrast for 5 Airy Ring beams with constant radius $r_0=1\text{mm}$ but different ring widths ($w_0=0.07\text{mm}$, $w_0=0.09\text{mm}$, $w_0=0.13\text{mm}$, $w_0=0.16\text{mm}$, $w_0=0.19\text{mm}$) in free space. We observe that in all cases the numerical and the theoretical values of Rayleigh length have small difference (%) between them which is less than 0.5%. We observe also that as the Airy Ring width increases, the numerical value of Airy Ring focus position is increased but the numerical value of Airy Ring focus contrast is decreased.

4. Propagation in the presence of obstacles

In order to numerically study the effect of obstacles in the propagation of Ring-Airy beams we have used two kinds of obstacles, absorbing and refracting. Furthermore, we have compared Ring-Airy beams with Gaussian beams of similar spatial dimensions. The obstacle in both cases consisted of a single thin disk placed at various positions on the transverse plane and along the propagation axis. The obstacle size was chosen so that it is comparable to the beam's FWHM. Following this approach our results were analyzed in normalized units, so that our results can lead to generic conclusions. In the case of refracting obstacles the obstacle was a thin piece of circular glass that induced π and $\pi/2$ phase jumps. At following graph, we present the beam and the obstacle which is consisted of a single thin disk placed at various positions on the transverse plane (x) and along the propagation axis (z).

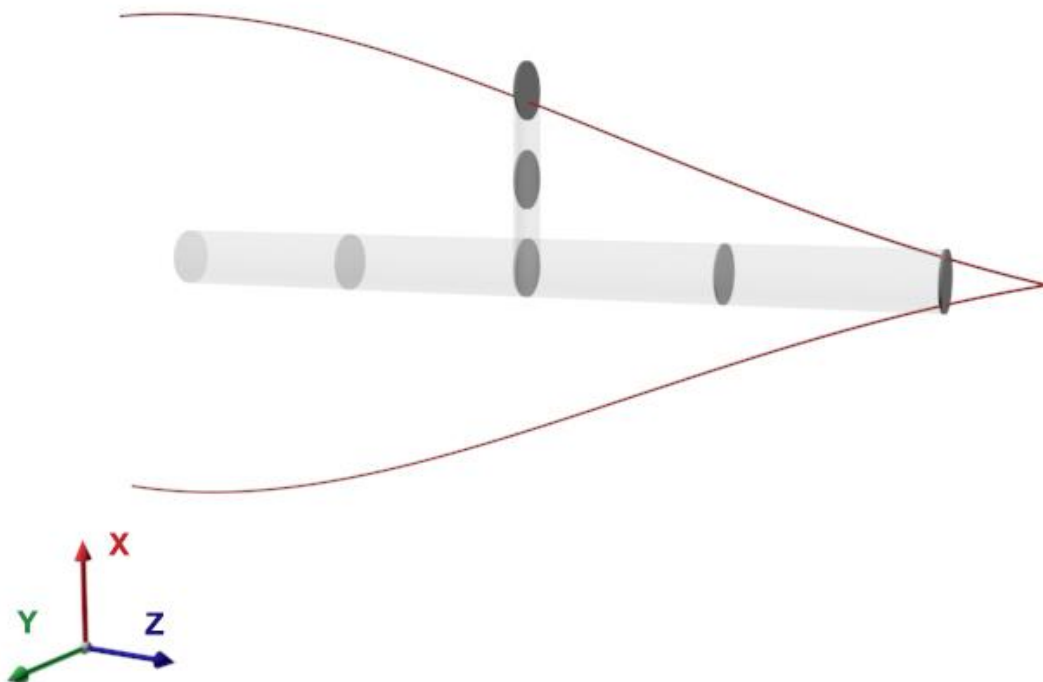


Figure 4.1: The beam and the obstacle which is consisted of a single thin disk placed at various positions on the transverse plane (x) and along the propagation axis (z).

Figure 4.1 depicts the beam and the obstacle which is moved in x and z direction. The beam can be a Gaussian or an Airy Ring beam. On the other hand, the obstacle

can be a circular block or a circular glass. In the case which the obstacle is a circular glass we examine two different cases. In the first case, the thickness of the circular glass is equal to $\lambda/2=0.4\mu\text{m}$, which induces π phase jump and in the second case, the thickness of the circular glass is equal to $\lambda/4=0.2\mu\text{m}$, which induces $\pi/2$ phase jump.

4.1 Perfectly absorbing propagation of a Gaussian beam in the presence of a circular block

a. Variable size

We consider a Gaussian beam with width $w_g=2.26\text{mm}$, where $\lambda=0.8\ \mu\text{m}$. The propagation distance z is 1.3 m. In the following simulations the transverse coordinates (x,y) are discretized to 1024×1024 sampling points while 200 steps are used for the propagation along z direction. We put an obstacle (circular block) at the center $(x=0,y=0)$ of x,y directions and at the middle between $z=0$ and the focus point of the Gaussian beam. At following graphs, we present the results of numerical simulation of the propagation of the Gaussian beam in the cases which the obstacle width D is different for every case. ($D= 2*r_0/3, r_0, 2*r_0, 2*(r_0+3w_0), 2*(r_0+7w_0), 2*(r_0+10w_0)$).

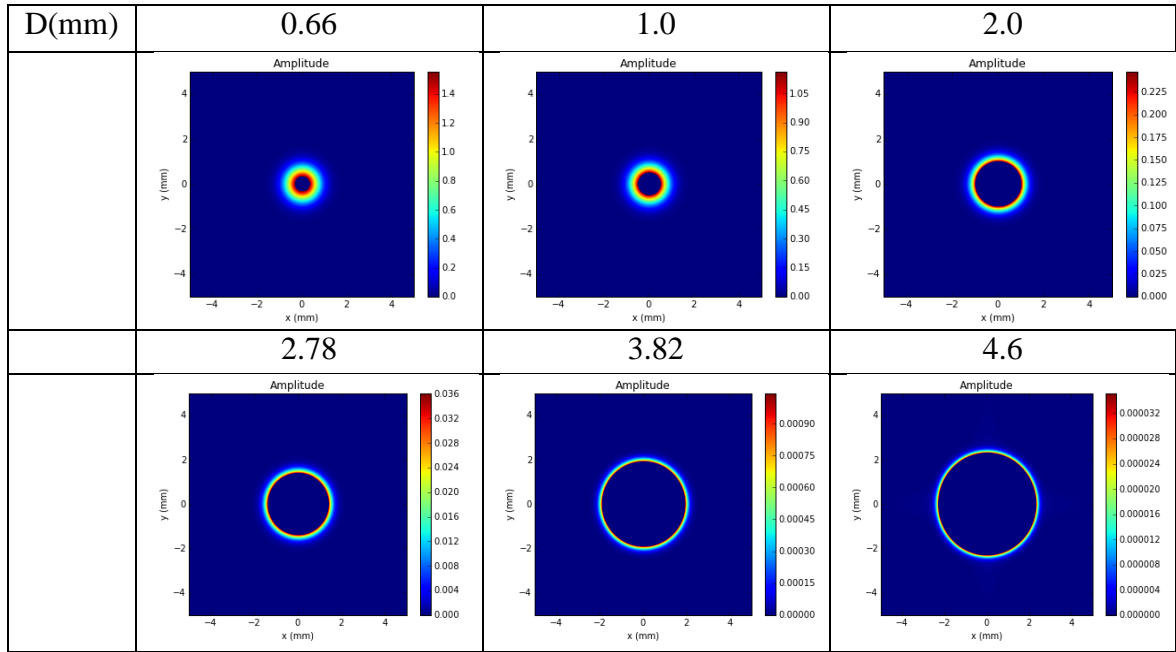


Figure 4.2: Beam amplitude after the circular block for a Gaussian beam with $w_g=2.26\text{mm}$, which propagates in the presence of a circular block with different size in every case ($D=2*r_0/3, r_0, 2*r_0, 2*(r_0+3w_0), 2*(r_0+7w_0), 2*(r_0+10w_0)$).

Figure 4.2 depicts beam amplitude after the circular block for a Gaussian beam. When the obstacle width is equal to $D=0.66\text{mm}$, we observe a small black circle at the center of the square. It represents the circular block which is situated at the middle between $z=0$ and the focus point of the Gaussian beam. We observe that as the obstacle width increases, this black circle which represents the obstacle also increases. We observe also that the values at colorbar decrease as the obstacle width increases. This happens because the circular block cuts more energy which does not reach at the focus point of the beam, as the obstacle width increases.

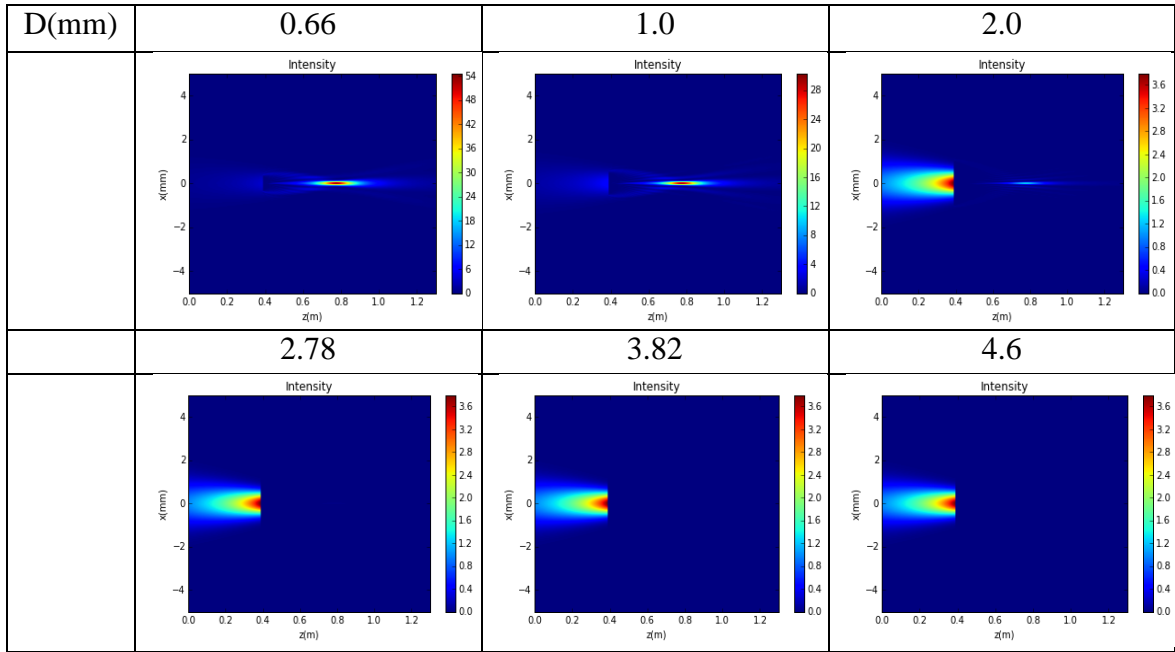


Figure 4.3: Intensity profile for a Gaussian beam with $w_g=2.26\text{mm}$, which propagates in the presence of a circular block with different size in every case ($D= 2*r_0/3, r_0, 2*r_0, 2*(r_0+3w_0), 2*(r_0+7w_0), 2*(r_0+10w_0)$).

Figure 4.3 depicts intensity profile of the propagated Gaussian beam for different values of size of the circular block (D). It is shown that for lower values of D , the beam focuses, whereas for higher values of D it scatters and deforms. For lower values of the obstacle width ($D < 2\text{mm}$), the intensity from the diffraction in the point which is situated the obstacle has added to the intensity in the focus point of the beam. For higher values of the obstacle width ($D > 2\text{mm}$), the intensity at the focus point of the Gaussian beam has zero value. This happens because the circular block cuts all the energy which does not reach at the focus point of the beam.

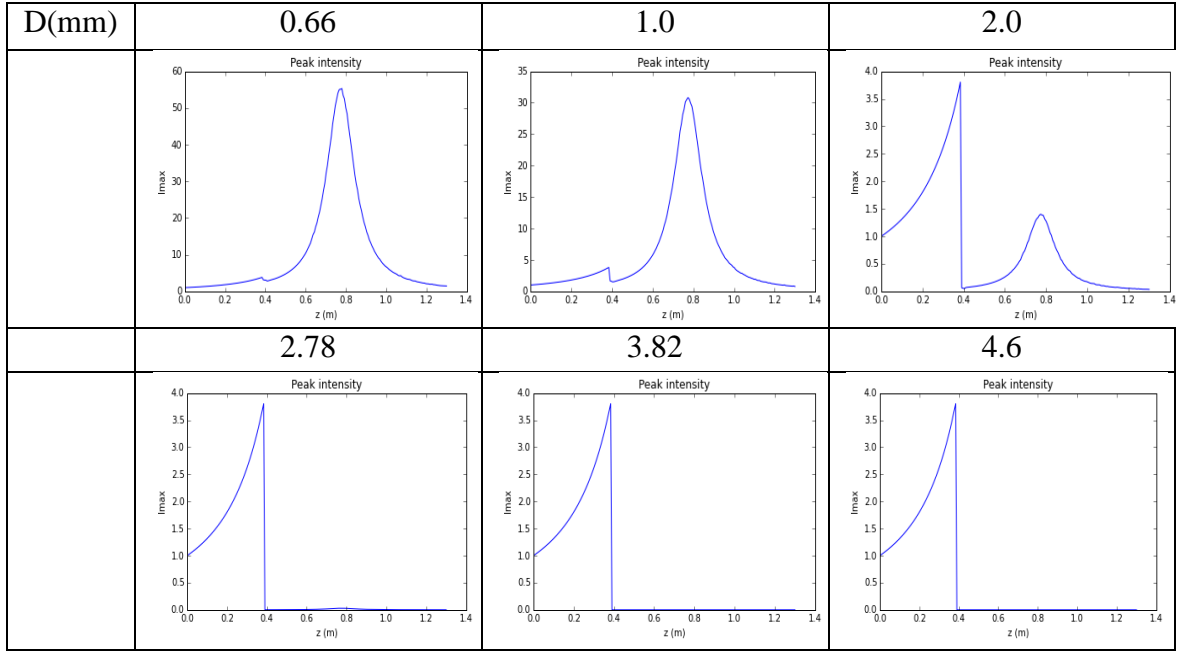


Figure 4.4: Maximum intensity profile for a Gaussian beam with $w_g=2.26\text{mm}$, which propagates in the presence of a circular block with different size in every case ($D= 2*r_0/3, r_0, 2*r_0, 2*(r_0+3w_0), 2*(r_0+7w_0), 2*(r_0+10w_0)$).

Figure 4.4 depicts maximum intensity profile of the propagated Gaussian beam for different values of size of the circular block (D). It is shown that for lower values of D , the numerical and the theoretical maximum intensity profile have small discrepancy. For higher values of the obstacle width (D), the discrepancy between the numerical and the theoretical maximum intensity profile is larger. For low values of the size of the circular block (D), the intensity at the focus point of the beam has high value. For a value of obstacle width which is equal to $D=2.0\text{mm}$, the intensity at focus point of the beam has decreased and the intensity at the point which is situated the obstacle has increased. For higher values ($D>2\text{mm}$), the intensity at the focus point of the beam drops to zero and the intensity at the point which is situated the obstacle has its maximum value.

b. Variable longitudinal position

We consider a Gaussian beam with width $w_g=2.26\text{mm}$, where $\lambda=0.8 \mu\text{m}$. The propagation distance z is 1.3 m. In the following simulations the transverse coordinates (x,y) are discretized to 1024×1024 sampling points while 200 steps are

used for the propagation along z direction. We put an obstacle (circular block) at the center ($x=0,y=0$) of x,y directions. The obstacle width is equal to 2mm. At following graphs, we present the results of numerical simulation of the propagation of the Gaussian beam in the cases which the obstacle position z in z direction is different for every case. The obstacle position z varies from the point $z=0$ up to Gaussian focus point. ($z=100.0\text{mm}$, 200.0mm , 390.0mm , 500.0mm , 600.0mm , 700.0mm).

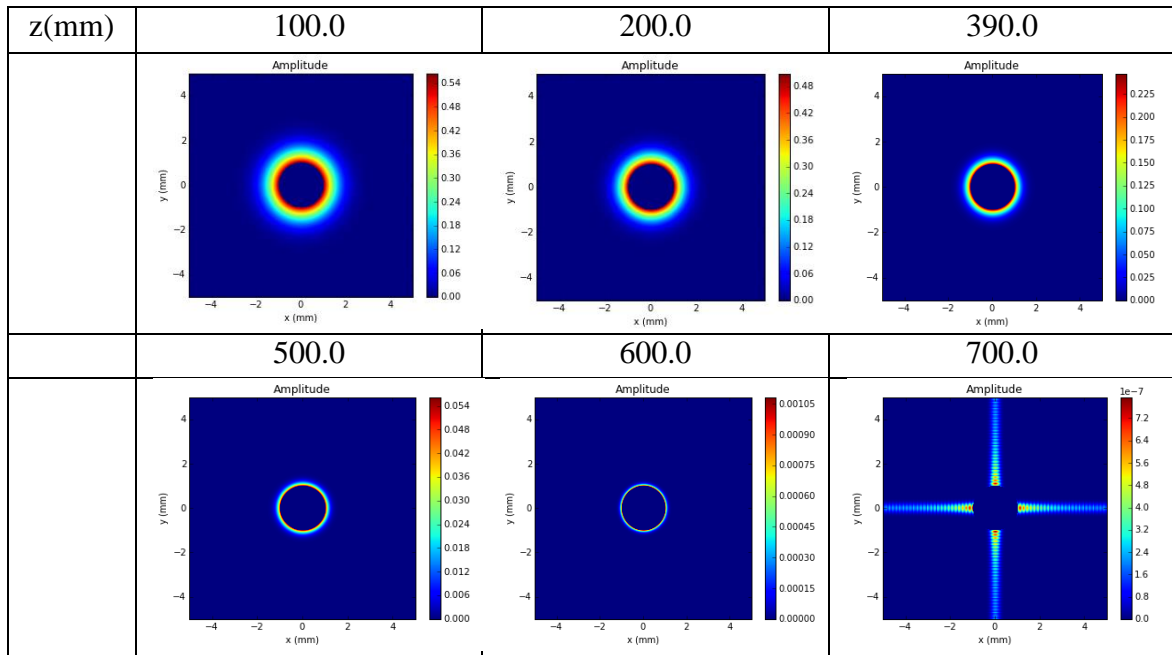


Figure 4.5: Beam amplitude after the circular block for a Gaussian beam with $w_g=2.26\text{mm}$, which propagates in the presence of a circular block with different position z in z direction in every case($z=100.0\text{mm}$, 200.0mm , 390.0mm , 500.0mm , 600.0mm , 700.0mm).

Figure 4.5 depicts beam amplitude after the circular block for a Gaussian beam. In this Figure we observe that the circle in the centre of the blue square has constant width because the circular block has constant width but its position in z direction is different in every case. Interestingly as the position of the obstacle width in z direction increases, the amplitude values in the colorbars decrease. This happens because as the obstacle moves near to the focus point of the Gaussian beam, it cuts more energy which does not reach to the focus point of the beam. For the case which the obstacle position in z direction is equal to $z=700.0\text{mm}$, we observe the phenomenon of diffraction at the position which is situated the obstacle.

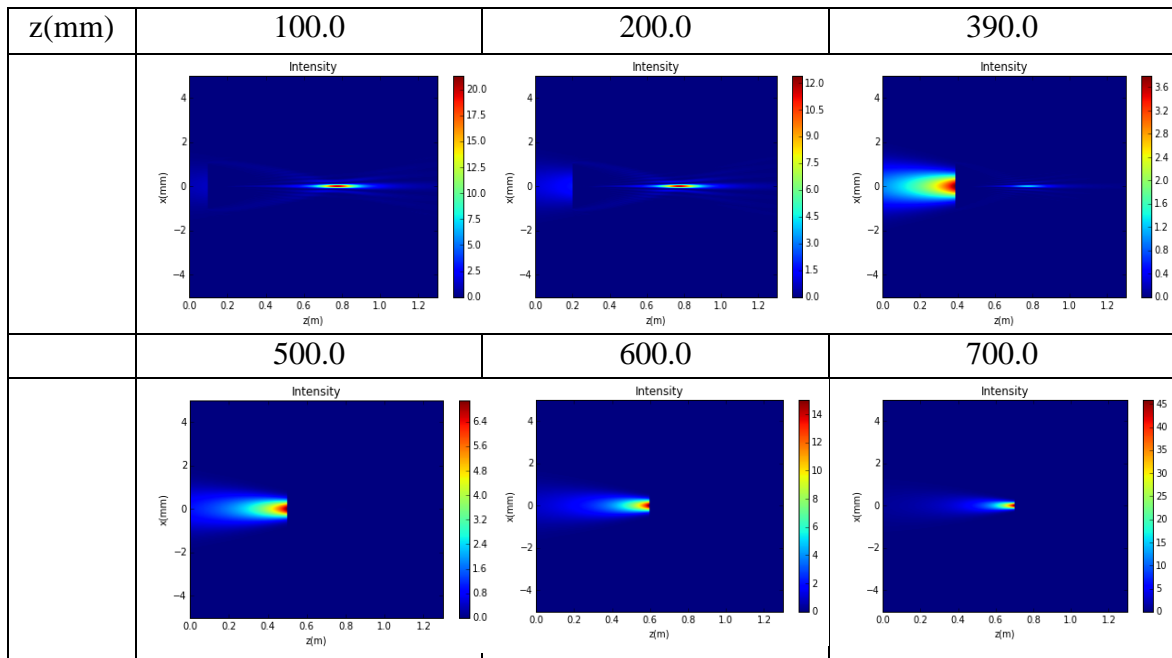


Figure 4.6: Intensity profile for a Gaussian beam with $w_g=2.26\text{mm}$, which propagates in the presence of a circular block with different position z in z direction in every case ($z=100.0\text{mm}$, 200.0mm , 390.0mm , 500.0mm , 600.0mm , 700.0mm).

Figure 4.6 depicts intensity profile of the propagated Gaussian beam for different values of position of the circular block in z direction (z). It is shown that for lower values of z , the beam focuses, whereas for higher values of z the intensity at the focus point of the beam drops to 0. For lower values of the obstacle position in z direction ($z < 390\text{mm}$), the intensity from the diffraction in the point which is situated the obstacle has added to the intensity at the focus point of the beam. For higher values of the obstacle position in z direction ($z > 390\text{mm}$), the intensity at the focus point of the Gaussian beam has zero value. This happens because the circular block cuts all the energy at the position where is situated, which does not reach at the focus point of the beam.

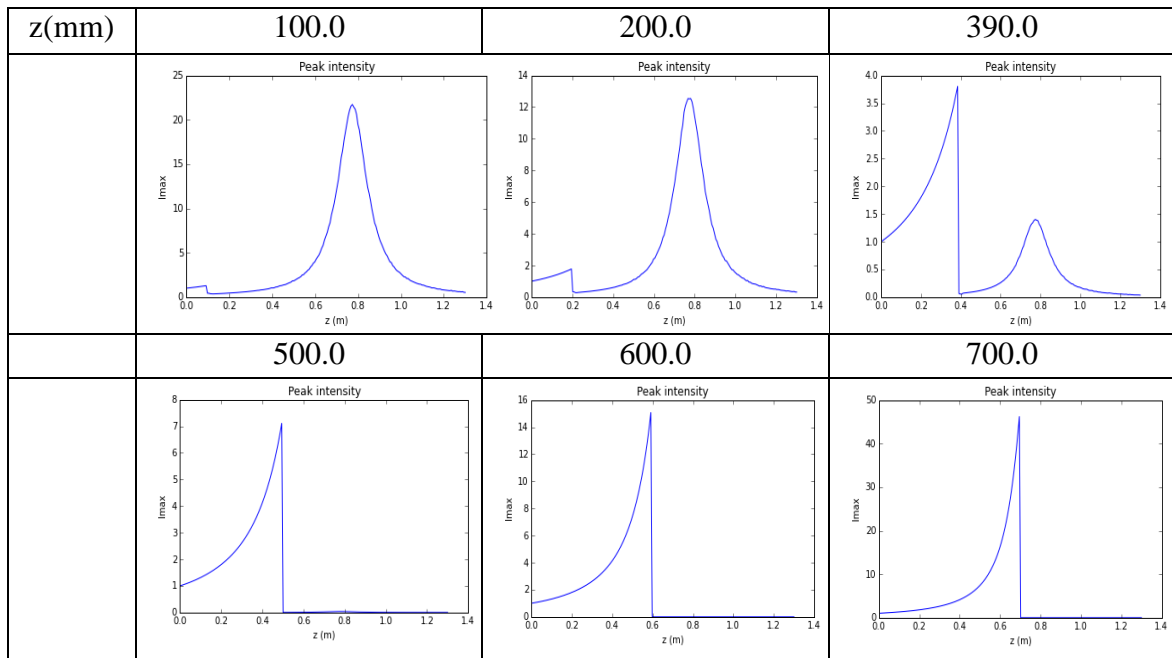


Figure 4.7: Maximum intensity profile for a Gaussian beam with $w_g=2.26\text{mm}$, which propagates in the presence of a circular block with different position z in z direction in every case ($z=100.0\text{mm}$, 200.0mm , 390.0mm , 500.0mm , 600.0mm , 700.0mm).

Figure 4.7 depicts maximum intensity profile of the propagated Gaussian beam for different values of the position of the circular block in z direction (z). It is shown that for lower values of z , the numerical and the theoretical maximum intensity profile have small discrepancy. For higher values of the obstacle position in z direction (z), the discrepancy between the numerical and the theoretical maximum intensity profile is larger. For low values of the position of the circular block in z direction (z), the intensity at the focus point of the beam has high value. For a value of obstacle position in z direction which is equal to $z=390.0\text{mm}$, the intensity at focus point of the beam has decreased and the intensity at the point which is situated the obstacle has increased. For higher values ($z>390.0\text{mm}$), the intensity at the focus point of the beam drops to zero and the intensity at the point which is situated the obstacle increases as the obstacle position in z direction increases. This happens because the circular block cuts all the energy of the beam, which does not reach at the focus point of the beam.

c. Variable transverse position

The next step is to study the propagation of the same Gaussian beam as previous in which the circular block has the same width as before ($D=2\text{mm}$) and we have put it in the middle between $z=0$ and the Gaussian focus point. In these simulations the transverse coordinates (x,y) are also discretized to 1024×1024 sampling points while 200 steps are used for the propagation along z direction. At following graphs, we present the results of numerical simulation of the propagation of the Gaussian beam in the cases which the obstacle position x in x direction is different for every case. ($x=0.26\text{mm}, 0.65\text{mm}, 1.04\text{mm}, 1.3\text{mm}, 1.69\text{mm}, 1.95\text{mm}$).

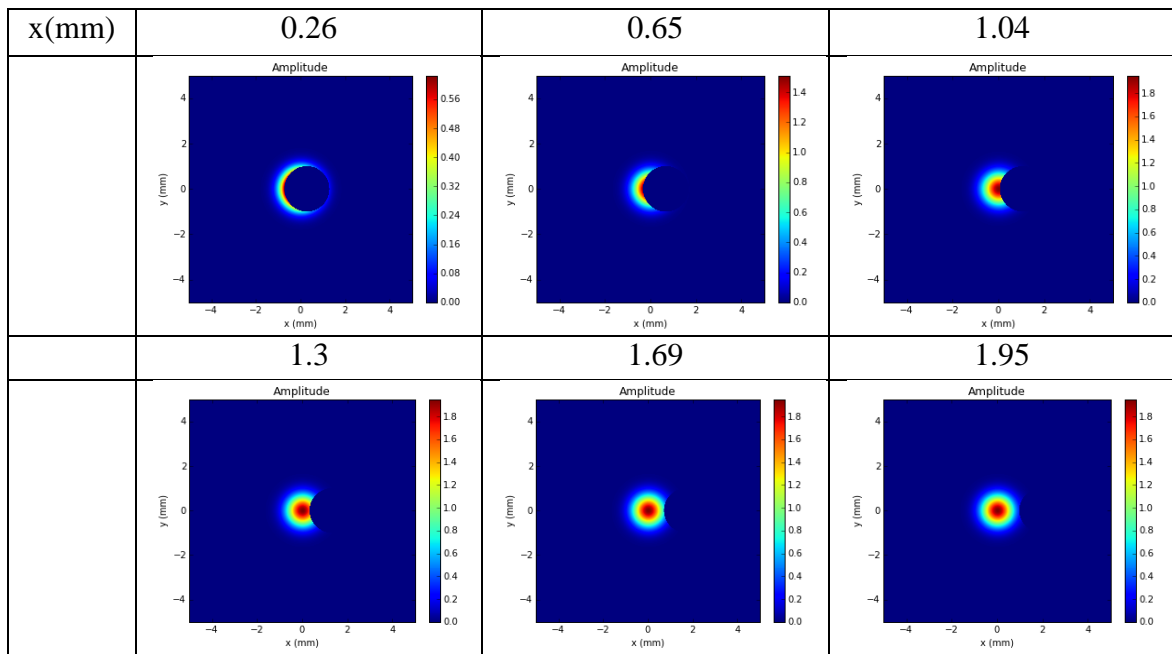


Figure 4.8: Beam amplitude after the circular block for a Gaussian beam with $w_g=2.26\text{mm}$, which propagates in the presence of a circular block with different position x in x direction in every case ($x=0.26\text{mm}, 0.65\text{mm}, 1.04\text{mm}, 1.3\text{mm}, 1.69\text{mm}, 1.95\text{mm}$).

Figure 4.8 depicts beam amplitude after the circular block for a Gaussian beam. In this Figure we observe a blue circle in the blue square which represents the circular block. When the obstacle position in x direction has a value of $x=0.26\text{mm}$, the obstacle has been moved from the center of the beam a distance which is equal to 0.26mm . As the value of obstacle position in x direction (x) increases, the movement of the circular block from the center of the beam also increases. This means that at

low values of x , the obstacle cuts much energy which does not reach at the focus point of the beam. On the other hand for high values of x , the obstacle does not cut so much energy which finally reaches at the focus point of the beam. For this reason, we observe lower values of beam amplitude at lower values of x than at higher values of x .

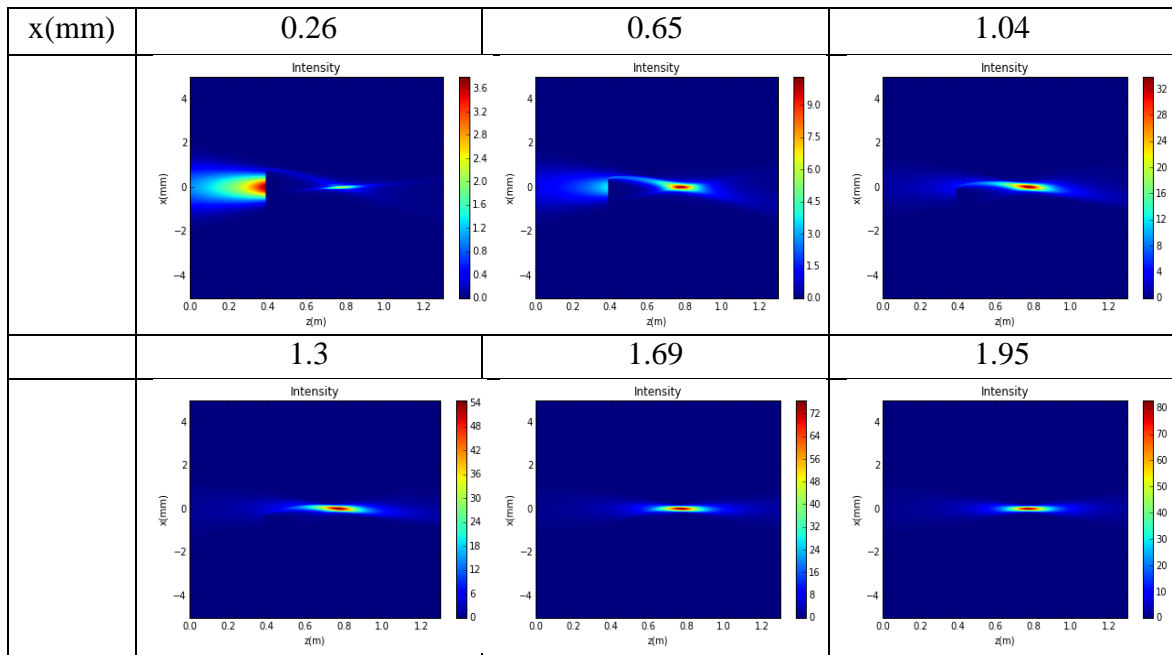


Figure 4.9: Intensity profile for a Gaussian beam with $w_g=2.26\text{mm}$, which propagates in the presence of a circular block with different position x in x direction in every case($x=0.26\text{mm}$, 0.65mm , 1.04mm , 1.3mm , 1.69mm , 1.95mm).

Figure 4.9 depicts intensity profile of the propagated Gaussian beam for different values of position of the circular block in x direction (x). It is shown that for lower values of x , the beam scatters and deforms, whereas for higher values of x it focuses. We observe in the Figure that when the obstacle position in x direction has a value which is equal to $x=0.26\text{mm}$, the obstacle cuts too much energy of the beam at the point which is situated. This energy does not reach at the focus point of the beam and this is the reason that we observe low values of intensity in the colorbar. As the obstacle moves in x direction, it cuts less energy at the point which is situated and finally more energy reaches at the focus point of the beam. For the case which the obstacle position in x direction has a value which is equal to $x=1.95\text{mm}$, much energy reaches at the focus point of the beam because the obstacle does not cut it at the point

which is situated and we observe that the intensity values at colorbar in this case have high values.

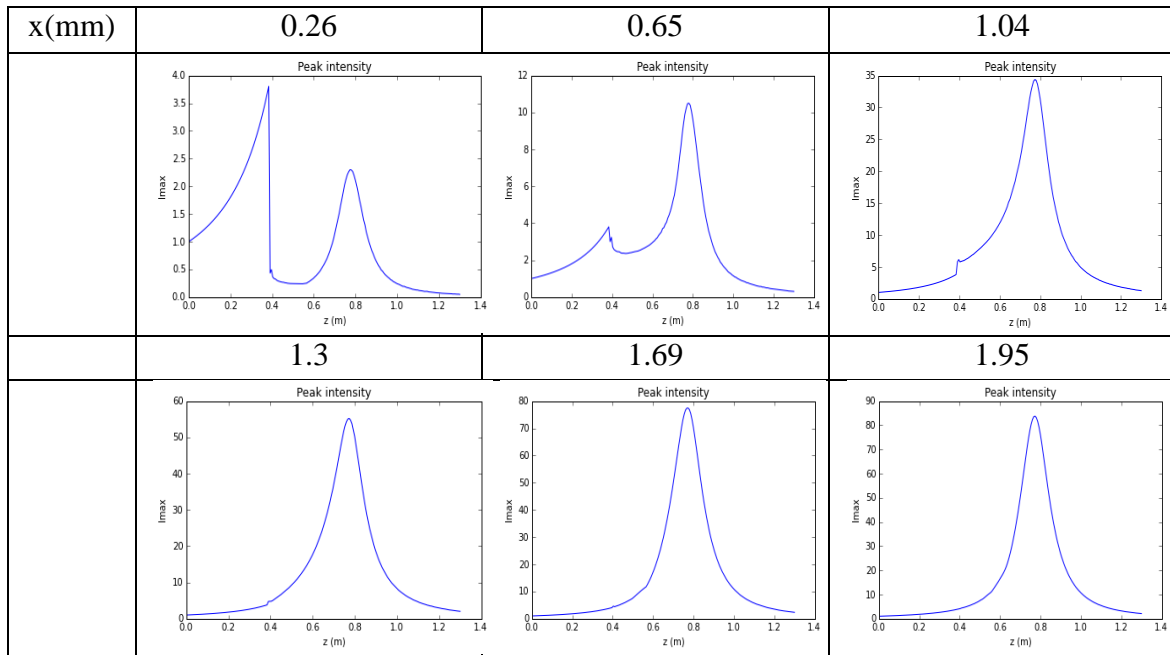


Figure 4.10: Maximum intensity profile for a Gaussian beam with $w_g=2.26\text{mm}$, which propagates in the presence of a circular block with different position x in x direction in every case($x=0.26\text{mm}$, 0.65mm , 1.04mm , 1.3mm , 1.69mm , 1.95mm).

Figure 4.10 depicts maximum intensity profile of the propagated Gaussian beam for different values of the position of the circular block in x direction (x). It is shown that for higher values of x , the numerical and the theoretical maximum intensity profile have small discrepancy. For lower values of the obstacle position in x direction (x), the discrepancy between the numerical and the theoretical maximum intensity profile is larger. When the value of obstacle position in x direction is equal to $x=0.26\text{mm}$, the intensity at the point which the obstacle is situated has a high value and the intensity at the focus point of the beam is lower than the previous one. For $x=0.65$, the intensity at the focus point of the beam has increased and its value is higher than the intensity value at the point which the obstacle is situated. As the position of the obstacle in x direction increases (x), the intensity at the focus point of the beam also increases because less energy is cut from the obstacle and finally more energy reaches at the focus point of the beam.

4.2 Perfectly refracting propagation of a Gaussian beam in the presence of a circular glass

a. Variable size

We consider a Gaussian beam with width $w_g=2.26\text{mm}$, where $\lambda=0.8\mu\text{m}$. The propagation distance z is 1.3m . In the following simulations the transverse coordinates (x,y) are discretized to 1024×1024 sampling points while 200 steps are used for the propagation along z direction. We put an obstacle (circular glass) at the center $(x=0, y=0)$ of x,y directions and at the middle between $z=0$ and the focus point of the Gaussian beam. The thickness of the glass is equal to $\lambda/2$ and its refractive index is equal to 1.0 . This glass adds π phase. At following graphs, we present the results of numerical simulation of the propagation of the Gaussian beam in the cases which the obstacle width D is different for every case. ($D= 2*r_0/3, r_0, 2*r_0, 2*(r_0+3w_0), 2*(r_0+7w_0), 2*(r_0+10w_0)$).

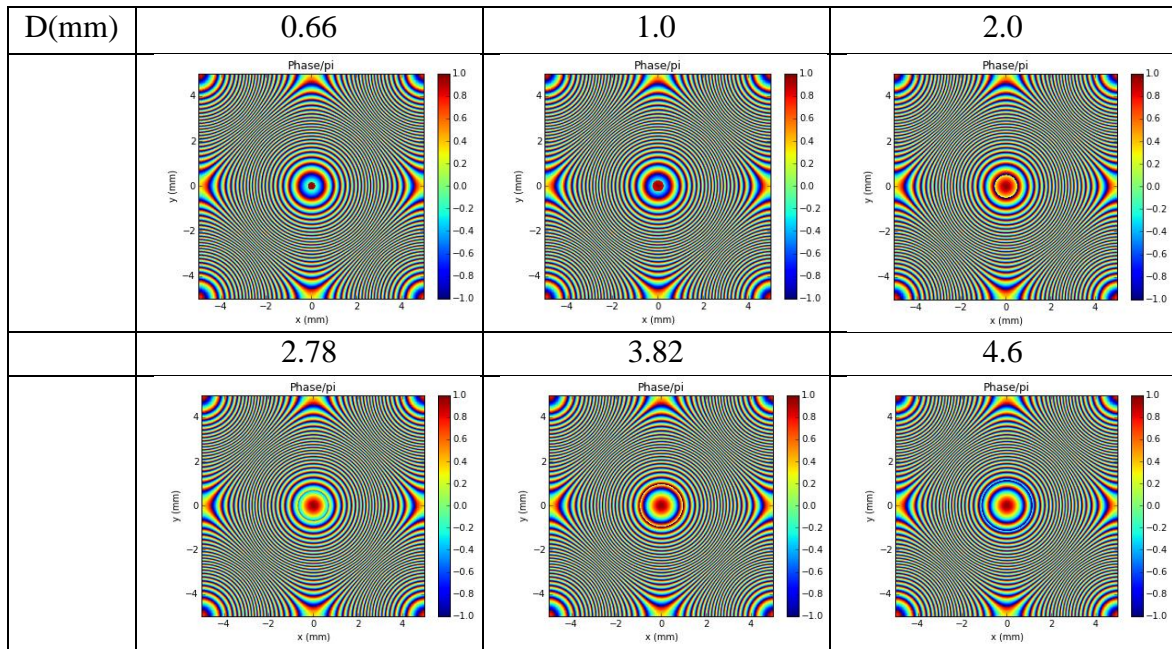


Figure 4.11: Beam phase after the circular glass for a Gaussian beam with $w_g=2.26\text{mm}$, which propagates in the presence of a circular glass with different size in every case ($D= 2*r_0/3, r_0, 2*r_0, 2*(r_0+3w_0), 2*(r_0+7w_0), 2*(r_0+10w_0)$).

Figure 4.11 depicts beam phase after the circular glass for a Gaussian beam. When the obstacle width is equal to $D=0.66\text{mm}$, we observe a small blue circle at the centre of the square. It represents the circular glass which is situated at the middle between $z=0$ and the focus point of the Gaussian beam. For the case which the obstacle width is equal to $D=2.0\text{mm}$, the small circle at the centre of the square becomes more red. This means that the phase in pi units there increases. We observe that as the obstacle width increases, this circle changes color from blue to red which means that as the obstacle width increases, the phase in pi units also increases. In all the cases we observe some artifacts at the edges of the square.

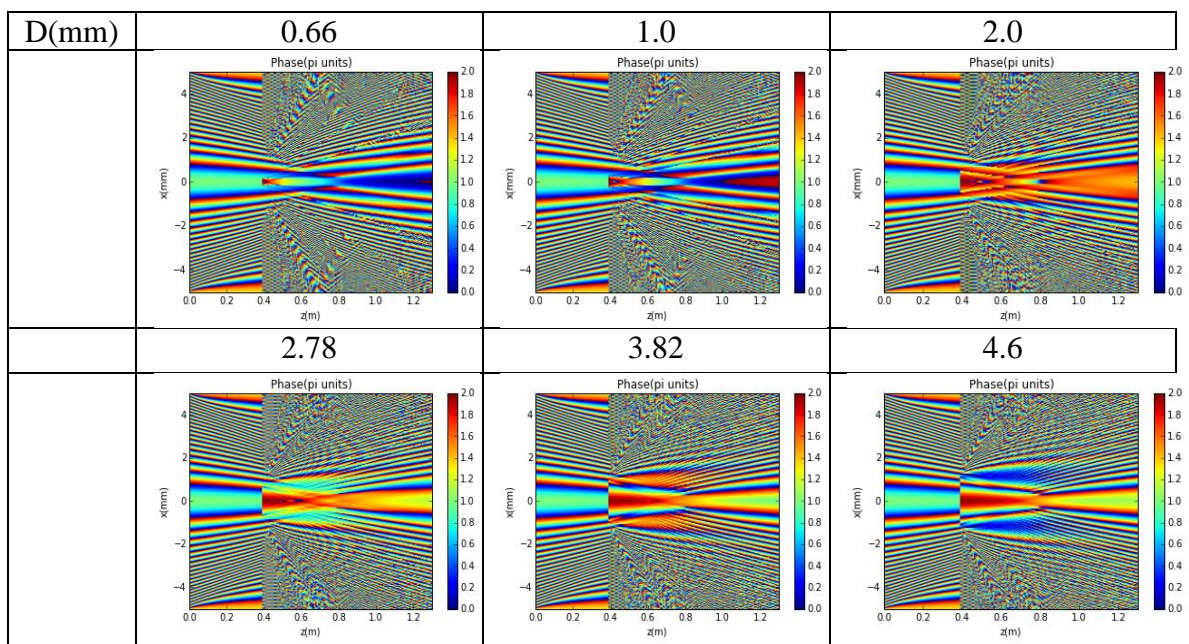


Figure 4.12: Phase profile for a Gaussian beam with $w_g=2.26\text{mm}$, which propagates in the presence of a circular glass with different size in every case ($D= 2*r_0/3, r_0, 2*r_0, 2*(r_0+3w_0), 2*(r_0+7w_0), 2*(r_0+10w_0)$).

Figure 4.12 depicts phase profile of the propagated Gaussian beam for different values of size of the circular glass (D). It is shown that for lower values of D , the beam focuses, whereas for higher values of D it scatters and deforms. For the case which the obstacle width is equal to $D=0.66\text{mm}$, the beam does not change enough its phase when it passes through the glass obstacle and it has a low value in pi units. When the obstacle width becomes $D=2.0\text{mm}$, we observe that when the Gaussian beam passes through the glass obstacle, its phase value in pi units changes at higher value. For higher values of the obstacle width ($D > 2.0\text{mm}$), we observe the same

phenomenon, the phase value increases when the beam passes through the glass obstacle. In all cases we observe some artifacts.

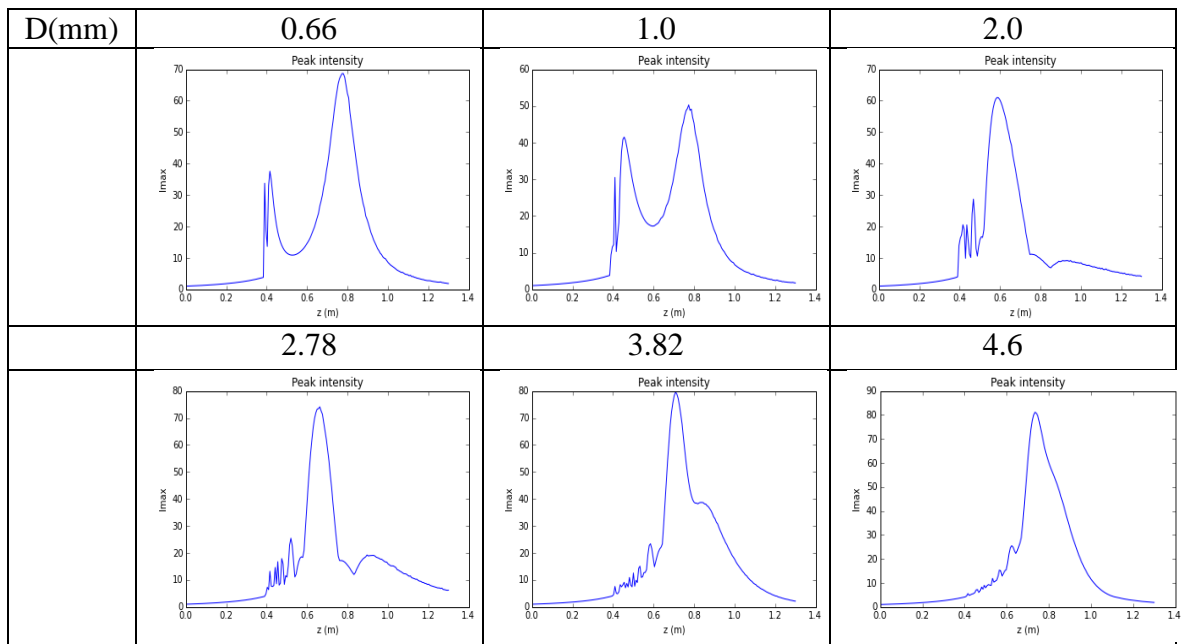


Figure 4.13: Maximum intensity profile for a Gaussian beam with $w_g=2.26\text{mm}$, which propagates in the presence of a circular glass with different size in every case ($D= 2*r_0/3, r_0, 2*r_0, 2*(r_0+3w_0), 2*(r_0+7w_0), 2*(r_0+10w_0)$).

Figure 4.13 depicts maximum intensity profile of the propagated Gaussian beam for different values of size of the circular glass (D). It is shown that for higher values of D , the numerical and the theoretical maximum intensity profile have small discrepancy. For lower values of the obstacle width D , the discrepancy between the numerical and the theoretical maximum intensity profile is larger. For the case which the obstacle width is equal to $D=0.66\text{mm}$, we observe an intensity at the point which the glass is situated and a higher intensity at the focus point of the beam. For $D=1.0\text{mm}$, the intensity at the point which the obstacle is situated remains at the same value as previous but the intensity at the focus point of the beam decreases. For higher values of the obstacle width ($D>2.0\text{mm}$) we observe that the intensity at the point which the obstacle is situated decreases and the intensity at the focus point of the beam increases.

b. Variable longitudinal position

We consider a Gaussian beam with width $w_g=2.26\text{mm}$, where $\lambda=0.8\ \mu\text{m}$. The propagation distance z is $1.3\ \text{m}$. In the following simulations the transverse coordinates (x,y) are discretized to 1024×1024 sampling points while 200 steps are used for the propagation along z direction. We put an obstacle (circular glass) at the center $(x=0,y=0)$ of x,y directions. The width of the glass is equal to $D=2.26\text{mm}$, the thickness of the glass is equal to $\lambda/2$ and its refractive index is equal to 1.0 . This glass adds π phase. At following graphs, we present the results of numerical simulation of the propagation of the Ring-Airy beam in the cases which the obstacle position in z direction is different for every case. The obstacle position varies from the point $z=0$ up to Gaussian focus point. ($z=100.0\text{mm}$, 200.0mm , 390.0mm , 500.0mm , 600.0mm , 700.0mm).

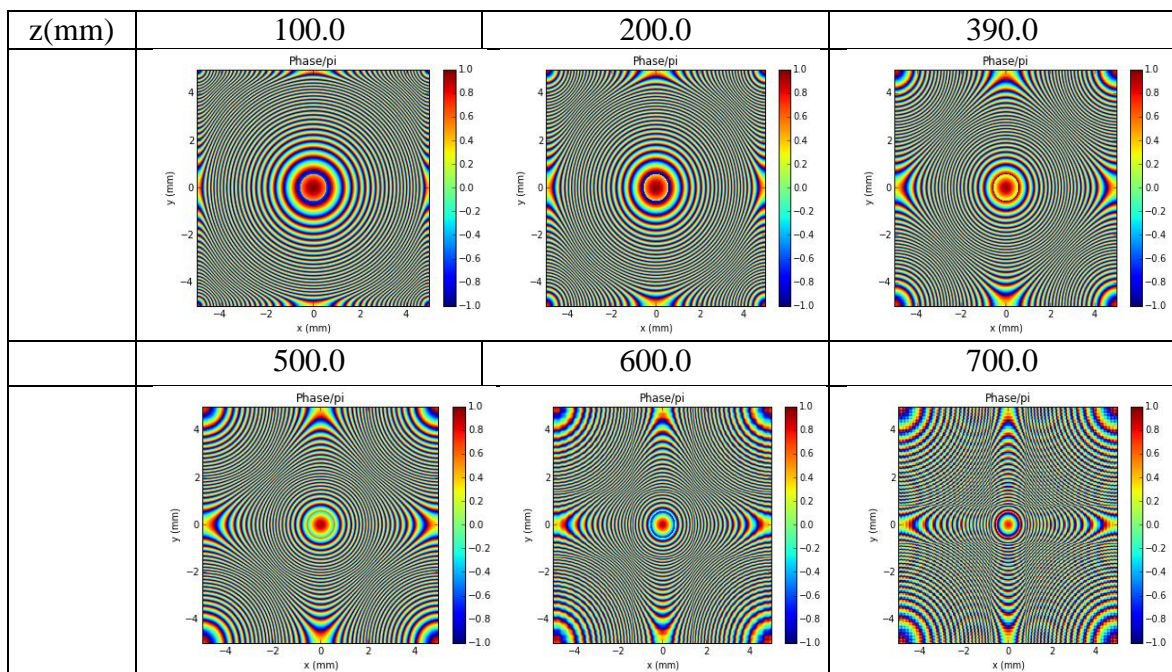


Figure 4.14: Beam phase after the circular glass for a Gaussian beam with $w_g=2.26\text{mm}$, which propagates in the presence of a circular glass with different position z in z direction in every case ($z=100.0\text{mm}$, 200.0mm , 390.0mm , 500.0mm , 600.0mm , 700.0mm).

Figure 4.14 depicts beam phase after the circular glass for a Gaussian beam. We observe that when the obstacle position in z direction has a value which is equal to $z=100.0\text{mm}$, there is a small red circle in the center of the square. This circle

represents the obstacle. In the case which the obstacle position in z direction has a value which is equal to $z=390.0\text{mm}$, this circle has changed color and we observe from the colorbar that the phase in pi units has lower value if we compare it with the previous case. For higher values of the obstacle position in z direction ($z>390.0\text{mm}$), we observe that the phase of the beam decreases as the obstacle position in z direction increases. In all cases we observe artifacts.

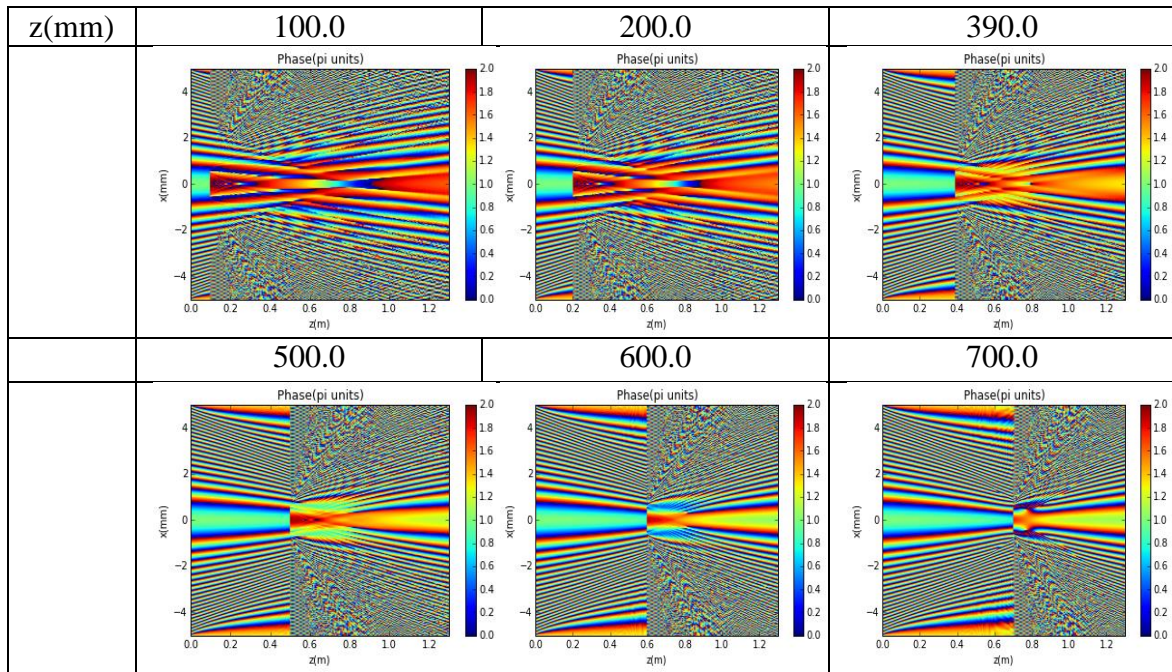


Figure 4.15:Phase profile for a Gaussian beam with $w_g=2.26\text{mm}$, which propagates in the presence of a circular glass with different position z in z direction in every case($z=100.0\text{mm}$, 200.0mm , 390.0mm , 500.0mm , 600.0mm , 700.0mm).

Figure 4.15 depicts phase profile of the propagated Gaussian beam for different values of position of the circular glass in z direction (z). It is shown that for lower values of z , the beam scatters and deforms, whereas for higher values of z it focuses. For the case which the obstacle position in z direction has a value which is equal to $z=100.0\text{mm}$, the phase change, when the beam passes through the glass obstacle, is very high. For higher values of the obstacle position in z direction (z), that change decreases as z increases. We observe in all cases the artifacts.

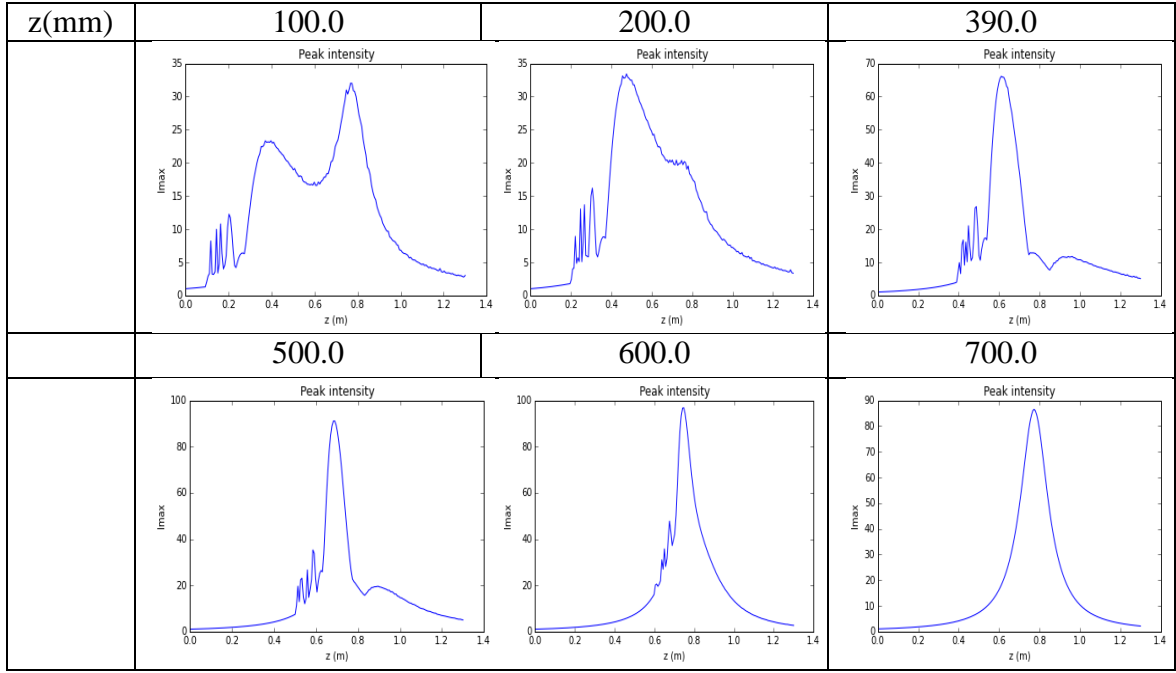


Figure 4.16: Maximum intensity profile for a Gaussian beam with $w_g=2.26\text{mm}$, which propagates in the presence of a circular glass with different position z in z direction in every case ($z=100.0\text{mm}$, 200.0mm , 390.0mm , 500.0mm , 600.0mm , 700.0mm).

Figure 4.16 depicts maximum intensity profile of the propagated Gaussian beam for different values of the obstacle position in z direction (z). It is shown that for higher values of z , the numerical and the theoretical maximum intensity profile have small discrepancy. For lower values of the obstacle position in z direction, the discrepancy between the numerical and the theoretical maximum intensity profile is larger. For the case which the obstacle position in z direction is equal to $z=100.0\text{mm}$, we observe a peak intensity at the focus point of the beam. As the obstacle position in z direction (z) increases, the intensity at the focus point of the beam also increases.

c. Variable transverse position

The next step is to study the propagation of the same Gaussian beam as previous in which the circular glass has width which is equal to 2.26mm , thickness which is equal to $\lambda/2$ and refractive index which is equal to 1.0 . This glass adds π phase and we have put it in the middle between $z=0$ and the Gaussian focus point. In these simulations the transverse coordinates (x,y) are also discretized to 1024×1024 sampling points while 200 steps are used for the propagation along z direction. At following graphs,

we present the results of numerical simulation of the propagation of the Ring-Airy in the cases which the obstacle position x in x direction is different for every case. ($x=0.26\text{mm}$, 0.65mm , 1.04mm , 1.3mm , 1.69mm , 1.95mm).

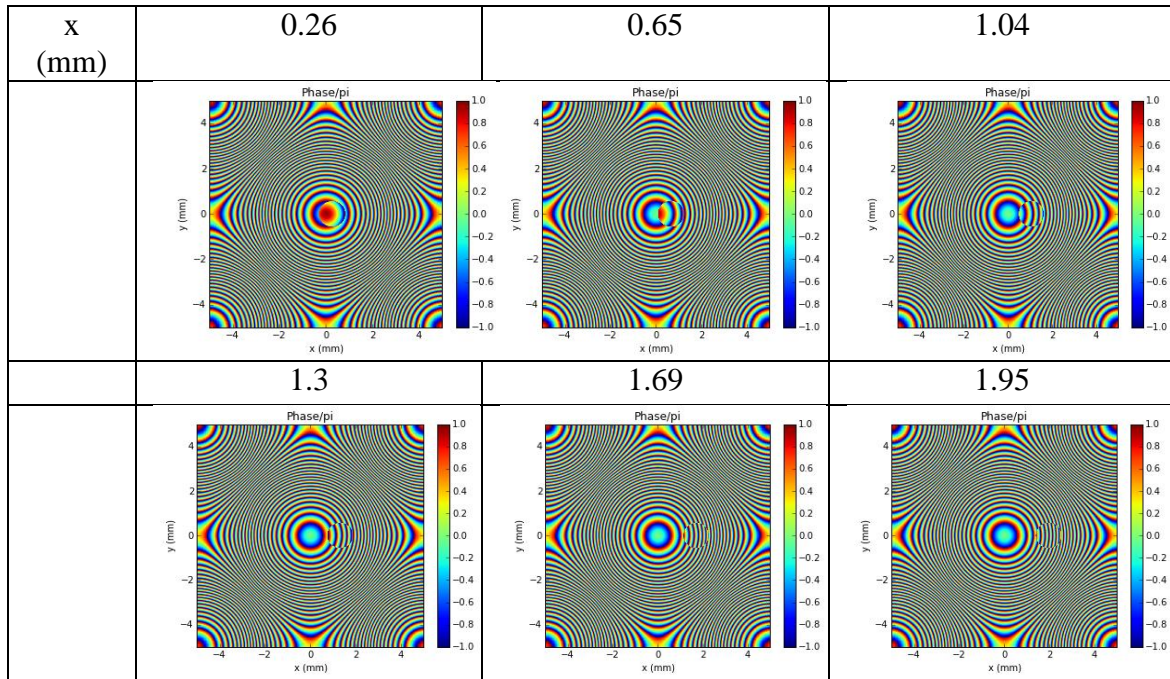


Figure 4.17: Beam phase after the circular glass for a Gaussian beam with $w_g=2.26\text{mm}$, which propagates in the presence of a circular glass with different position x in x direction in every case ($x=0.26\text{mm}$, 0.65mm , 1.04mm , 1.3mm , 1.69mm , 1.95mm).

Figure 4.17 depicts beam phase after the circular glass for a Gaussian beam. In this Figure we observe a circle in the square which represents the circular glass. When the obstacle position in x direction has a value of $x=0.26\text{mm}$, the obstacle has moved from the center of the beam a distance which is equal to 0.26mm . This means that only a small amount of the beam does not pass through the glass obstacle. The phase change in that case is high and this is the reason that we observe red circle in the centre of the square which means high value of phase beam in π units after the glass obstacle. As the value of obstacle position in x direction (x) increases, the movement of the circular glass from the center of the beam also increases. This means that as this movement is increased, the amount of the beam that passes through the glass obstacle is decreased. So, this is the reason that we observe blue circle which means low values of beam phase for high values of the obstacle position in x direction. In all cases there are artifacts.

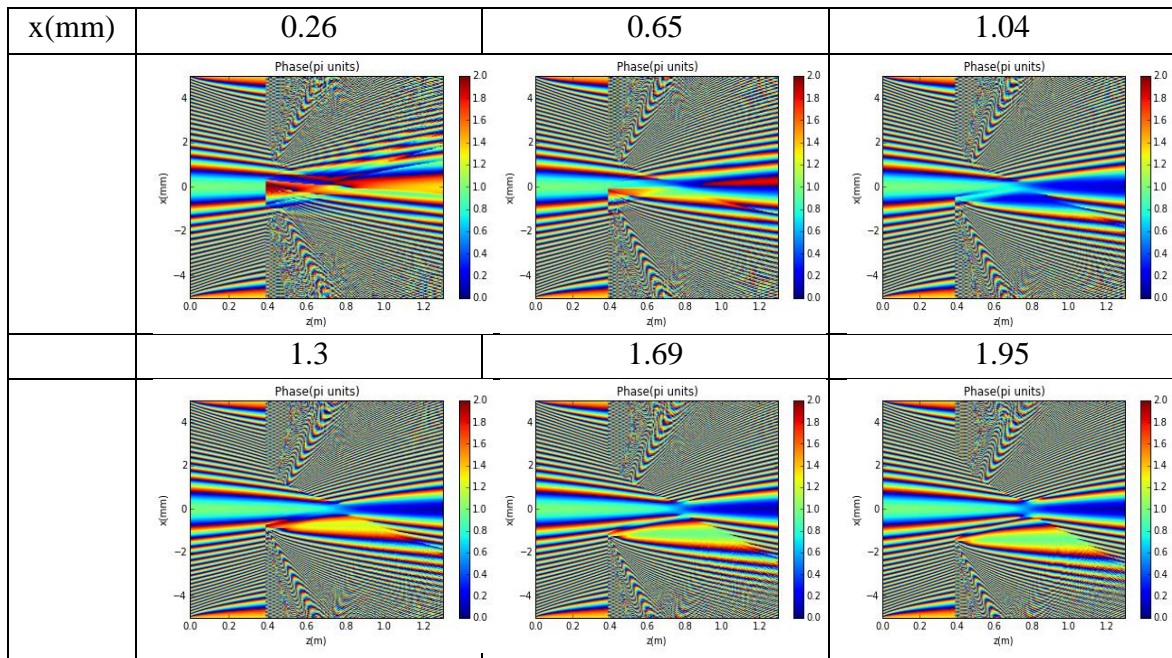


Figure 4.18: Phase profile for a Gaussian beam with $w_g=2.26\text{mm}$, which propagates in the presence of a circular glass with different position x in x direction in every case($x=0.26\text{mm}$, 0.65mm , 1.04mm , 1.3mm , 1.69mm , 1.95mm).

Figure 4.18 depicts phase profile of the propagated Gaussian beam for different values of position of the circular glass in x direction (x). It is shown that for lower values of x , the beam scatters and deforms, whereas for higher values of x it focuses. For the case which the obstacle position in x direction has a value which is equal to $x=0.26\text{mm}$, the phase change, when the beam passes through the glass obstacle, is very high. The reason is that a large amount of the beam passes through the glass, which changes its phase. For higher values of the obstacle position in x direction (x), that change is decreased as x is increased. The reason is that only a small amount of the beam passes through the glass obstacle, which changes its phase. We observe in all cases the artifacts.

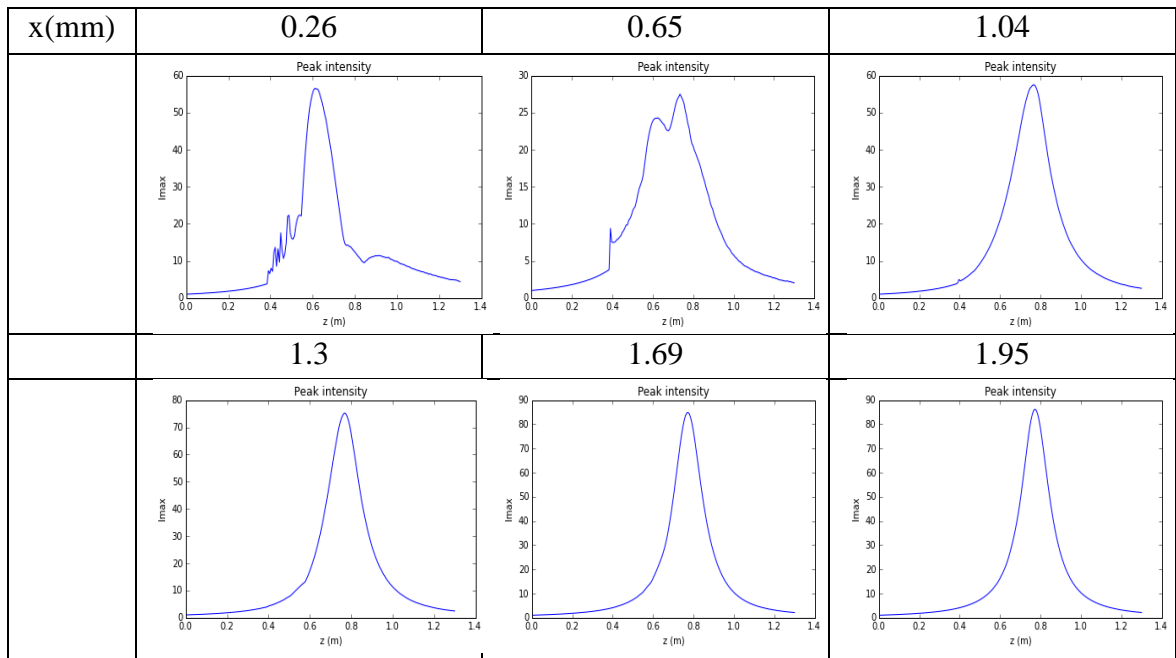


Figure 4.19: Maximum intensity profile for a Gaussian beam with $w_g=2.26\text{mm}$, which propagates in the presence of a circular glass with different position x in x direction in every case ($x=0.26\text{mm}$, 0.65mm , 1.04mm , 1.3mm , 1.69mm , 1.95mm).

Figure 4.19 depicts maximum intensity profile of the propagated Gaussian beam for different values of the obstacle position in x direction (x). It is shown that for higher values of x , the numerical and the theoretical maximum intensity profile have small discrepancy. For lower values of the obstacle position in x direction, the discrepancy between the numerical and the theoretical maximum intensity profile is larger. For the case which the obstacle position in x direction is equal to $x=0.26\text{mm}$, a large amount of the Gaussian beam passes through the glass obstacle and the intensity of the beam has a low value. For higher values of x ($x>1.04\text{mm}$), a small amount of the beam passes through the glass obstacle and the intensity of the beam is higher than in the previous case.

4.3 Perfectly absorbing propagation of a Ring-Airy beam in the presence of a circular block

a. Variable size

We consider an Airy Ring beam with radius $r_0=1\text{mm}$ and the corresponding constants are $w_0=0.13\text{mm}$ and $\alpha=0.1$, where $\lambda=0.8\ \mu\text{m}$. The propagation distance z is $1.3\ \text{m}$. In the following simulations the transverse coordinates (x,y) are discretized to 1024×1024 sampling points while 200 steps are used for the propagation along z direction. We put an obstacle (circular block) at the center $(x=0,y=0)$ of x,y directions and at the middle between $z=0$ and the focus point of the Ring-Airy beam. At following graphs, we present the radial intensity profile of this Airy Ring beam and the results of numerical simulation of the propagation of the Ring-Airy beam in the cases which the obstacle width D is different for every case. ($D= 2*r_0/3, r_0, 2*r_0, 2*(r_0+3w_0), 2*(r_0+7w_0), 2*(r_0+10w_0)$).

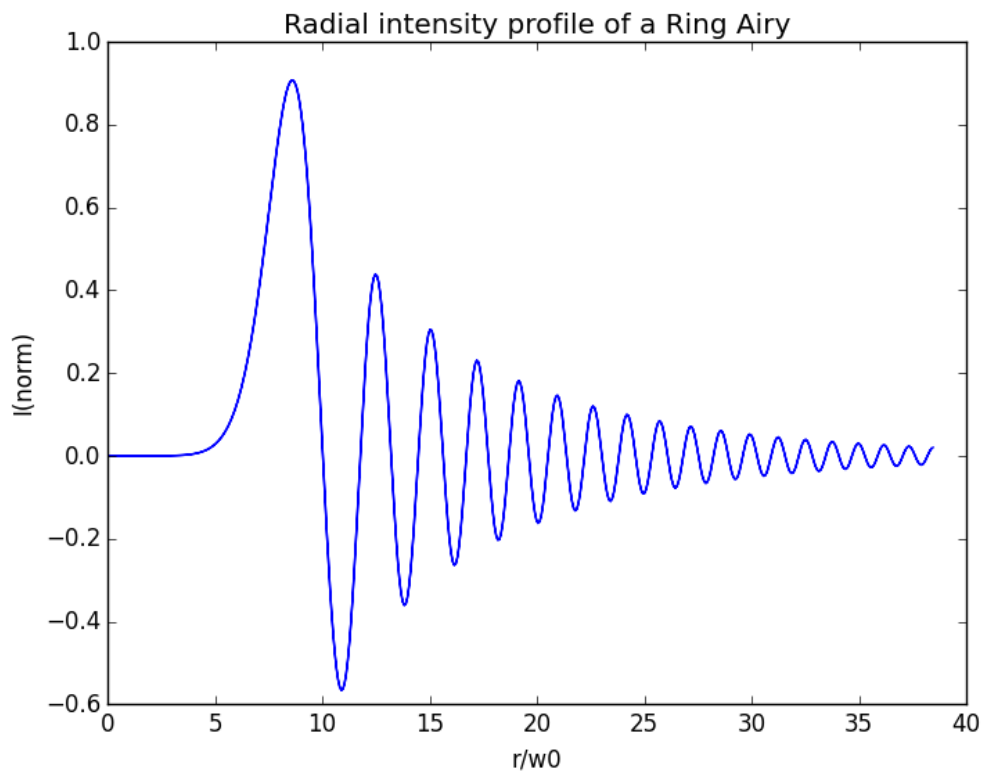


Figure 4.20: Radial intensity profile of a Ring Airy beam with radius $r_0=1\text{mm}$ and the corresponding constants are $w_0=0.13\text{mm}$ and $\alpha=0.1$

Figure 4.20 depicts the radial intensity profile of an Airy Ring beam with radius $r_0=1\text{mm}$ and the corresponding constants are $w_0=0.13\text{mm}$ and $a=0.1$. We observe that as the radius of the beam (r), which is normalized over the Airy Ring width (w_0), increases the radial intensity profile of the beam decreases. This result agrees with the rotationally symmetrical Airy distribution Equation (3.1).

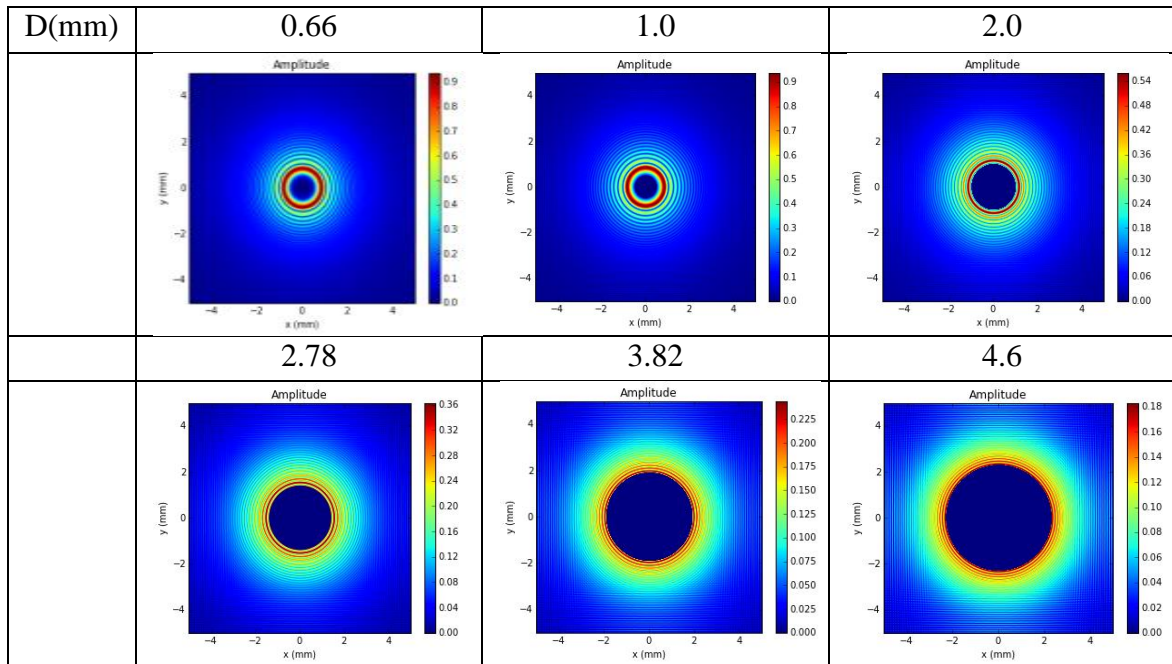


Figure 4.21: Beam amplitude after the circular block for an Airy Ring beam with $r_0=1\text{mm}$, $w_0=0.13\text{mm}$ and $a=0.1$ which propagates in the presence of a circular block with different size in every case ($D= 2*r_0/3, r_0, 2*r_0, 2*(r_0+3w_0), 2*(r_0+7w_0), 2*(r_0+10w_0)$).

Figure 4.21 depicts beam amplitude after the circular block for an Airy Ring beam with $a=0.1$. When the obstacle width is equal to $D=0.66\text{mm}$, we observe a small blue circle at the centre of the square. It represents the circular block which is situated at the middle between $z=0$ and the focus point of the Airy Ring beam. We observe that as the obstacle width increases, this blue circle which represents the obstacle also increases. We observe also that the values at color bars decrease as the obstacle width increases. This happens because the circular block cuts more energy which does not reach at the focus point of the beam, as the obstacle width increases.

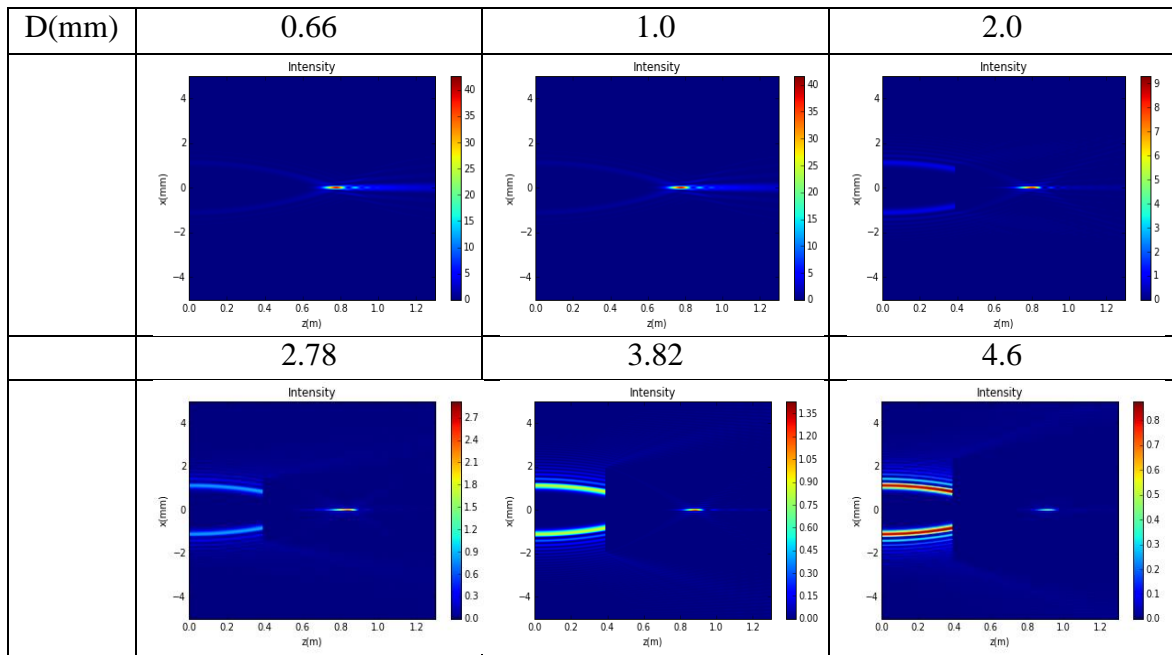


Figure 4.22: Intensity profile for an Airy Ring beam with $r_0=1\text{mm}$, $w_0=0.13\text{mm}$ and $a=0.1$ which propagates in the presence of a circular block with different size in every case ($D= 2*r_0/3, r_0, 2*r_0, 2*(r_0+3w_0), 2*(r_0+7w_0), 2*(r_0+10w_0)$).

Figure 4.22 depicts intensity profile of the propagated Airy Ring beam with $a=0.1$ for different values of size of the circular block (D). It is shown that for lower values of D , the beam focuses, whereas for higher values of D it scatters and deforms. For lower values of the obstacle width ($D < 2\text{mm}$), the intensity at the focus point of the beam has high value. This happens because if the obstacle width has low value, it cuts only a small amount of energy which does not reach at the focus point of the beam. For higher values of the obstacle width ($D > 2\text{mm}$), the intensity at the focus point of the Airy Ring beam has low value. This happens because the circular block cuts a large amount of the energy which does not reach at the focus point of the beam.

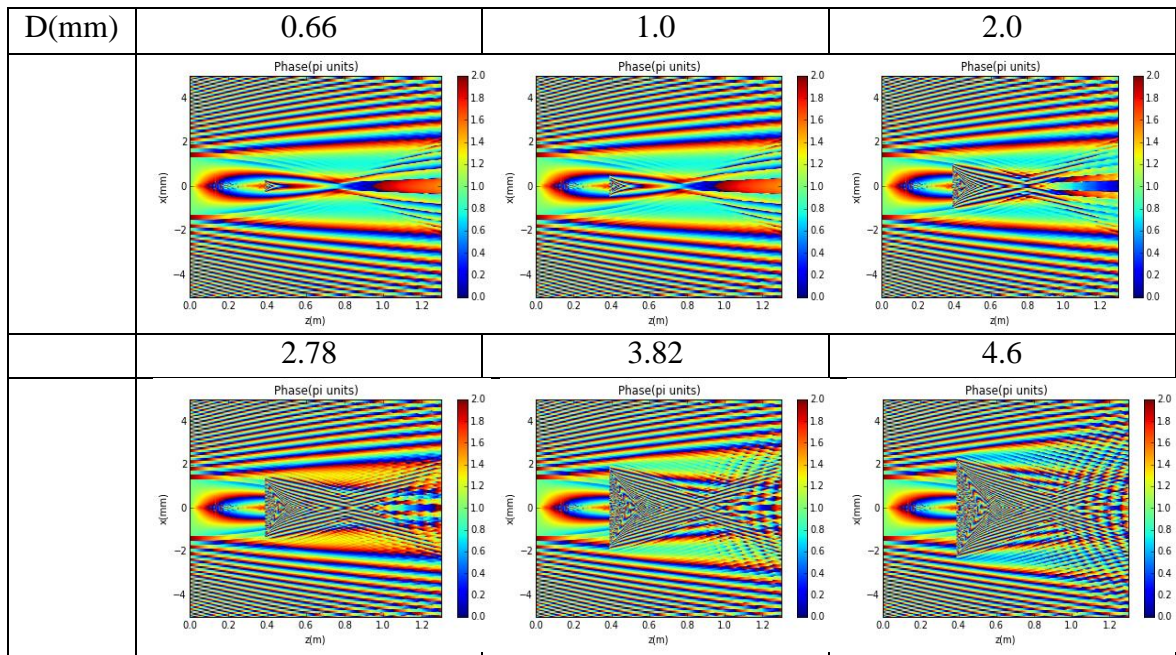


Figure 4.23: Phase profile for an Airy Ring beam with $r_0=1\text{mm}$, $w_0=0.13\text{mm}$ and $a=0.1$ which propagates in the presence of a circular block with different size in every case ($D= 2*r_0/3, r_0, 2*r_0, 2*(r_0+3w_0), 2*(r_0+7w_0), 2*(r_0+10w_0)$).

Figure 4.23 depicts phase profile of the propagated Airy Ring beam with $a=0.1$ for different values of size of the circular block (D). It is shown that for lower values of D , the beam focuses, whereas for higher values of D it scatters and deforms. We observe at the Figure how the phase of the beam changes as the size of the circular block increases. For high values of the size of the circular block ($D>2.0\text{mm}$), we observe some artifacts.

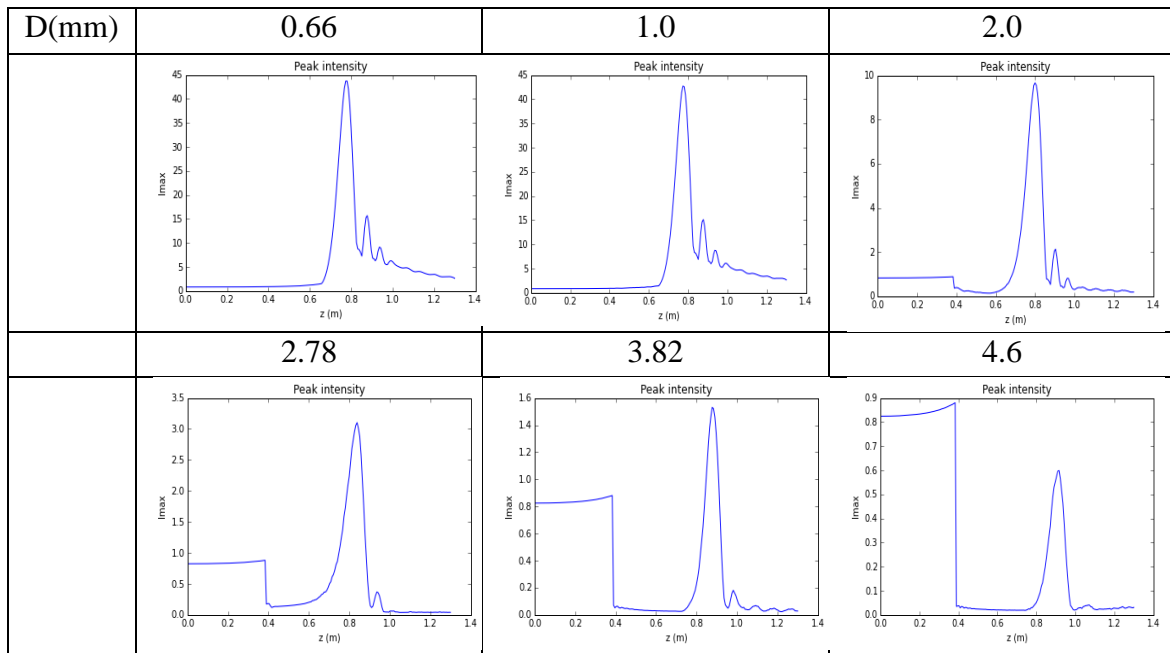


Figure 4.24: Maximum intensity profile for an Airy Ring beam with $r_0=1\text{mm}$, $w_0=0.13\text{mm}$ and $a=0.1$ which propagates in the presence of a circular block with different size in every case ($D= 2*r_0/3, r_0, 2*r_0, 2*(r_0+3w_0), 2*(r_0+7w_0), 2*(r_0+10w_0)$).

Figure 4.24 depicts maximum intensity profile of the propagated Airy Ring beam with $a=0.1$ for different values of size of the circular block (D). It is shown that for lower values of D , the numerical and the theoretical maximum intensity profile have small discrepancy. For higher values of the obstacle width (D), the discrepancy between the numerical and the theoretical maximum intensity profile is larger. For low values of the size of the circular block ($D=0.66\text{mm}, 1.0\text{mm}$), the intensity at the focus point of the beam has high value because the obstacle does not cut energy and all the energy reaches at the focus point of the beam. This happens because the size of the circular block has low value and the Airy Ring beam has a hole in the center of it so the obstacle does not cut energy of the beam. For higher values of the obstacle width ($D>2.0\text{mm}$) we observe that the circular block cuts energy which does not reach at the focus point of the beam. As the obstacle width increases, the intensity at the point which the obstacle is situated is also increased. Interestingly, for $D=4.6\text{mm}$, the intensity at the point which the obstacle is situated is higher than the intensity in the focus point of the beam. This happens because in that case the obstacle has a high value of size and it cuts a large amount of energy which does not reach at the focus point of the beam.

Next, we follow the same steps as previous with an Airy Ring beam with the same radius and width as previous, ($r_0=1\text{mm}$, $w_0=0.13\text{mm}$) but with a different exponential decay factor which is equal to $a=0.15$ in that case. In the following simulations the transverse coordinates (x,y) are discretized to 1024×1024 sampling points while 200 steps are used for the propagation along z direction. The radial intensity profiles of these Airy Ring beams are presented in Figure 4.25 and the results of numerical simulation are presented in Figures 4.26, 4.27, 4.28 and 4.29.

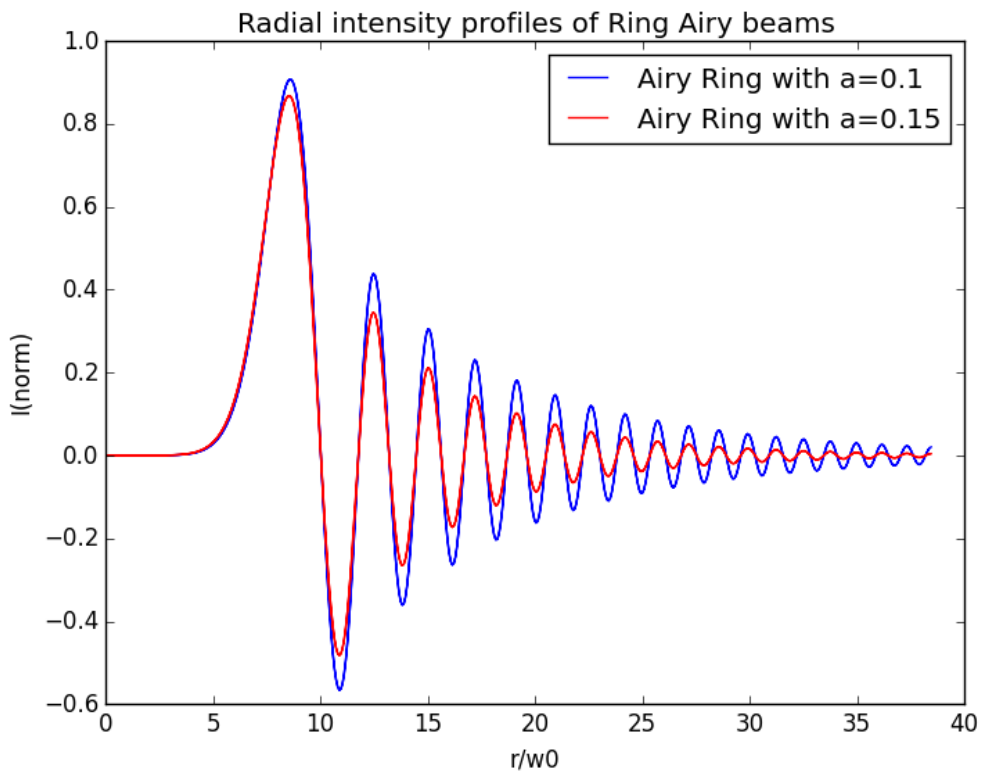


Figure 4.25: Comparison of radial intensity profiles of two Airy Ring beams with the same radius and width ($r_0=1\text{mm}$, $w_0=0.13\text{mm}$) but with a different exponential decay factor where in the first case is equal to $a=0.1$ and in the second case is equal to $a=0.15$.

Figure 4.25 depicts the radial intensity profiles of two different Airy Ring beams. These two beams have the same radius which is equal to $r_0=1\text{mm}$, the same width which is equal to $w_0=0.13\text{mm}$ but different exponential decay factors where in the first case is equal to $a=0.1$ and in the second case is equal to $a=0.15$. We observe that as the exponential decay factor of an Airy Ring beam increases, its radial intensity profile decreases. This result agrees with the rotationally symmetrical Airy distribution Equation (3.1).

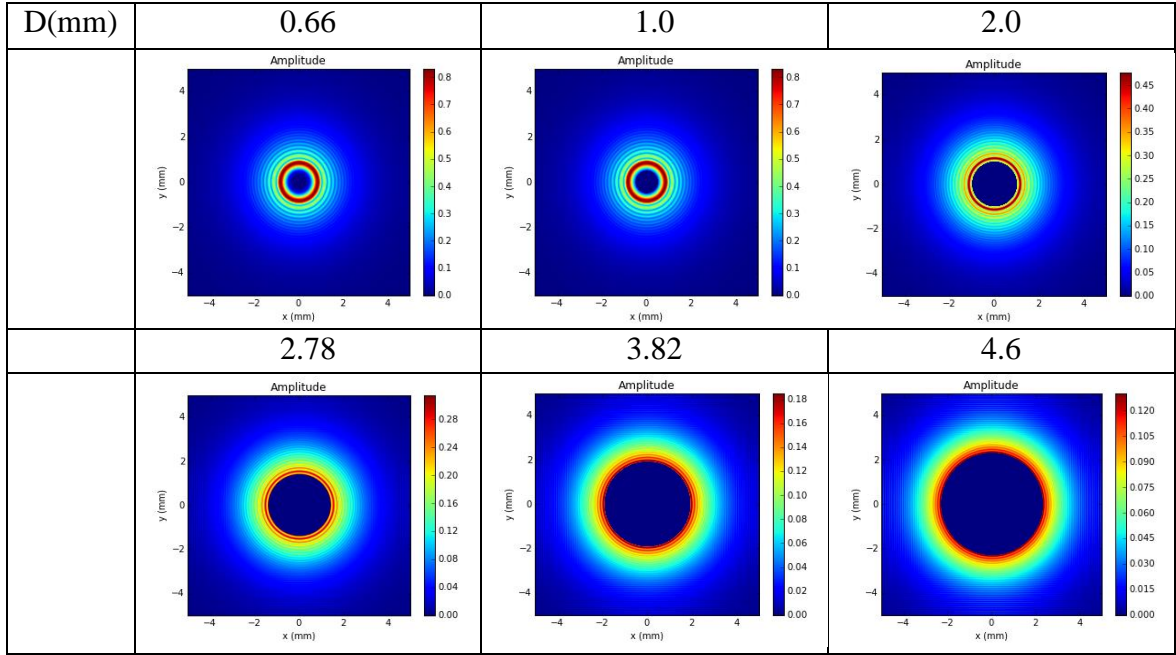


Figure 4.26: Beam amplitude after the circular block for an Airy Ring beam with $r_0=1\text{mm}$, $w_0=0.13\text{mm}$ and $a=0.15$ which propagates in the presence of a circular block with different size in every case ($D=2*r_0/3, r_0, 2*r_0, 2*(r_0+3w_0), 2*(r_0+7w_0), 2*(r_0+10w_0)$).

Figure 4.26 depicts beam amplitude after the circular block for an Airy Ring beam with $a=0.15$. When the obstacle width is equal to $D=0.66\text{mm}$, we observe a small blue circle at the centre of the square. It represents the circular block which is situated at the middle between $z=0$ and the focus point of the Airy Ring beam. We observe that as the obstacle width increases, this blue circle which represents the obstacle also increases. We observe also that the values at colorbar decrease as the obstacle width increases. This happens because the circular block cuts more energy which does not reach at the focus point of the beam, as the obstacle width increases. If we compare Figure 4.20 with the Figure 4.25, we observe that for the same values of obstacle width, the values at colorbar for the Airy Ring beam with $a=0.1$ are higher than the values at colorbar for the Airy Ring beam with $a=0.15$.

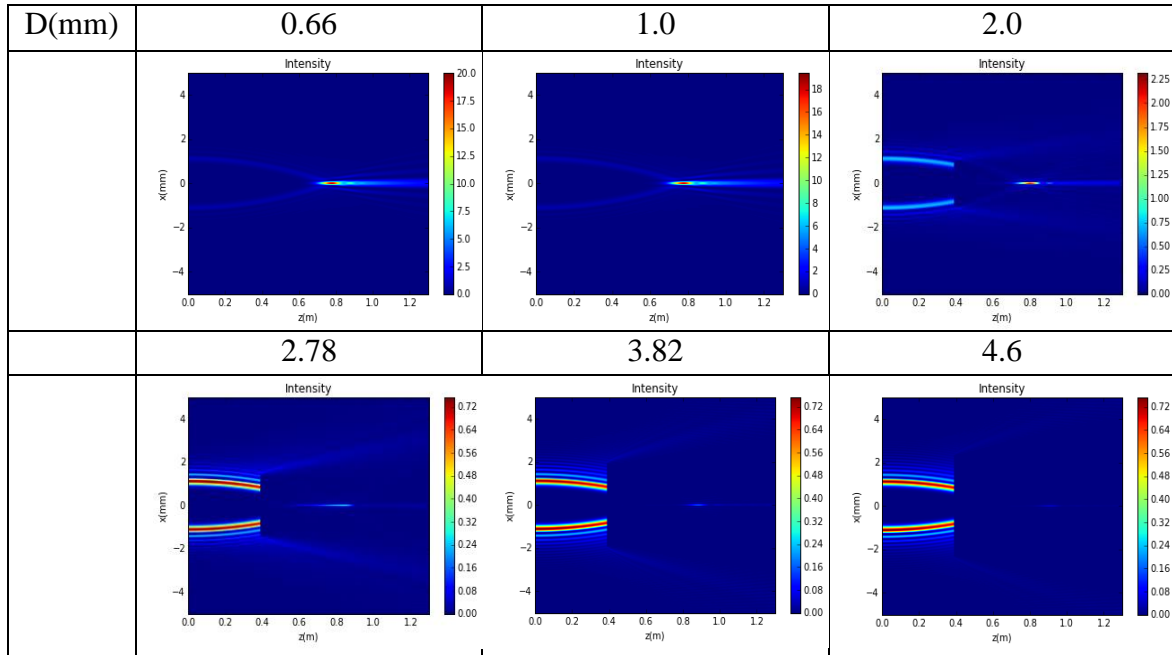


Figure 4.27: Intensity profile for an Airy Ring beam with $r_0=1\text{mm}$, $w_0=0.13\text{mm}$ and $a=0.15$ which propagates in the presence of a circular block with different size in every case ($D=2*r_0/3, r_0, 2*r_0, 2*(r_0+3w_0), 2*(r_0+7w_0), 2*(r_0+10w_0)$).

Figure 4.27 depicts intensity profile of the propagated Airy Ring beam with $a=0.15$ for different values of size of the circular block (D). It is shown that for lower values of D , the beam focuses, whereas for higher values of D it scatters and deforms. For lower values of the obstacle width ($D < 2\text{mm}$), the intensity at the focus point of the beam has high values. This happens because if the obstacle width has low value, it cuts only a small amount of energy which does not reach at the focus point of the beam. For higher values of the obstacle width ($D > 2\text{mm}$), the intensity at the focus point of the Airy Ring beam has low value. This happens because the circular block cuts a large amount of the energy which does not reach at the focus point of the beam. If we compare Figure 4.21 with the Figure 4.26, we observe that for the same values of obstacle width, the values at colorbar for the Airy Ring beam with $a=0.1$ are higher than the values at colorbar for the Airy Ring beam with $a=0.15$.

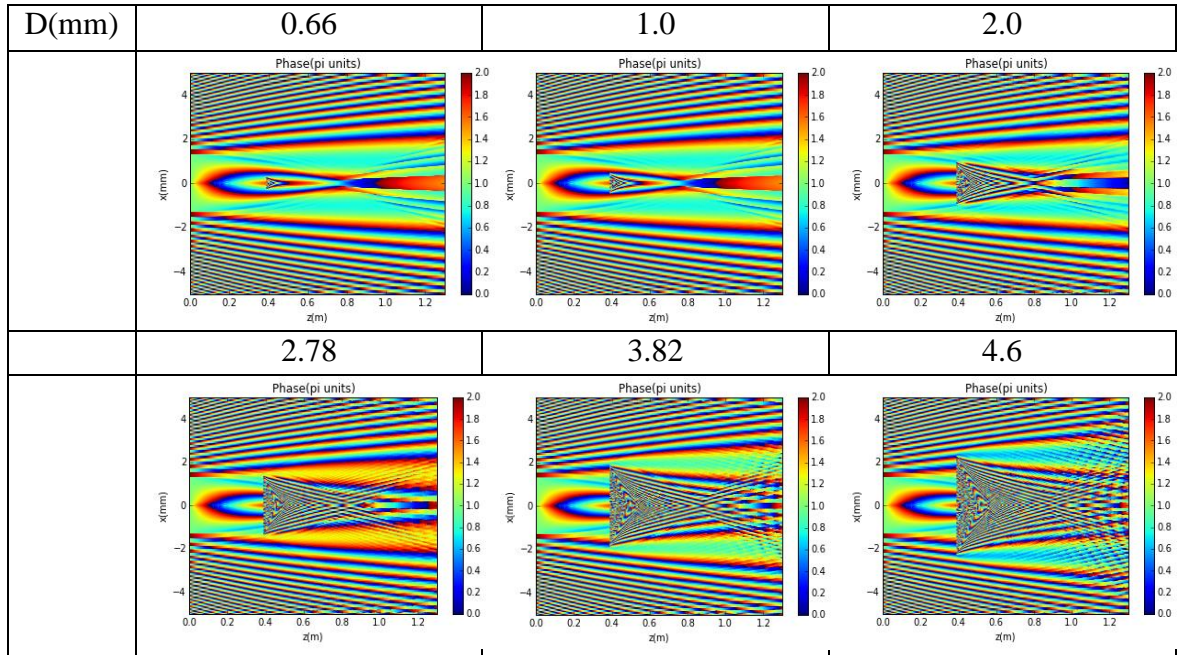


Figure 4.28: Phase profile for an Airy Ring beam with $r_0=1\text{mm}$, $w_0=0.13\text{mm}$ and $a=0.15$ which propagates in the presence of a circular block with different size in every case ($D=2*r_0/3, r_0, 2*r_0, 2*(r_0+3w_0), 2*(r_0+7w_0), 2*(r_0+10w_0)$).

Figure 4.28 depicts phase profile of the propagated Airy Ring beam with $a=0.15$ for different values of size of the circular block (D). It is shown that for lower values of D , the beam focuses, whereas for higher values of D it scatters and deforms. We observe at the Figure how the phase of the beam changes as the size of the circular block increases. For high values of the size of the circular block ($D>2.0\text{mm}$), we observe some artifacts.

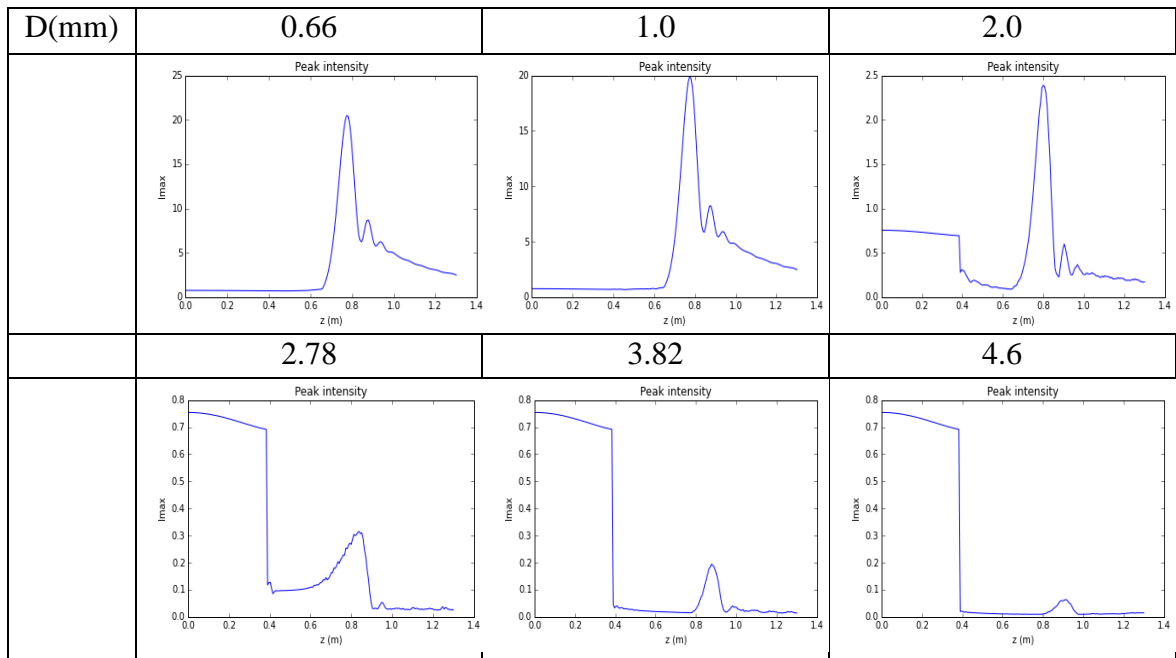


Figure 4.29: Maximum intensity profile for an Airy Ring beam with $r_0=1\text{mm}$, $w_0=0.13\text{mm}$ and $a=0.15$ which propagates in the presence of a circular block with different size in every case ($D= 2*r_0/3, r_0, 2*r_0, 2*(r_0+3w_0), 2*(r_0+7w_0), 2*(r_0+10w_0)$).

Figure 4.29 depicts maximum intensity profile of the propagated Airy Ring beam with $a=0.15$ for different values of size of the circular block (D). It is shown that for lower values of D , the numerical and the theoretical maximum intensity profile have small discrepancy. For higher values of the obstacle width (D), the discrepancy between the numerical and the theoretical maximum intensity profile is larger. For low values of the size of the circular block ($D=0.66\text{mm}$, 1.0mm), the intensity at the focus point of the beam has high value because the obstacle does not cut energy and all the energy reaches at the focus point of the beam. This happens because the size of the circular block has low value and the Airy Ring beam has a hole in the center of it so the obstacle does not cut energy of the beam. For higher values of the obstacle width ($D>2.0\text{mm}$) we observe that the circular block cuts energy which does not reach at the focus point of the beam. As the obstacle width increases, the intensity at the focus point of the beam decreases. Interestingly, for $D>2.0\text{mm}$, the intensity at the point which the obstacle is situated is higher than the intensity in the focus point of the beam. This happens because in that case the obstacle has a high value of size and it cuts a large amount of energy which does not reach at the focus point of the beam. If we compare Figure 4.23 with the Figure 4.28, we observe that for the same values of obstacle width, the values of peak intensity at the focus point of the beam for the

Airy Ring beam with $a=0.1$ are higher than the values of peak intensity at the focus point of the beam for the Airy Ring beam with $a=0.15$.

In order to present our simulations results we define two metrics. The first metric is the percentage change of focus contrast data results ($\Delta I(\%)$) which is defined in Equation (4.1).

$$\Delta I(\%) = \left(1 - \frac{I_{\max}}{(I_{\max})_{ref}} \right) \bullet 100 \quad (4.1)$$

where $(I_{\max})_{ref}$ represents the intensity peak when there is not obstacle. If ΔI is 100% then the intensity peak drops to 0 and we have too many loses. On the other hand if ΔI is 0% then the intensity peak drops to $(I_{\max})_{ref}$ and the loses drop to 0. The second metric is the percentage change of focus position data results ($\Delta P(\%)$) which is defined in Equation (4.2).

$$\Delta P(\%) = \left(1 - \frac{P}{P_{ref}} \right) \bullet 100 \quad (4.2)$$

where P represents the focus position and P_{ref} represents the focus position when there is not obstacle. If ΔP is 100% then the focus position P drops to 0. On the other hand if ΔP is 0% then the focus position P drops to P_{ref} .

In Figure 4.30, we compare the percentage change of focus contrast data results ($\Delta I(\%)$), as it is defined in Equation (4.1), from Airy Ring and Gaussian simulations as a function of the obstacle width (D), which is normalized over the ring radius of the Airy Ring beam (r_0+w_0).

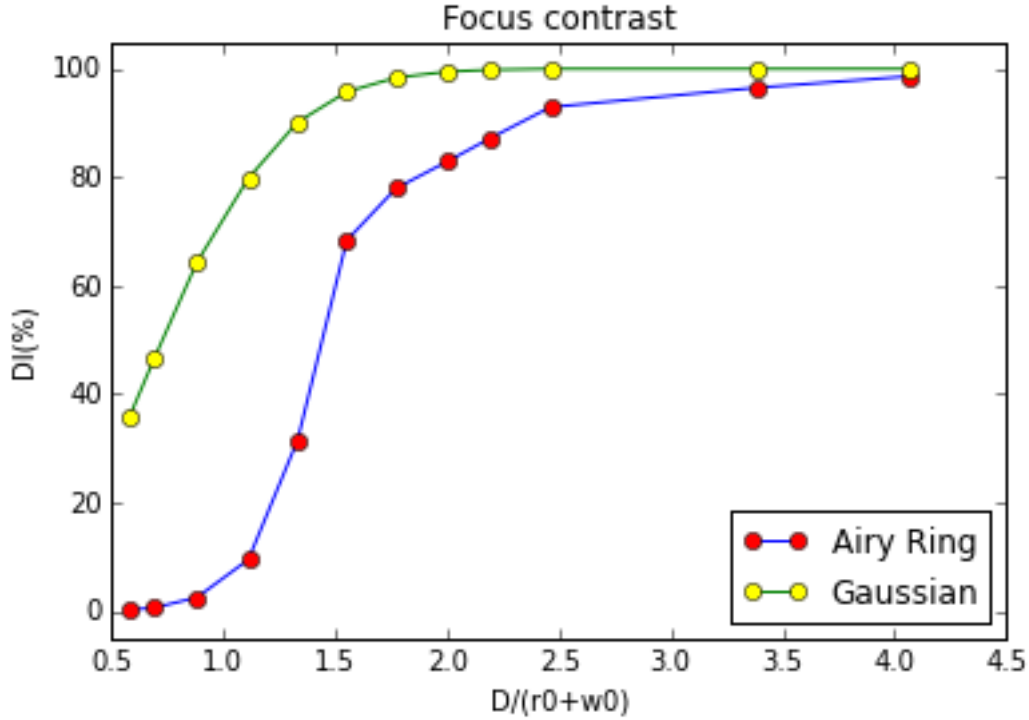


Figure 4.30: Comparison of the percentage change of focus contrast data results (ΔI (%)) from Airy Ring and Gaussian simulations as a function of the obstacle width (D), which is normalized over the ring radius of the Airy Ring beam (r_0+w_0).

In Figure 4.30 the values of the percentage change of focus contrast data results (ΔI (%)) from Airy Ring and Gaussian simulations have bigger difference for lower values of the normalized obstacle width (D). For higher values of the normalized obstacle width (D) the ΔI (%) values tend to stabilize around $\Delta I \sim 100\%$. We observe that the Airy Ring beam is better than the Gaussian beam because for low values of the normalized obstacle width (D), the percentage change of focus contrast data results and so the losses have lower value for the Airy Ring beam than for the Gaussian beam. For higher values of the normalized obstacle width (D), the percentage change of focus contrast data results (ΔI (%)) has the same value for the two beams. As a result, in this case the Airy Ring beam is better than the Gaussian beam.

Finally, in Figure 4.31, we compare the percentage change of focus position data results (ΔP (%)), as it is defined in Equation (4.2), from Airy Ring and Gaussian simulations as a function of the obstacle width (D), which is normalized over the ring radius of the Airy Ring beam (r_0+w_0).

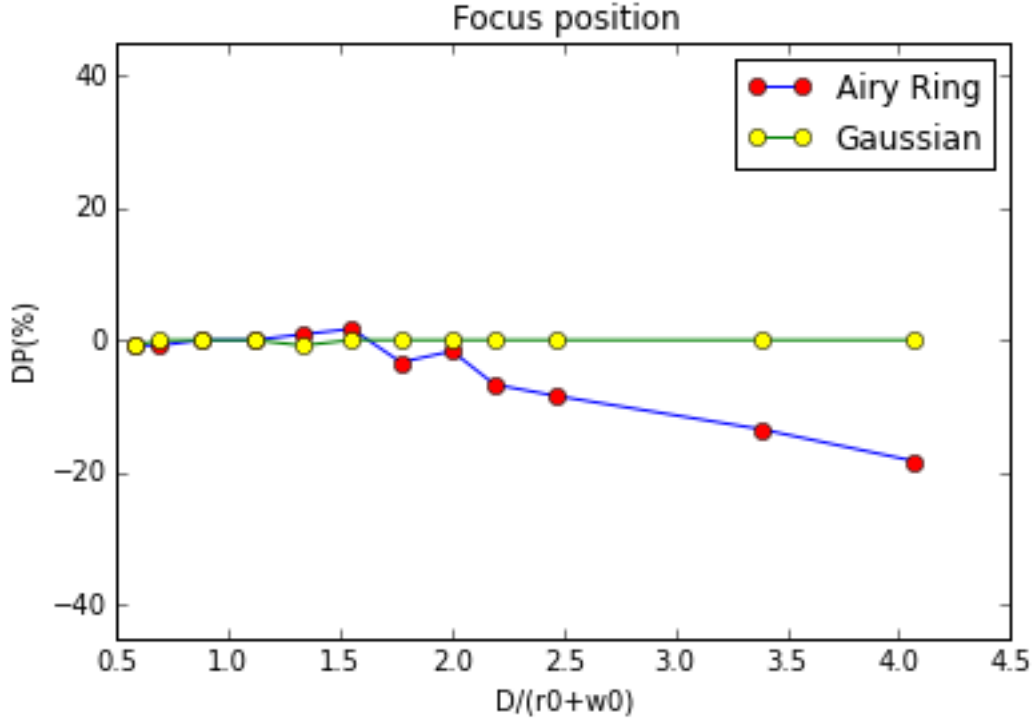


Figure 4.31: Comparison of the percentage change of focus position data results (ΔP (%)) from Airy Ring and Gaussian simulations as a function of the obstacle width (D), which is normalized over the ring radius of the Airy Ring beam (r_0+w_0).

In Figure 4.31 the percentage change of focus position data results (ΔP (%)) from Airy Ring and Gaussian simulations have around the same values for lower values of the normalized obstacle width (D). Interestingly, at higher values of the normalized obstacle width (D), Airy Ring beams exhibit considerably lower percentage change of focus position data results, compared to the Gaussian beams. In this case, the focus position of Gaussian beam drops to P_{ref} as it is defined in Equation (4.2), for all the values of the normalized obstacle width (D). The focus position of Airy Ring beam drops to P_{ref} for lower values of the normalized obstacle width (D), but for higher values of the normalized obstacle width (D), the focus position of the beam has higher value than the P_{ref} value of the Airy Ring beam.

b. Variable longitudinal position

We consider an Airy Ring beam with radius $r_0=1\text{mm}$ and the corresponding constants are $w_0=0.13\text{mm}$ and $\alpha=0.1$, where $\lambda=0.8 \mu\text{m}$. The propagation distance z is

1.3 m. In the following simulations the transverse coordinates (x,y) are discretized to 1024x1024 sampling points while 200 steps are used for the propagation along z direction. We put an obstacle (circular block) at the center (x=0,y=0) of x,y directions. The obstacle width is equal to $2*r_0$. At following graphs, we present the results of numerical simulation of the propagation of the Ring-Airy beam in the cases which the obstacle position z in z direction is different for every case. The obstacle position z varies from the point z=0 up to Ring-Airy focus point. (z=100.0mm, 200.0mm, 390.0mm, 500.0mm, 600.0mm, 700.0mm).

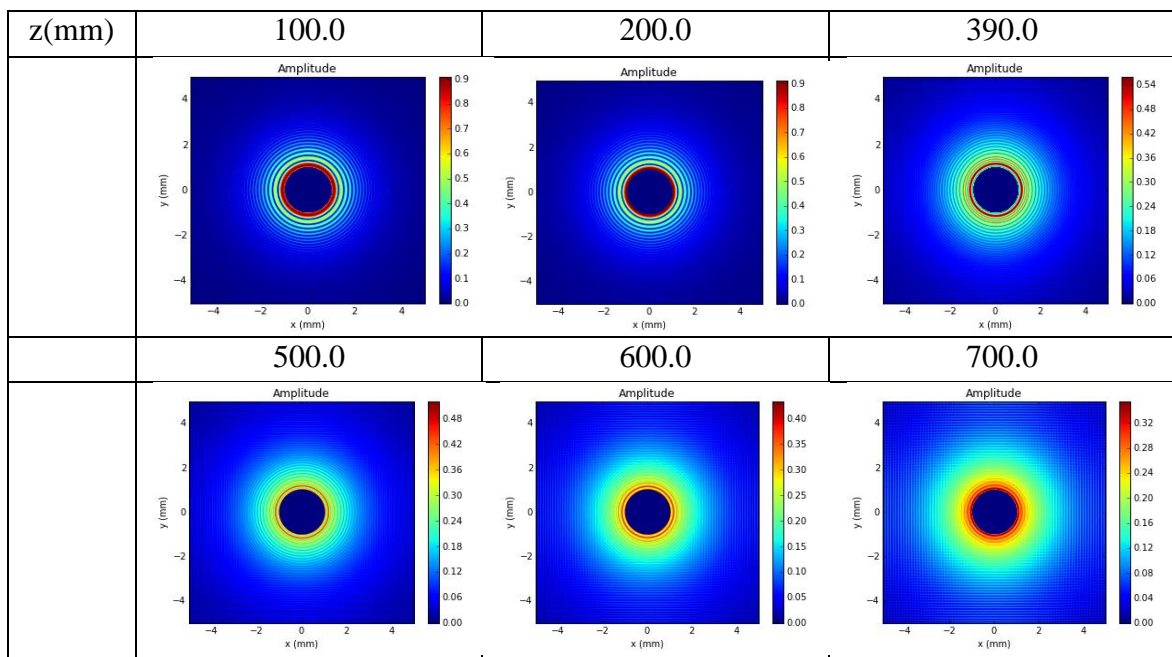


Figure 4.32: Beam amplitude after the circular block for an Airy Ring beam with $r_0=1\text{mm}$, $w_0=0.13\text{mm}$ and $a=0.1$ which propagates in the presence of a circular block with different position z in z direction in every case (z=100.0mm, 200.0mm, 390.0mm, 500.0mm, 600.0mm, 700.0mm).

Figure 4.32 depicts beam amplitude after the circular block for an Airy Ring beam. In this Figure we observe that the circle in the centre of the blue square has constant width because the circular block has constant width but its position in z direction is different in every case. Interestingly as the position of the obstacle width in z direction increases, the values in the colorbars decrease. This happens because as the obstacle moves near to the focus point of the Airy Ring beam, it cuts more energy which does not reach to the focus point of the beam.

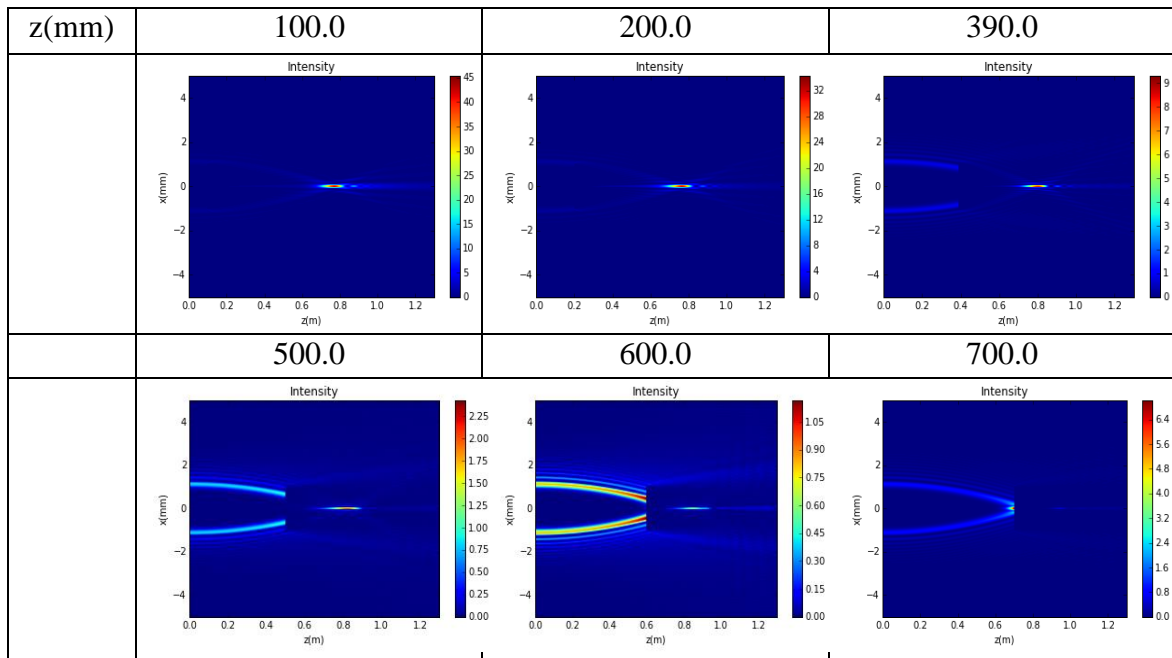


Figure 4.33: Intensity profile for an Airy Ring beam with $r_0=1\text{mm}$, $w_0=0.13\text{mm}$ and $a=0.1$ which propagates in the presence of a circular block with different position z in z direction in every case ($z=100.0\text{mm}$, 200.0mm , 390.0mm , 500.0mm , 600.0mm , 700.0mm).

Figure 4.33 depicts intensity profile of the propagated Airy Ring beam for different values of position of the circular block in z direction (z). It is shown that for lower values of z , the beam focuses, whereas for higher values of z it scatters and deforms. For lower values of the obstacle position in z direction ($z < 390\text{mm}$), the intensity at the focus point of the beam has high value because the obstacle is far away from the focus point of the beam and it does not cut so much energy. For higher values of the obstacle position in z direction ($z > 390\text{mm}$), the intensity at the focus point of the Airy Ring beam has lower value. This happens because the circular block cuts too much energy which does not reach at the focus point of the beam.

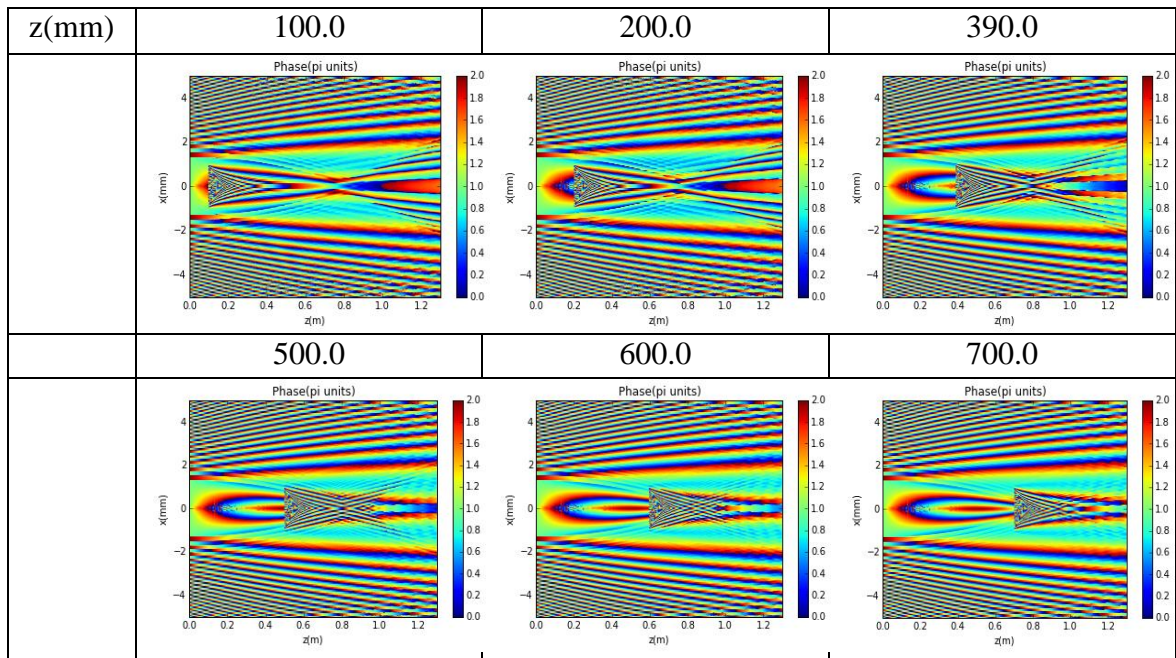


Figure 4.34: Phase profile for an Airy Ring beam with $r_0=1\text{mm}$, $w_0=0.13\text{mm}$ and $a=0.1$ which propagates in the presence of a circular block with different position z in z direction in every case ($z=100.0\text{mm}$, 200.0mm , 390.0mm , 500.0mm , 600.0mm , 700.0mm).

Figure 4.34 depicts phase profile of the propagated Airy Ring beam for different values of obstacle position in z direction (z). It is shown that for lower values of z , the beam focuses, whereas for higher values of z it scatters and deforms. We observe at the Figure how the phase of the beam changes as the position in z direction of the circular block increases. For high values of the position in z direction of the circular block ($z>390.0\text{mm}$), we observe some artifacts.

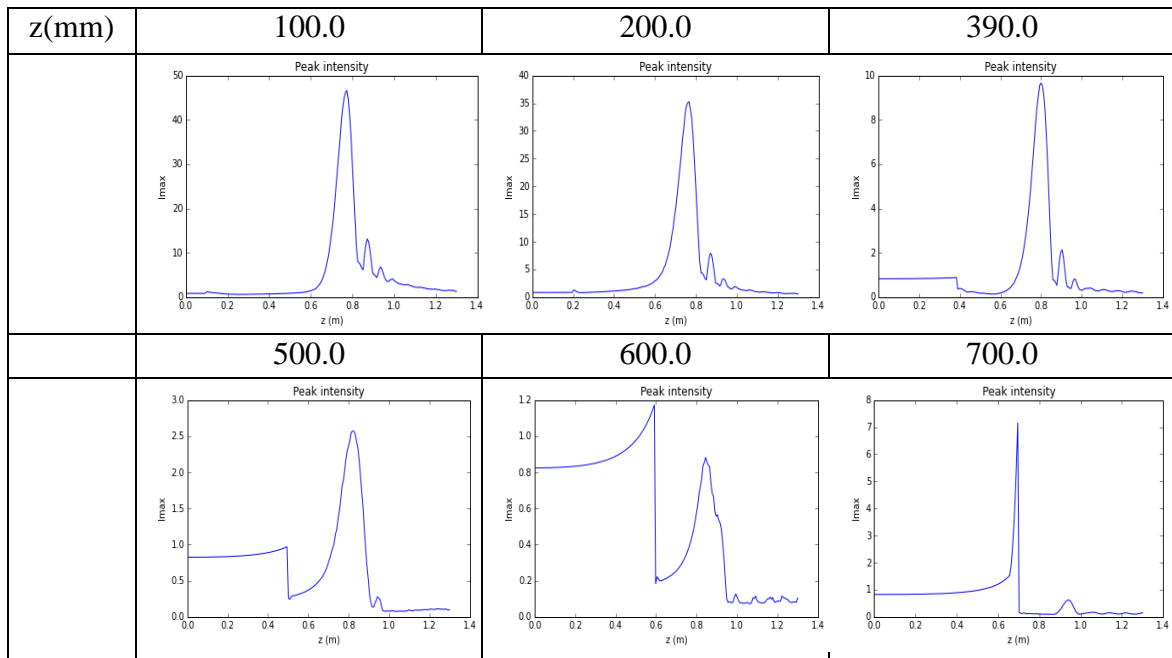


Figure 4.35: Maximum intensity profile for an Airy Ring beam with $r_0=1\text{mm}$, $w_0=0.13\text{mm}$ and $a=0.1$ which propagates in the presence of a circular block with different position z in z direction in every case ($z=100.0\text{mm}$, 200.0mm , 390.0mm , 500.0mm , 600.0mm , 700.0mm).

Figure 4.35 depicts maximum intensity profile of the propagated Airy Ring beam for different values of position in z direction of the circular block (z). It is shown that for lower values of z , the numerical and the theoretical maximum intensity profile have small discrepancy. For higher values of the obstacle position in z direction (z), the discrepancy between the numerical and the theoretical maximum intensity profile is larger. For low values of the position in z direction of the circular block ($z=100.0\text{mm}$, 200.0mm), the intensity at the focus point of the beam has high value because the obstacle does not cut energy and all the energy reaches at the focus point of the beam. For higher values of the obstacle position in z direction ($z>200.0\text{mm}$) we observe that the circular block cuts energy which does not reach at the focus point of the beam. As the obstacle position in z direction increases, the intensity at the focus point of the beam decreases and the intensity at the point which the obstacle is situated increases. Interestingly, for $z>500.0\text{mm}$, the intensity at the point which the obstacle is situated is higher than the intensity at the focus point of the beam. This happens because in that case the obstacle cuts a large amount of energy which does not reach at the focus point of the beam.

In Figure 4.36, we compare the percentage change of focus contrast data results (ΔI (%)), as it is defined in Equation (4.1), from Airy Ring and Gaussian simulations as a

function of z position of the obstacle (z), which is normalized over the Airy Ring focal distance (f_0).

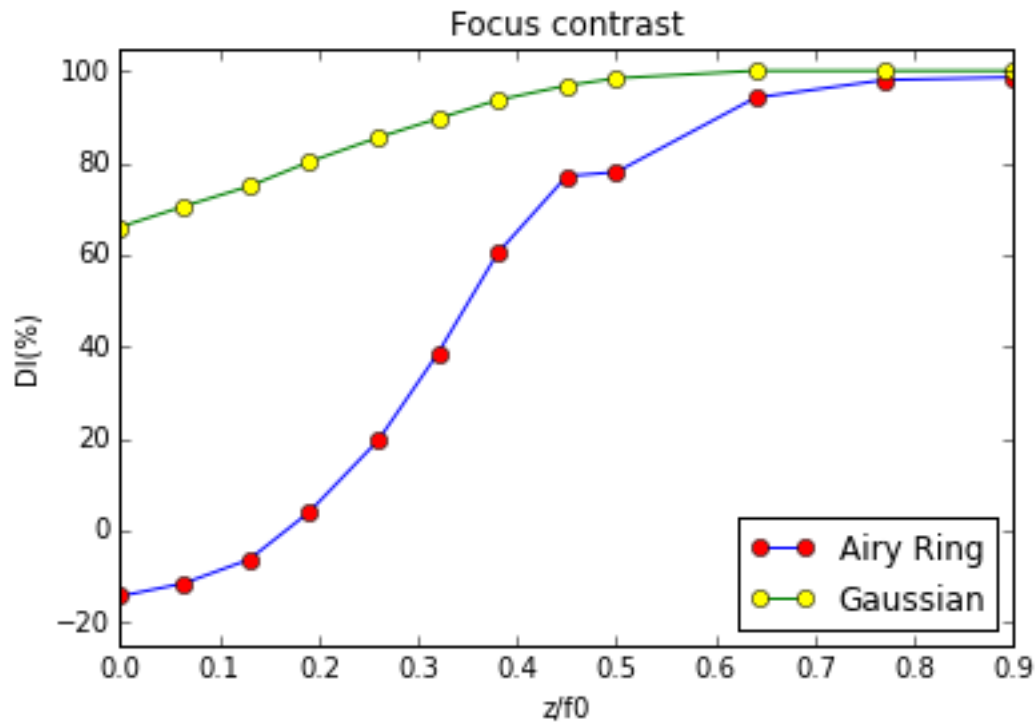


Figure 4.36: Comparison of the percentage change of focus contrast data results (ΔI (%)) from Airy Ring and Gaussian simulations as a function of z position of the obstacle (z), which is normalized over the Airy Ring focal distance (f_0).

In Figure 4.36 the values of the percentage change of focus contrast data results (ΔI (%)) from Airy Ring and Gaussian simulations have bigger difference for lower values of the normalized obstacle position in z direction (z). For higher values of the normalized obstacle position in z direction (z) the ΔI (%) values tend to stabilize around $\Delta I \sim 100\%$. We observe that the Airy Ring beam is better than the Gaussian beam because for low values of the normalized obstacle position in z direction (z), the percentage change of focus contrast data results and so the losses have lower value for the Airy Ring beam than for the Gaussian beam. For higher values of the normalized obstacle position in z direction (z), the percentage change of focus contrast data results (ΔI (%)) has the same value for the two beams. As a result, in this case the Airy Ring beam is better than the Gaussian beam.

Finally, in Figure 4.37, we compare the percentage change of focus position data results (ΔP (%)), as it is defined in Equation (4.2), from Airy Ring and Gaussian

simulations as a function of z position of the obstacle (z), which is normalized over the Airy Ring focal distance (f_0).

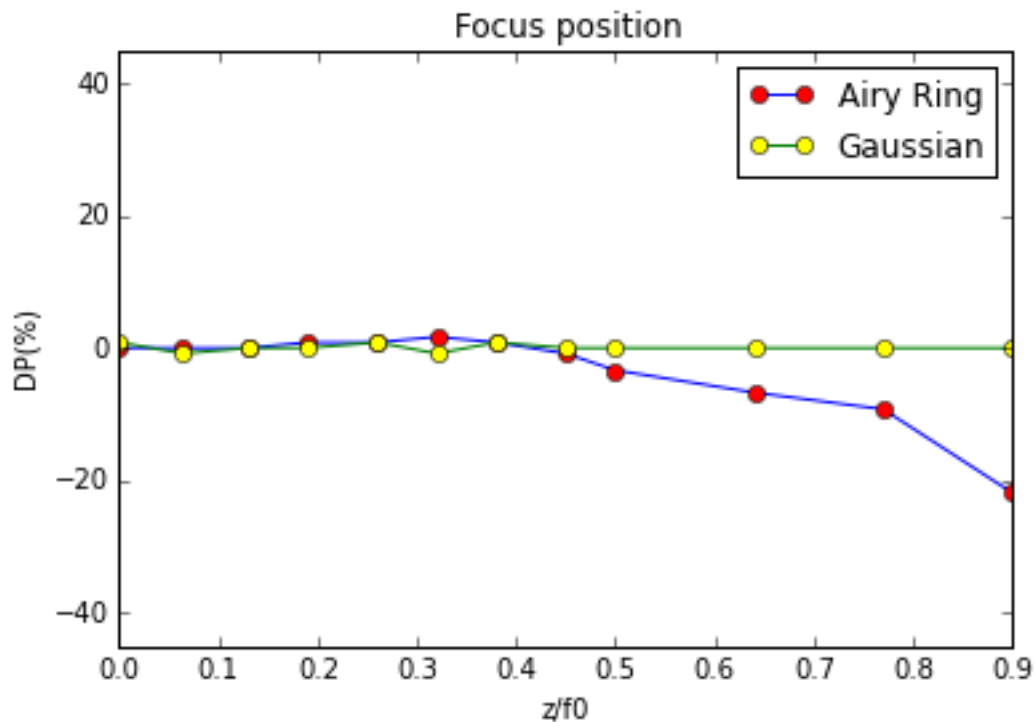


Figure 4.37: Comparison of the percentage change of focus position data results (ΔP (%)) from Airy Ring and Gaussian simulations as a function of z position of the obstacle (z), which is normalized over the Airy Ring focal distance (f_0).

In Figure 4.37 the percentage change of focus position data results ($\Delta P(\%)$) from Airy Ring and Gaussian simulations have around the same values for lower values of the normalized obstacle position in z direction (z). Interestingly, at higher values of the normalized obstacle position in z direction (z), Airy Ring beams exhibit considerably lower percentage change of focus position data results, compared to the Gaussian beams. In this case, the focus position of Gaussian beam drops to P_{ref} as it is defined in Equation (4.2), for all the values of the normalized obstacle position in z direction (z). The focus position of Airy Ring beam drops to P_{ref} for lower values of the normalized obstacle position in z direction (z), but for higher values of the normalized obstacle position in z direction (z), the focus position of the beam has higher value than the P_{ref} value of the Airy Ring beam.

c. Variable transverse position

The next step is to study the propagation of the same Ring-Airy beam as previous in which the circular block has the same width as before ($2*r_0$) and we have put it in the middle between $z=0$ and the Ring-Airy focus point. In these simulations the transverse coordinates (x,y) are also discretized to 1024×1024 sampling points while 200 steps are used for the propagation along z direction. At following graphs, we present the results of numerical simulation of the propagation of the Ring-Airy beam in the cases which the obstacle position x in x direction is different for every case. ($x=0.26\text{mm}, 0.65\text{mm}, 1.04\text{mm}, 1.3\text{mm}, 1.69\text{mm}, 1.95\text{mm}$).

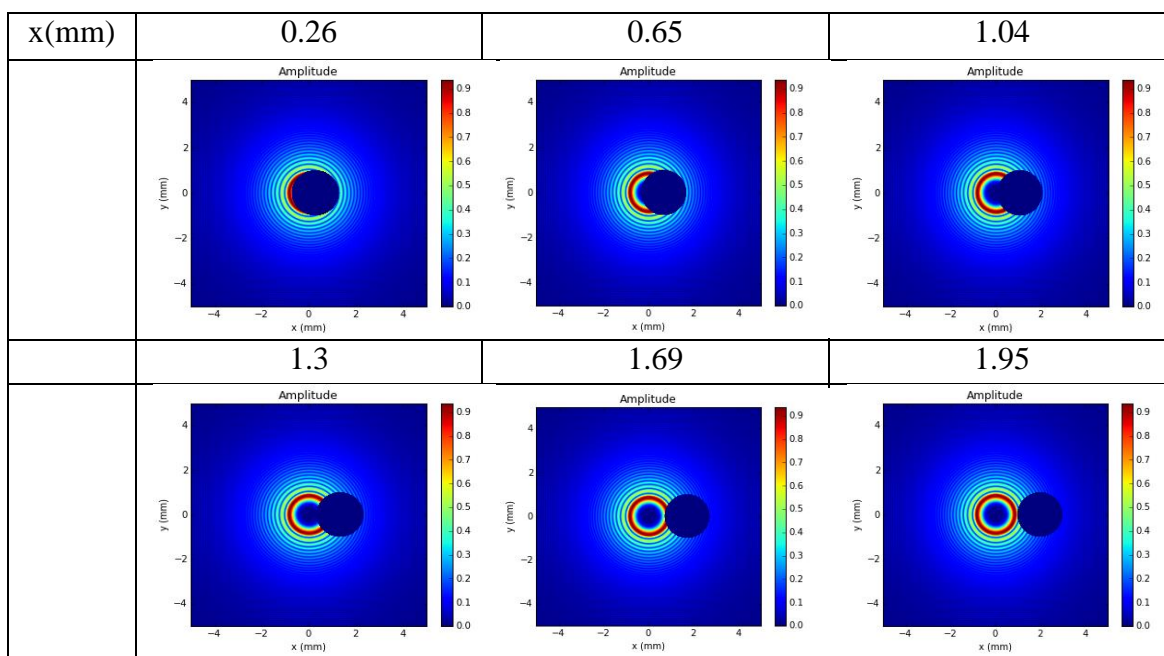


Figure 4.38: Beam amplitude after the circular block for an Airy Ring beam with $r_0=1\text{mm}$, $w_0=0.13\text{mm}$ and $a=0.1$ which propagates in the presence of a circular block with different position x in x direction in every case ($x=0.26\text{mm}, 0.65\text{mm}, 1.04\text{mm}, 1.3\text{mm}, 1.69\text{mm}, 1.95\text{mm}$).

Figure 4.38 depicts beam amplitude after the circular block for an Airy Ring beam. In this Figure we observe a blue circle in the blue square which represents the circular block. When the obstacle position in x direction has a value of $x=0.26\text{mm}$, the obstacle has moved from the center of the beam a distance which is equal to 0.26mm . As the value of obstacle position in x direction (x) increases, the movement of the

circular block from the center of the beam also increases. This means that at low values of x , the obstacle cuts much energy which does not reach at the focus point of the beam. On the other hand for high values of x , the obstacle does not cut so much energy which finally reaches at the focus point of the beam.

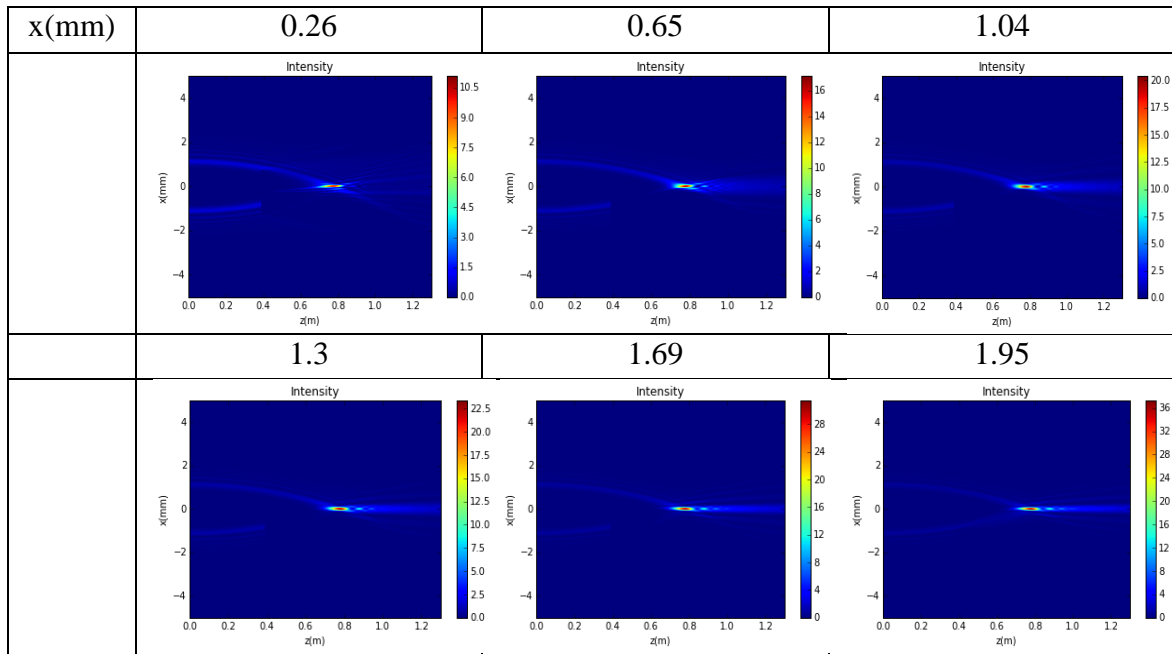


Figure 4.39: Intensity profile for an Airy Ring beam with $r_0=1\text{mm}$, $w_0=0.13\text{mm}$ and $a=0.1$ which propagates in the presence of a circular block with different position x in x direction in every case ($x=0.26\text{mm}$, 0.65mm , 1.04mm , 1.3mm , 1.69mm , 1.95mm).

Figure 4.39 depicts intensity profile of the propagated Airy Ring beam for different values of position of the circular block in x direction (x). It is shown that for lower values of x , the beam scatters and deforms, whereas for higher values of x it focuses. We observe in the Figure that when the obstacle position in x direction has a value which is equal to $x=0.26\text{mm}$, the obstacle cuts too much energy of the beam at the point which is situated. This energy does not reach at the focus point of the beam and this is the reason that we observe low values of intensity in the colorbar. As the obstacle moves in x direction, it cuts less energy at the point which is situated and finally more energy reaches at the focus point of the beam. For the case which the obstacle position in x direction has a value which is equal to $x=1.95\text{mm}$, much energy reaches at the focus point of the beam because the obstacle does not cut it at the point which is situated and we observe that the intensity values at colorbar have high values.

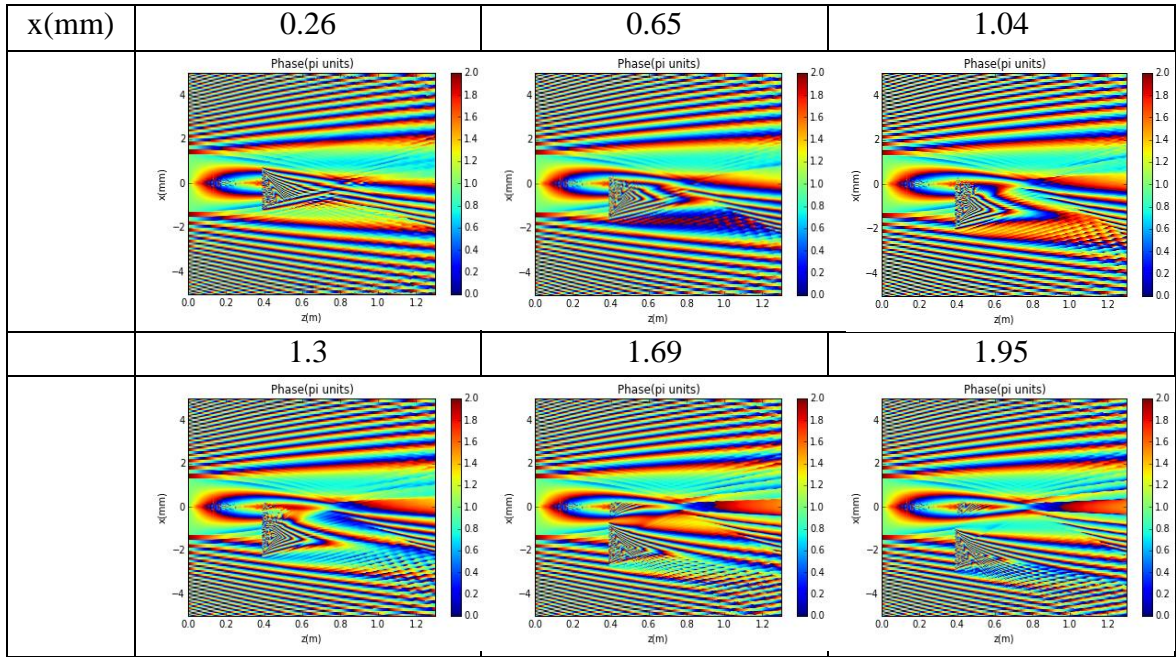


Figure 4.40: Phase profile for an Airy Ring beam with $r_0=1\text{mm}$, $w_0=0.13\text{mm}$ and $a=0.1$ which propagates in the presence of a circular block with different position x in x direction in every case ($x=0.26\text{mm}$, 0.65mm , 1.04mm , 1.3mm , 1.69mm , 1.95mm).

Figure 4.40 depicts phase profile of the propagated Airy Ring beam for different values of position of the circular block in x direction (x). It is shown that for lower values of x , the beam scatters and deforms, whereas for higher values of x it focuses. We observe at the Figure how the beam phase changes as the obstacle moves in x direction. As we can observe from the colorbars the presence of a circular block does not change much the Airy Ring beam phase. We can observe also the presence of artifacts.

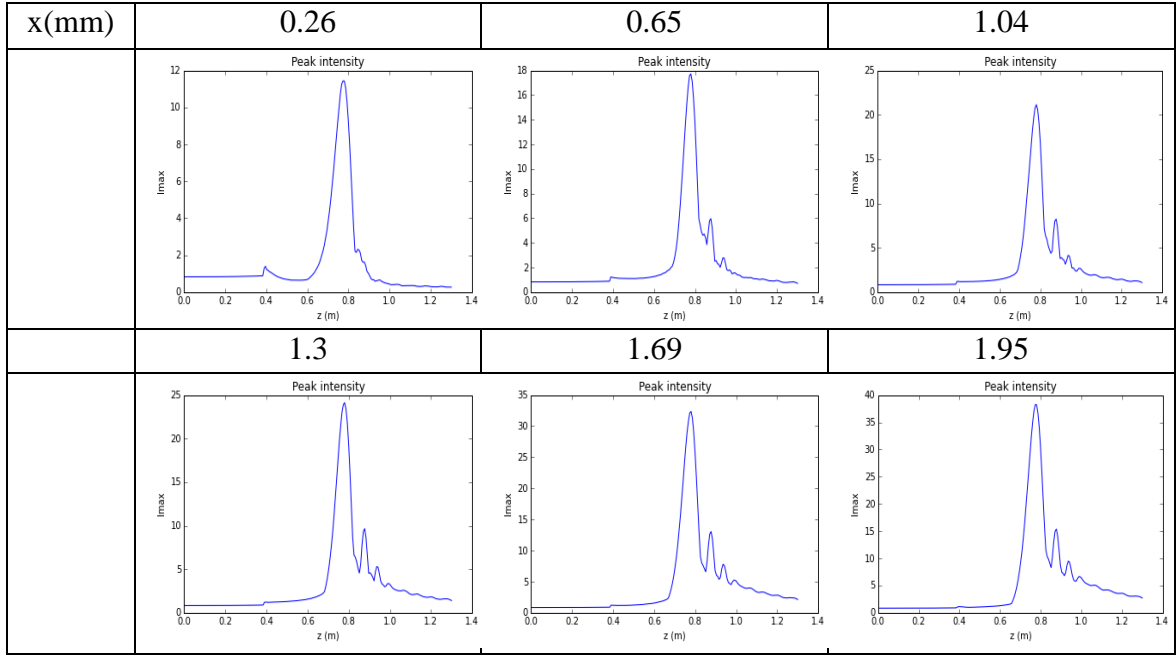


Figure 4.41: Maximum intensity profile for an Airy Ring beam with $r_0=1\text{mm}$, $w_0=0.13\text{mm}$ and $a=0.1$ which propagates in the presence of a circular block with different position x in x direction in every case ($x=0.26\text{mm}$, 0.65mm , 1.04mm , 1.3mm , 1.69mm , 1.95mm).

Figure 4.41 depicts maximum intensity profile of the propagated Airy Ring beam for different values of position in x direction of the circular block (x). It is shown that for lower values of x , the numerical and the theoretical maximum intensity profile have large discrepancy. For higher values of the obstacle position in x direction (x), the discrepancy between the numerical and the theoretical maximum intensity profile is smaller. For low values of the position in x direction of the circular block ($x=0.26\text{mm}$, 0.65mm), the intensity at the focus point of the beam has low value because the obstacle cuts enough energy which does not reach at the focus point of the beam. That is the reason that we observe a small peak intensity at $z=0.39\text{m}$ point for low values of the obstacle position in x direction. For higher values of the obstacle position in x direction ($x>1.3\text{mm}$) we observe that the circular block does not cut enough energy which reaches at the focus point of the beam. As the obstacle position in x direction increases, the intensity at the focus point of the beam also increases.

In Figure 4.42, we compare the percentage change of focus contrast data results (ΔI (%)), as it is defined in Equation (4.1), from Airy Ring and Gaussian simulations as a function of x position of the obstacle (x), which is normalized over the ring radius of the Airy Ring beam (r_0+w_0).

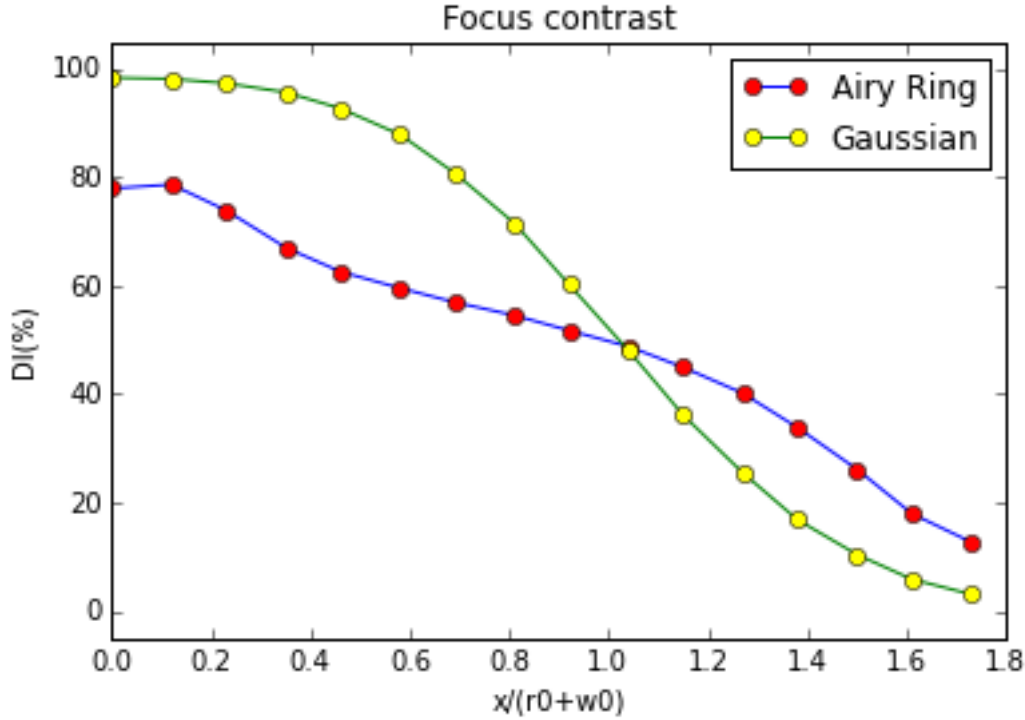


Figure 4.42: Comparison of the percentage change of focus contrast data results (ΔI (%)) from Airy Ring and Gaussian simulations as a function of x position of the obstacle (x), which is normalized over the ring radius of the Airy Ring beam (r_0+w_0).

In Figure 4.42, at lower values of the normalized obstacle position in x direction (x), Gaussian beams exhibit considerably higher percentage change of focus contrast data results (ΔI (%)), compared to the Airy Ring beams and so the losses in Gaussians beams are higher than the losses in Airy Ring beams. Interestingly, at higher values of the normalized obstacle position in x direction (x), Airy Ring beams exhibit considerably higher percentage change of focus contrast data results, compared to the Gaussian beams and so the losses in Airy Ring beams are higher than the losses in Gaussian beams. As a result, for low values of the obstacle position in x direction the Airy Ring beam is better than the Gaussian beam but for high values of the obstacle position in x direction the Gaussian beam is better than the Airy Ring beam. So for low values of obstacle position in x direction we prefer to use Airy Ring beam but for high values of obstacle position in x direction we prefer to use Gaussian beam.

Finally, in Figure 4.43, we compare the percentage change of focus position data results (ΔP (%)), as it is defined in Equation (4.2), from Airy Ring and Gaussian simulations as a function of x position of the obstacle (x), which is normalized over the ring radius of the Airy Ring beam (r_0+w_0).

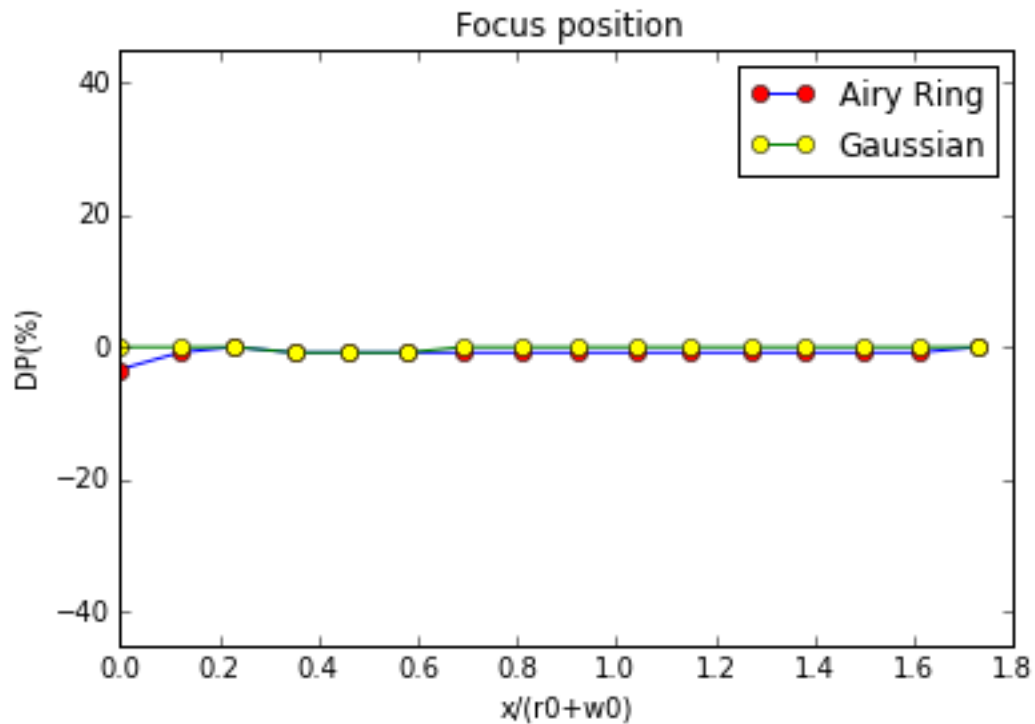


Figure 4.43: Comparison of the percentage change of focus position data results (ΔP (%)) from Airy Ring and Gaussian simulations as a function of x position of the obstacle (x), which is normalized over the ring radius of the Airy Ring beam (r_0+w_0).

In Figure 4.43 the percentage change of focus position data results ($\Delta P(\%)$) from Airy Ring and Gaussian simulations have around the same values for all the values of the normalized obstacle position in x direction (x). The focus position of the beams drops to P_{ref} for all the values of the normalized obstacle position in x direction (x). In this case it seems to be no focus shift (because the Airy Ring has a hole in the center of it).

4.4 Perfectly refracting propagation of a Ring-Airy beam in the presence of a circular glass

a. Variable size

π phase jump

We consider an Airy Ring beam with radius $r_0=1\text{mm}$ and the corresponding constants are $w_0=0.13\text{mm}$ and $a=0.1$, where $\lambda=0.8\mu\text{m}$. The propagation distance z is 1.3m . In the following simulations the transverse coordinates (x,y) are discretized to 1024×1024 sampling points while 200 steps are used for the propagation along z direction. We put an obstacle (circular glass) at the center $(x=0, y=0)$ of x,y directions and at the middle between $z=0$ and the focus point of the Ring-Airy beam. The thickness of the glass is equal to $\lambda/2$ and its refractive index is equal to 1.0. This glass adds π phase. At following graphs, we present the results of numerical simulation of the propagation of the Ring-Airy beam in the cases which the obstacle width D is different for every case. ($D= 2*r_0/3, r_0, 2*r_0, 2*(r_0+3w_0), 2*(r_0+7w_0), 2*(r_0+10w_0)$).

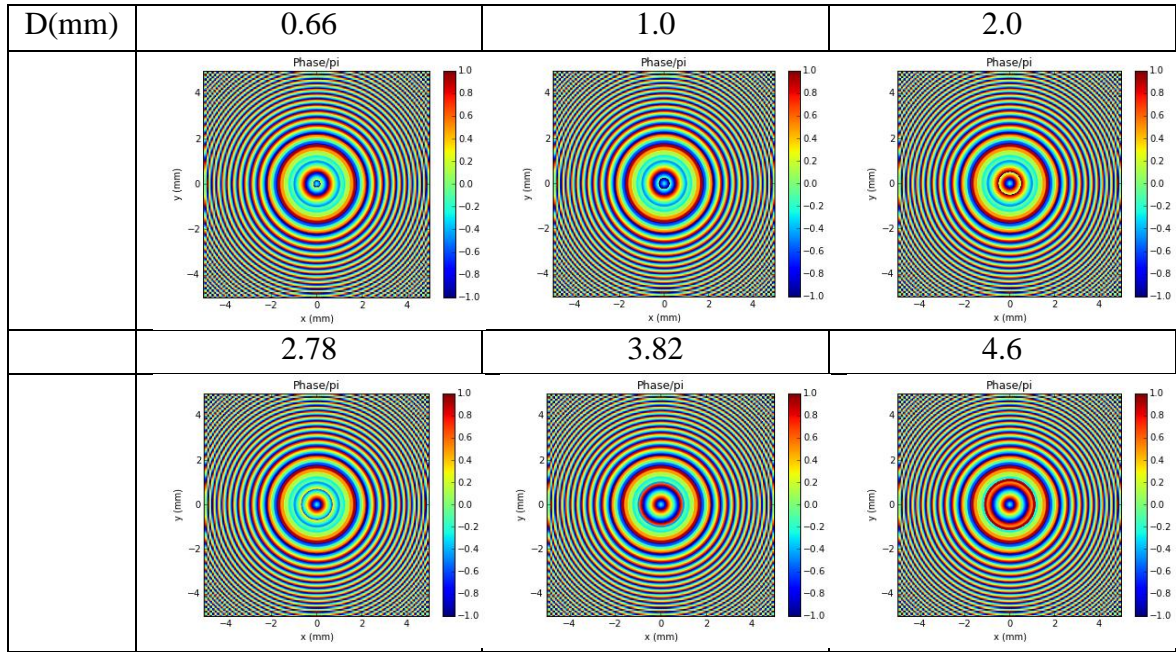


Figure 4.44: Beam phase after the circular glass for an Airy Ring beam with $r_0=1\text{mm}$, $w_0=0.13\text{mm}$ and $a=0.1$ which propagates in the presence of a circular glass for the case of π phase jump with different size in every case ($D= 2*r_0/3, r_0, 2*r_0, 2*(r_0+3w_0), 2*(r_0+7w_0), 2*(r_0+10w_0)$).

Figure 4.44 depicts beam phase after the circular glass for an Airy Ring beam for the case of π phase jump. When the obstacle width is equal to $D=0.66\text{mm}$, we observe that the phase in the center of the beam has a low value in pi units. Interestingly, when the obstacle width is equal to $D=2.0\text{mm}$, the phase in the center of the beam has higher value in pi units than the previous one. For higher values of the obstacle width ($D>2.0\text{mm}$), we observe that as the glass obstacle is increased in size, a secondary phase peak appears. This peak is due to the diffraction from the transparent obstacle and at some point becomes stronger than the primary phase peak. In all the cases we observe some artifacts at the edges of the square.

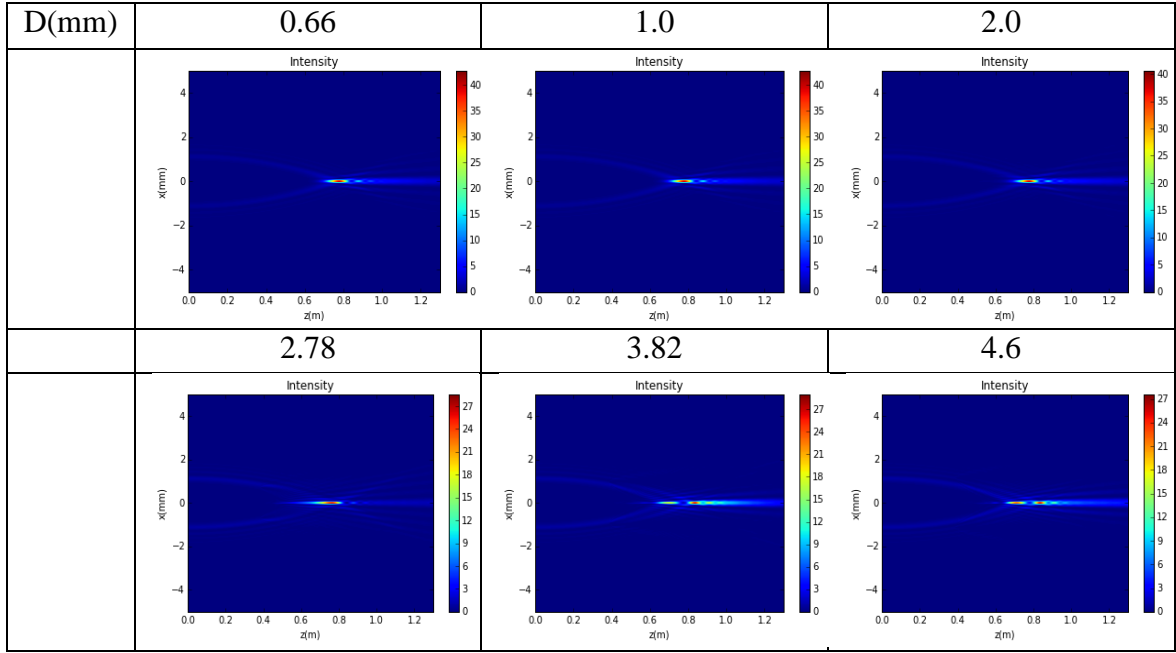


Figure 4.45: Intensity profile for an Airy Ring beam with $r_0=1\text{mm}$, $w_0=0.13\text{mm}$ and $a=0.1$ which propagates in the presence of a circular glass for the case of π phase jump with different size in every case ($D= 2*r_0/3, r_0, 2*r_0, 2*(r_0+3w_0), 2*(r_0+7w_0), 2*(r_0+10w_0)$).

In Figure 4.45 we observe that as the glass obstacle is increased in size, a secondary peak appears. This peak is due to the diffraction from the transparent obstacle and at some point becomes stronger than the primary peak. We observe also that for low values of the obstacle width (D), the intensity value at the focus point of the beam is high. This happens because the Airy Ring beam has a hole in the center of it and when the obstacle width value is low, the obstacle does not cut enough energy and so much energy reaches at the focus point of the beam. On the other hand, we observe low values of intensity for high values of the obstacle width. This happens because when the obstacle width value is high, the obstacle cuts enough energy which does not reach at the focus point of the beam.

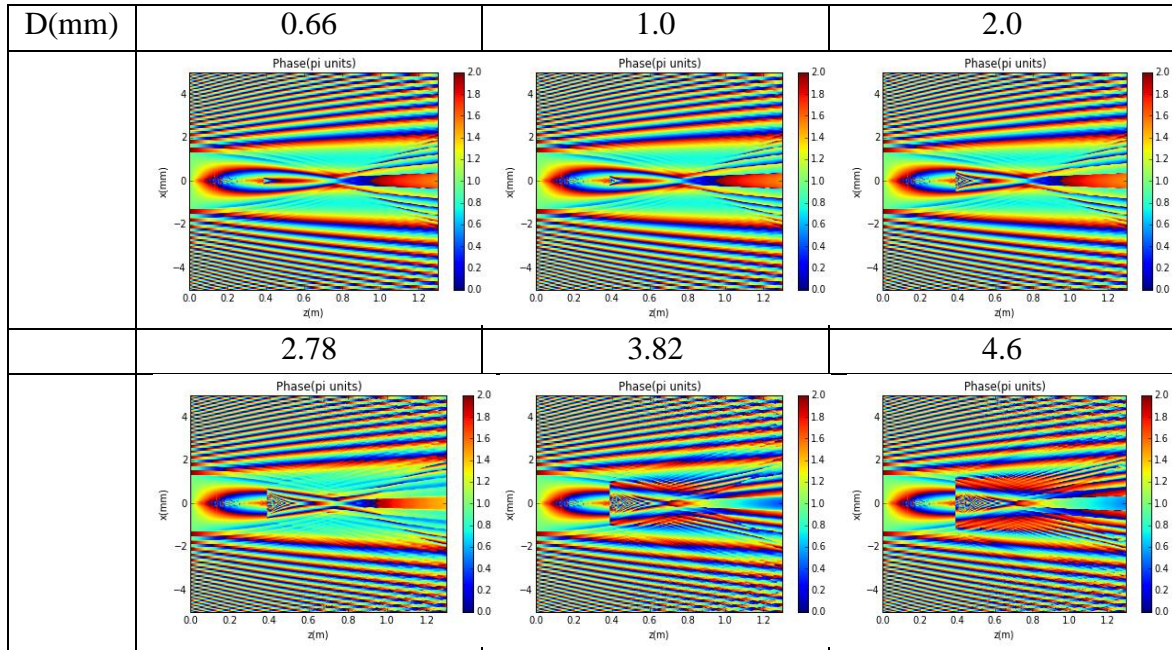


Figure 4.46: Phase profile for an Airy Ring beam with $r_0=1\text{mm}$, $w_0=0.13\text{mm}$ and $a=0.1$ which propagates in the presence of a circular glass for the case of π phase jump with different size in every case ($D= 2*r_0/3, r_0, 2*r_0, 2*(r_0+3w_0), 2*(r_0+7w_0), 2*(r_0+10w_0)$).

Figure 4.46 depicts phase profile of the propagated Airy Ring beam for different values of the circular glass width (D) for the case of π phase jump. We observe at the Figure how the beam phase changes as the obstacle width increases. The phase change is higher at the middle between $z=0$ and the focus point of the Ring-Airy beam point where the glass obstacle is situated. For this case the phase jump at the point where the obstacle is situated is equal to π . As we can observe from the colorbars, the presence of a circular glass does not change much the Airy Ring beam phase. We can observe also the presence of artifacts.

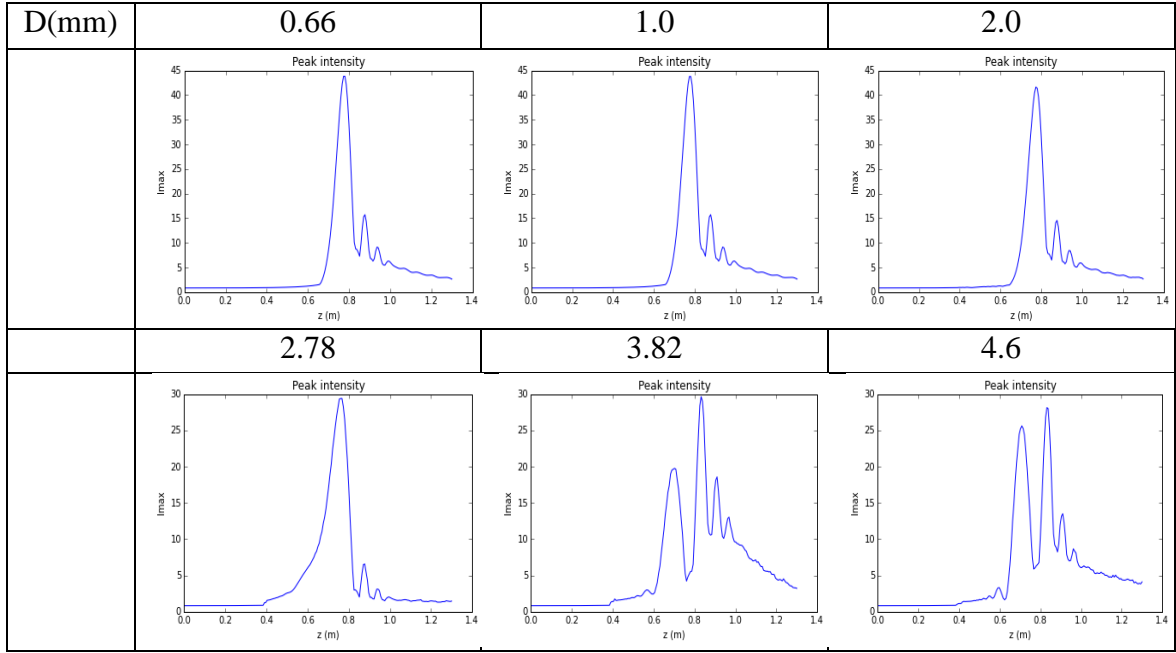


Figure 4.47: Maximum intensity profile for an Airy Ring beam with $r_0=1\text{mm}$, $w_0=0.13\text{mm}$ and $a=0.1$ which propagates in the presence of a circular glass for the case of π phase jump with different size in every case ($D= 2*r_0/3, r_0, 2*r_0, 2*(r_0+3w_0), 2*(r_0+7w_0), 2*(r_0+10w_0)$).

Figure 4.47 depicts maximum intensity profile of the propagated Airy Ring beam for different values of size of the circular glass (D) for the case of π phase jump. It is shown that for lower values of D , the numerical and the theoretical maximum intensity profile have small discrepancy. For higher values of the obstacle width D , the discrepancy between the numerical and the theoretical maximum intensity profile is larger. For the case which the obstacle width is equal to $D=0.66\text{mm}$, we observe a high value of intensity at the focus point of the beam. For $D=1.0\text{mm}$, the intensity at the focus point of the beam remains at the same value as previous. For low values of the obstacle width, the intensity at the focus point of the beam has a high value because the Airy Ring beam has a hole in the center and the obstacle which has a low value of width does not cut energy at the point which is situated. So, all the energy reaches at the focus point of the beam and at this point the intensity value is high. For higher values of the obstacle width ($D>2.78\text{mm}$) we observe that a secondary intensity peak appears. This intensity peak is due to the diffraction from the transparent obstacle and becomes stronger than the primary intensity peak. We observe also that the intensity at the focus point of the beam has lower value than in the cases where the obstacle width has a low value. This happens because the width

value of the obstacle is high and it cuts much energy which does not reach at the focus point of the beam.

In Figure 4.48, we compare the percentage change of focus contrast data results (ΔI (%)), as it is defined in Equation (4.1), from Airy Ring and Gaussian simulations for the case of π phase jump as a function of the obstacle width (D), which is normalized over the ring radius of the Airy Ring beam (r_0+w_0).

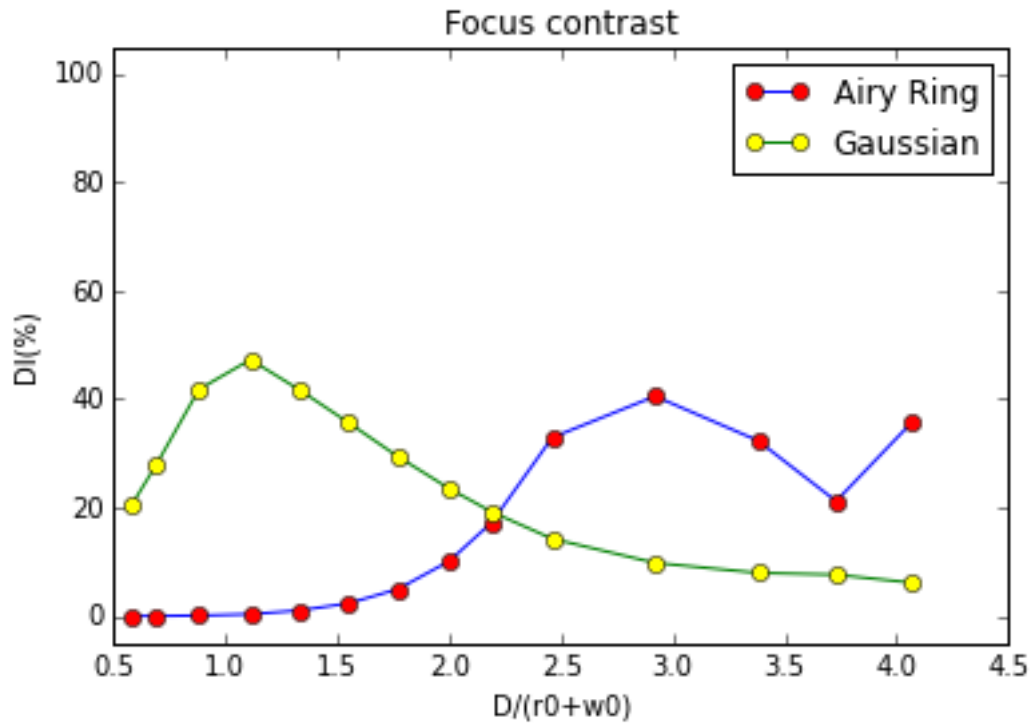


Figure 4.48: Comparison of the percentage change of focus contrast data results (ΔI (%)) from Airy Ring and Gaussian simulations for the case of π phase jump as a function of the obstacle width (D), which is normalized over the ring radius of the Airy Ring beam (r_0+w_0).

In Figure 4.48, at lower values of the normalized obstacle width (D), Gaussian beams exhibit considerably higher percentage change of focus contrast data results (ΔI (%)), compared to the Airy Ring beams and so the losses in Gaussians beams are higher than the losses in Airy Ring beams. Interestingly, at higher values of the normalized obstacle width (D), Airy Ring beams exhibit considerably higher percentage change of focus contrast data results, compared to the Gaussian beams and so the losses in Airy Ring beams are higher than the losses in Gaussian beams. As a result, for low values of the obstacle width, the Airy Ring beam is better than the Gaussian beam but for high values of the obstacle width, the Gaussian beam is better

than the Airy Ring beam. So for low values of obstacle width we prefer to use Airy Ring beam but for high values of obstacle width we prefer to use Gaussian beam.

Finally, in Figure 4.49, we compare the percentage change of focus position data results (ΔP (%)), as it is defined in Equation (4.2), from Airy Ring and Gaussian simulations for the case of π phase jump as a function of the obstacle width (D), which is normalized over the ring radius of the Airy Ring beam (r_0+w_0).

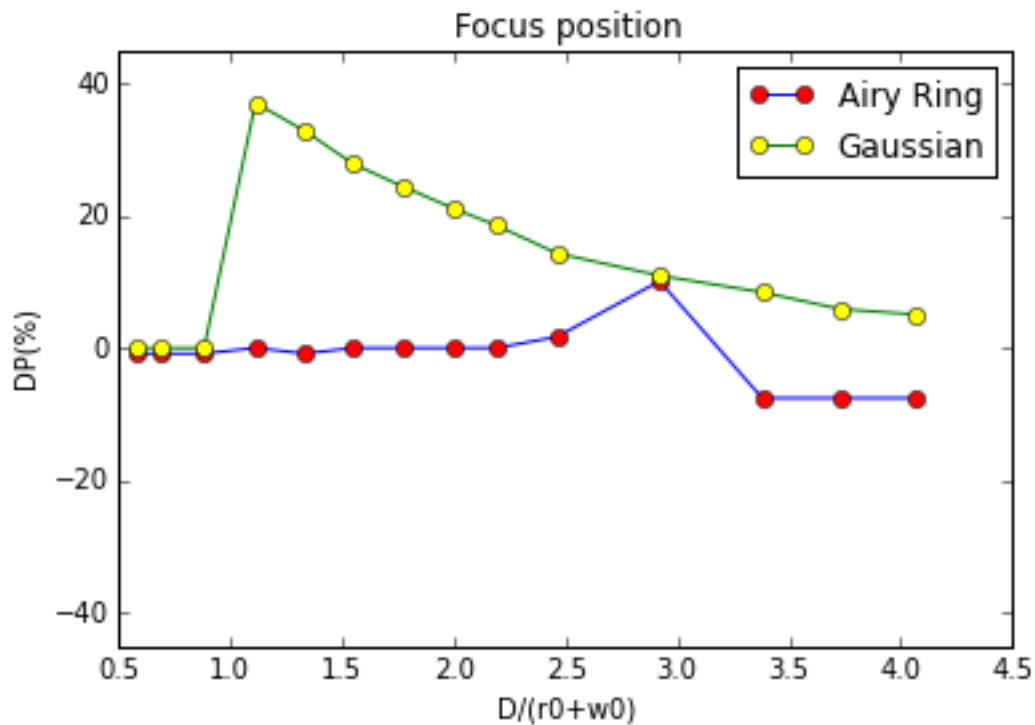


Figure 4.49: Comparison of the percentage change of focus position data results (ΔP (%)) from Airy Ring and Gaussian simulations for the case of π phase jump as a function of the obstacle width (D), which is normalized over the ring radius of the Airy Ring beam (r_0+w_0).

In Figure 4.49, for most of the values of the normalized obstacle width (D), Airy Ring beams exhibit considerably lower percentage change of focus position data results, compared to the Gaussian beams. For lower values of the normalized obstacle width (D), we observe a strong shift of the focus of the Gaussian beam. On the other hand for higher values of the normalized obstacle width (D), we observe a strong shift of the focus of the Airy Ring beam. We observe these strong shifts of the focus of the beams because as the beams pass through the glass obstacle, the diffraction phenomenon happens which moves the focus points of the beams.

$\pi/2$ phase jump

Next, we follow the same steps as previous with the same Airy-Ring beam ($r_0=1\text{mm}$, $w_0=0.13\text{mm}$, $a=0.1$) but with a different circular glass. In this case the thickness of the glass is equal to $\lambda/4$ and its refractive index is equal to 1.0. This glass adds $\pi/2$ phase. In the following simulations the transverse coordinates (x,y) are discretized to 1024×1024 sampling points while 200 steps are used for the propagation along z direction. At following graphs, we present the results of numerical simulation of the propagation of the Ring-Airy beam in the cases which the obstacle width is different for every case. ($D= 2*(r_0+2w_0)$, $2*(r_0+4w_0)$, $2*(r_0+5w_0)$, $2*(r_0+8w_0)$, $2*(r_0+9w_0)$, $2*(r_0+10w_0)$).

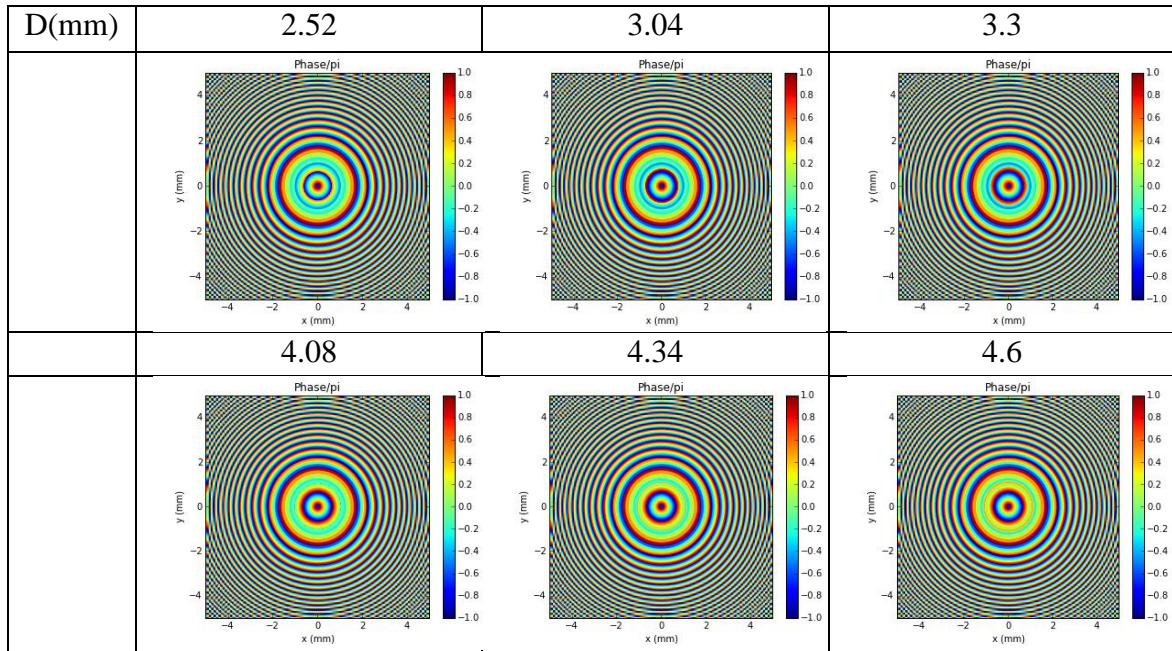


Figure 4.50: Beam phase after the circular glass for an Airy Ring beam with $r_0=1\text{mm}$, $w_0=0.13\text{mm}$ and $a=0.1$ which propagates in the presence of a circular glass for the case of $\pi/2$ phase jump with different size in every case ($D= 2*(r_0+2w_0)$, $2*(r_0+4w_0)$, $2*(r_0+5w_0)$, $2*(r_0+8w_0)$, $2*(r_0+9w_0)$, $2*(r_0+10w_0)$).

Figure 4.50 depicts beam phase after the circular glass for an Airy Ring beam for the case of $\pi/2$ phase jump. When the obstacle width is equal to $D=2.52\text{mm}$, we observe that the phase in the center of the beam has a low value in pi units. Interestingly, when the obstacle width is equal to $D=3.3\text{mm}$, the phase in the center of the beam has higher value in pi units than the previous one. For higher values of the

obstacle width ($D > 3.3\text{mm}$), we observe that as the glass obstacle is increased in size, a secondary phase peak appears. This peak is due to the diffraction from the transparent obstacle and at some point becomes stronger than the primary phase peak. In all the cases we observe some artifacts at the edges of the square.

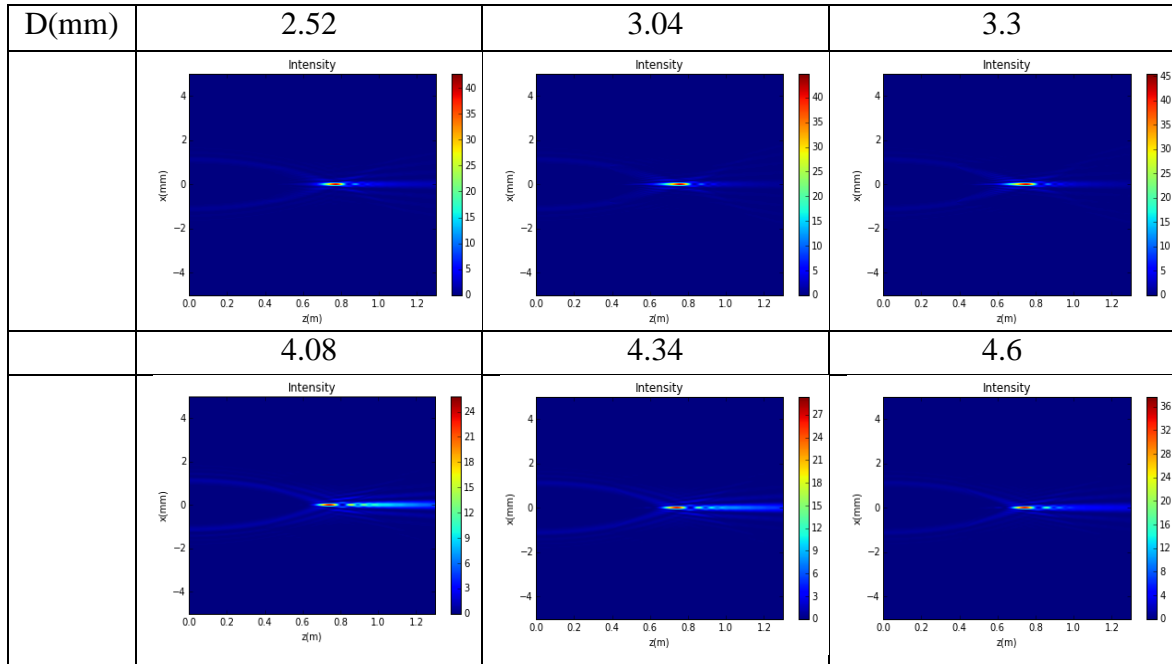


Figure 4.51: Intensity profile for an Airy Ring beam with $r_0=1\text{mm}$, $w_0=0.13\text{mm}$ and $a=0.1$ which propagates in the presence of a circular glass for the case of $\pi/2$ phase jump with different size in every case ($D= 2*(r_0+2w_0)$, $2*(r_0+4w_0)$, $2*(r_0+5w_0)$, $2*(r_0+8w_0)$, $2*(r_0+9w_0)$, $2*(r_0+10w_0)$).

In Figure 4.51 we observe that as the glass obstacle is increased in size, a secondary peak appears. This peak is due to the diffraction from the transparent obstacle but it does not become stronger than the primary intensity peak as in the case where the glass obstacle adds π phase jump. We observe also that for low values of the obstacle width (D), the intensity value at the focus point of the beam is high. This happens because the Airy Ring beam has a hole in the center of it and when the obstacle width value is low, the obstacle does not cut enough energy and so much energy reaches at the focus point of the beam. On the other hand, we observe low values of intensity for high values of the obstacle width. This happens because when the obstacle width value is high, the obstacle cuts enough energy which does not reach at the focus point of the beam.

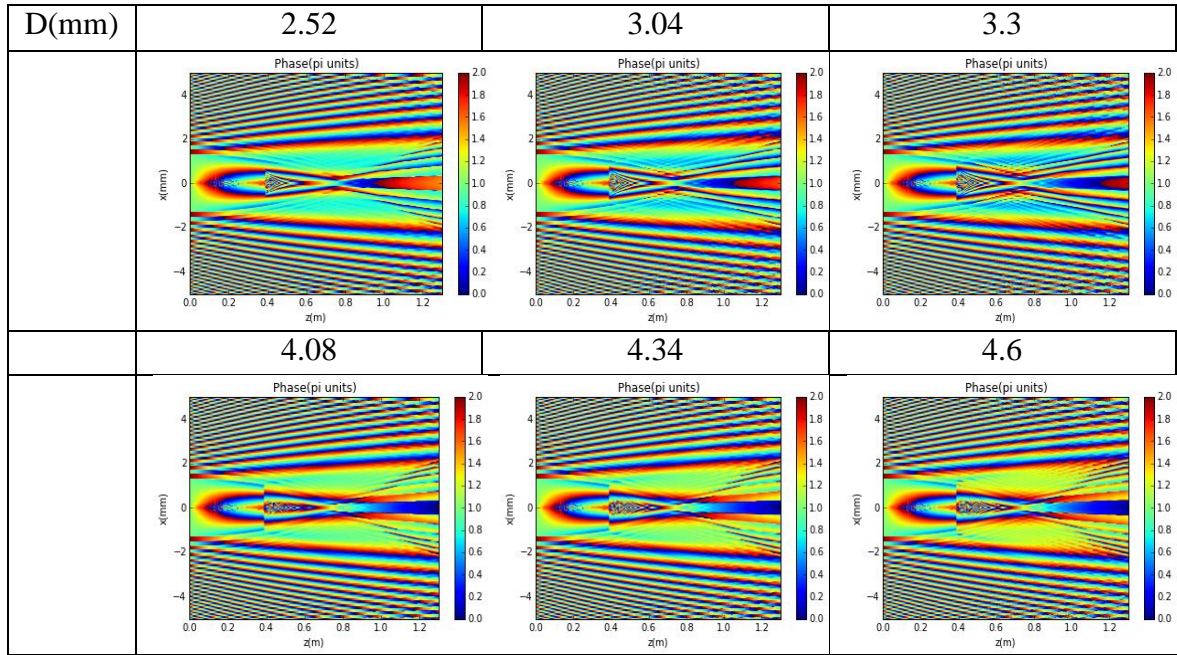


Figure 4.52: Phase profile for an Airy Ring beam with $r_0=1\text{mm}$, $w_0=0.13\text{mm}$ and $a=0.1$ which propagates in the presence of a circular glass for the case of $\pi/2$ phase jump with different size in every case ($D= 2*(r_0+2w_0)$, $2*(r_0+4w_0)$, $2*(r_0+5w_0)$, $2*(r_0+8w_0)$, $2*(r_0+9w_0)$, $2*(r_0+10w_0)$).

Figure 4.52 depicts phase profile of the propagated Airy Ring beam for different values of the circular glass width (D) for the case of $\pi/2$ phase jump. We observe at the Figure how the beam phase changes as the obstacle width increases. The phase change is higher at the middle between $z=0$ and the focus point of the Ring-Airy beam point where the glass obstacle is situated. For this case the phase jump at the point where the obstacle is situated is equal to $\pi/2$. As we can observe from the colorbars, the presence of a circular glass does not change much the Airy Ring beam phase. We can observe also the presence of artifacts.

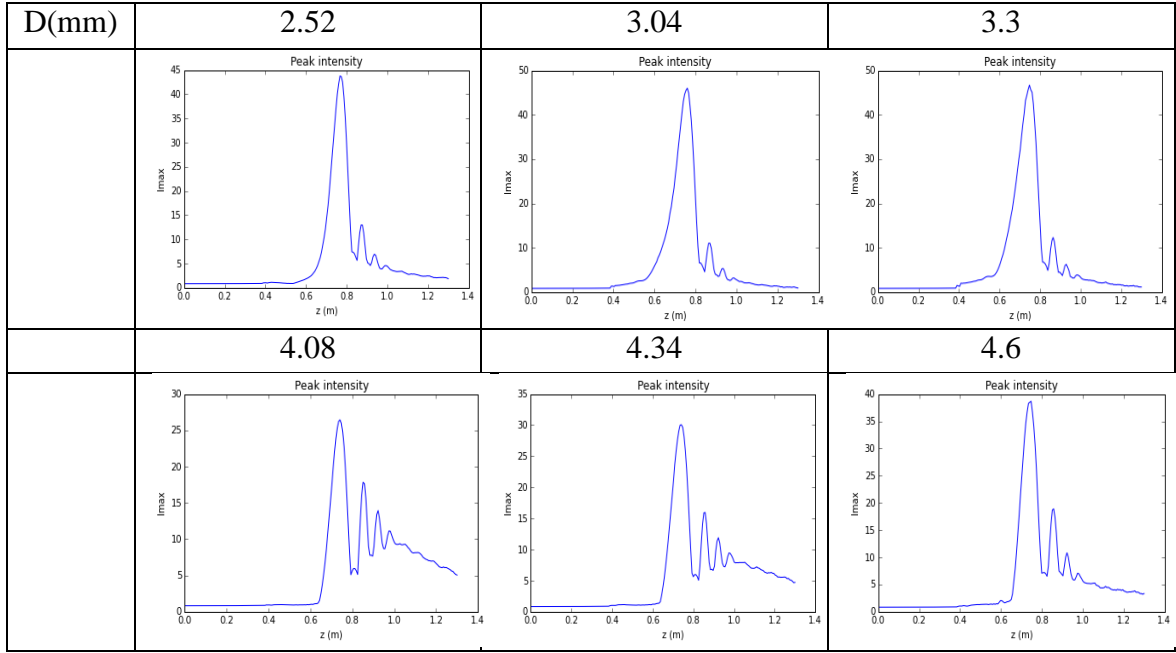


Figure 4.53: Maximum intensity profile for an Airy Ring beam with $r_0=1\text{mm}$, $w_0=0.13\text{mm}$ and $a=0.1$ which propagates in the presence of a circular glass for the case of $\pi/2$ phase jump with different size in every case ($D= 2*(r_0+2w_0)$, $2*(r_0+4w_0)$, $2*(r_0+5w_0)$, $2*(r_0+8w_0)$, $2*(r_0+9w_0)$, $2*(r_0+10w_0)$).

Figure 4.53 depicts maximum intensity profile of the propagated Airy Ring beam for different values of size of the circular glass (D) for the case of $\pi/2$ phase jump. It is shown that for lower values of D , the numerical and the theoretical maximum intensity profile have small discrepancy. For higher values of the obstacle width D , the discrepancy between the numerical and the theoretical maximum intensity profile is larger. For low values of the obstacle width ($D < 4.08\text{mm}$), we observe that the intensity at the focus point of the beam is increased as the obstacle width is increased. We observe also that for low values of the obstacle width, the intensity at the focus point of the beam has a high value because the Airy Ring beam has a hole in the center and the obstacle which has a low value of width does not cut energy at the point which is situated. So, all the energy reaches at the focus point of the beam and at this point the intensity value is high. For high values of the obstacle width ($D > 3.3\text{mm}$), the intensity at the focus point of the beam has lower value than in the previous cases. This happens because the width value of the obstacle is high and it cuts much energy which does not reach at the focus point of the beam. We observe also that a secondary intensity peak appears. This intensity peak is due to the

diffraction from the transparent obstacle but it does not become stronger than the primary intensity peak as in the case where the glass obstacle adds π phase jump.

In Figure 4.54, we compare the percentage change of focus contrast data results (ΔI (%)), as it is defined in Equation (4.1), from Airy Ring and Gaussian simulations for the case of $\pi/2$ phase jump as a function of the obstacle width (D), which is normalized over the ring radius of the Airy Ring beam (r_0+w_0).

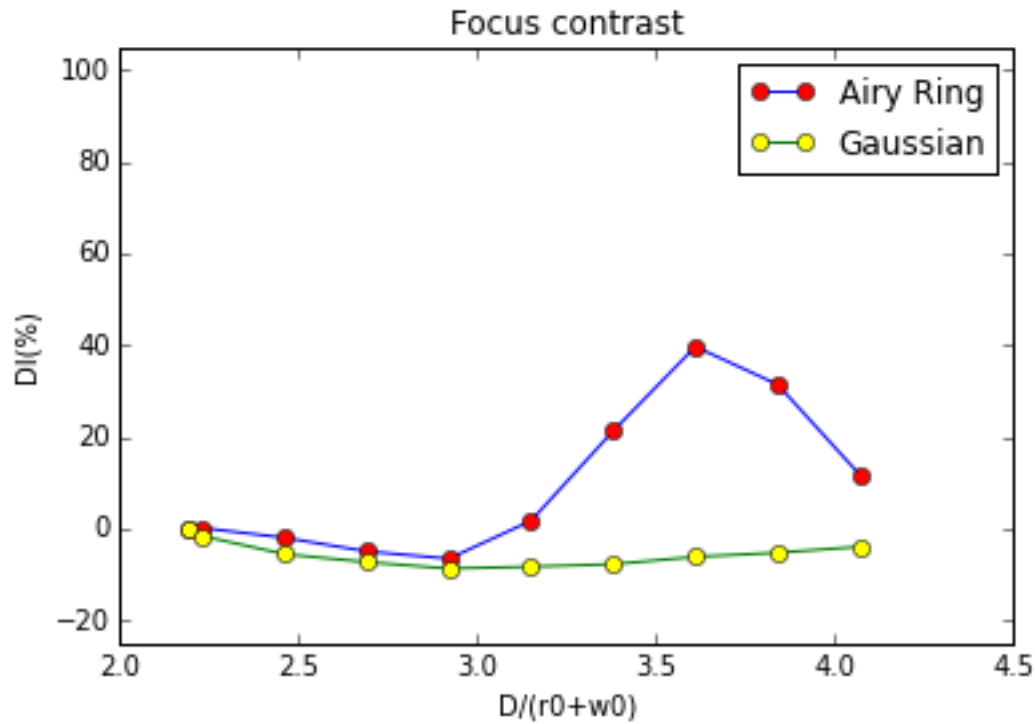


Figure 4.54 Comparison of the percentage change of focus contrast data results (ΔI (%)) from Airy Ring and Gaussian simulations for the case of $\pi/2$ phase jump as a function of the obstacle width (D), which is normalized over the ring radius of the Airy Ring beam (r_0+w_0).

In Figure 4.54 the percentage change of focus contrast data results (ΔI (%)) from Airy Ring and Gaussian simulations have around the same values for lower values of the normalized obstacle width (D) and so the same losses. Interestingly, at higher values of the normalized obstacle width (D), Gaussian beams exhibit considerably lower percentage change of focus contrast data results, compared to the Airy Ring beams and so lower losses. As a result, Gaussian beam is better in this case because it has the same losses as Airy Ring beam for low values of the normalized obstacle width (D) but lower losses than Airy Ring beam for high values of the normalized obstacle width (D).

Finally, in Figure 4.55, we compare the percentage change of focus position data results (ΔP (%)), as it is defined in Equation (4.2), from Airy Ring and Gaussian simulations for the case of $\pi/2$ phase jump as a function of the obstacle width (D), which is normalized over the ring radius of the Airy Ring beam (r_0+w_0).

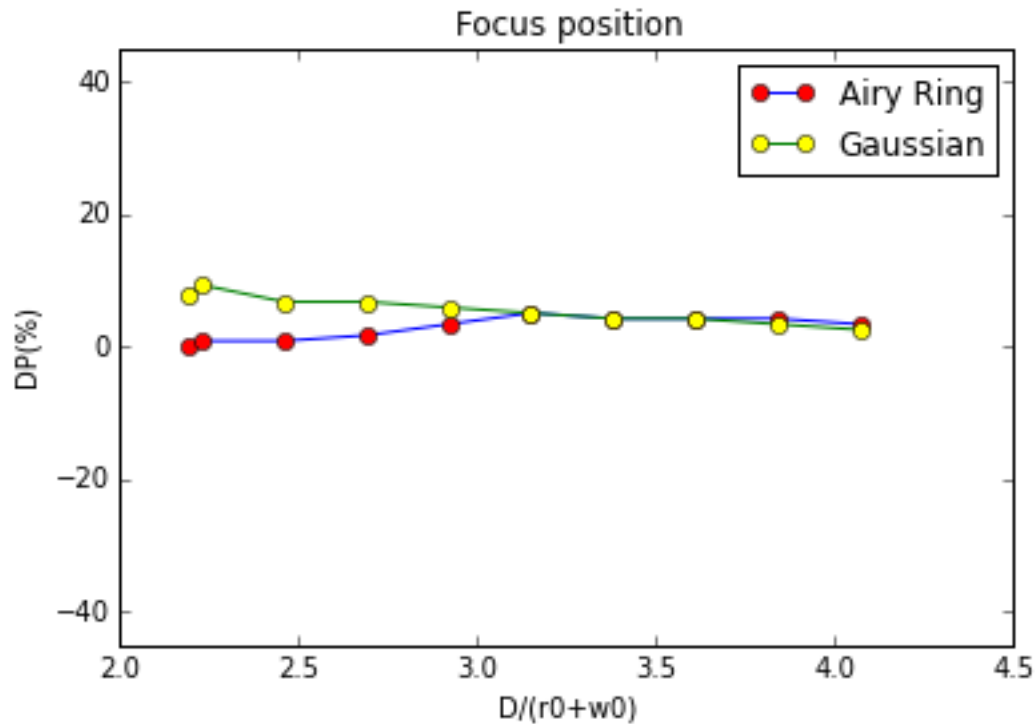


Figure 4.55: Comparison of the percentage change of focus position data results (ΔP (%)) from Airy Ring and Gaussian simulations for the case of $\pi/2$ phase jump as a function of the obstacle width (D), which is normalized over the ring radius of the Airy Ring beam (r_0+w_0).

In Figure 4.55, at lower values of the normalized obstacle width (D), Airy Ring beams exhibit considerably lower percentage change of focus position data results, compared to the Gaussian beams. At higher values of the normalized obstacle width (D), Airy Ring and Gaussian beams have around the same values of percentage change of focus position data results.

b. Variable longitudinal position

π phase jump

We consider an Airy Ring beam with radius $r_0=1\text{mm}$ and the corresponding constants are $w_0=0.13\text{mm}$ and $\alpha=0.1$, where $\lambda=0.8\ \mu\text{m}$. The propagation distance z is $1.3\ \text{m}$. In the following simulations the transverse coordinates (x,y) are discretized to 1024×1024 sampling points while 200 steps are used for the propagation along z direction. We put an obstacle (circular glass) at the center $(x=0,y=0)$ of x,y directions. The width of the glass is equal to $2 \cdot (r_0 + w_0)$, the thickness of the glass is equal to $\lambda/2$ and its refractive index is equal to 1.0. This glass adds π phase. At following graphs, we present the results of numerical simulation of the propagation of the Ring-Airy beam in the cases which the obstacle position in z direction is different for every case. The obstacle position varies from the point $z=0$ up to Ring-Airy focus point. ($z=100.0\text{mm}$, 200.0mm , 390.0mm , 500.0mm , 600.0mm , 700.0mm).

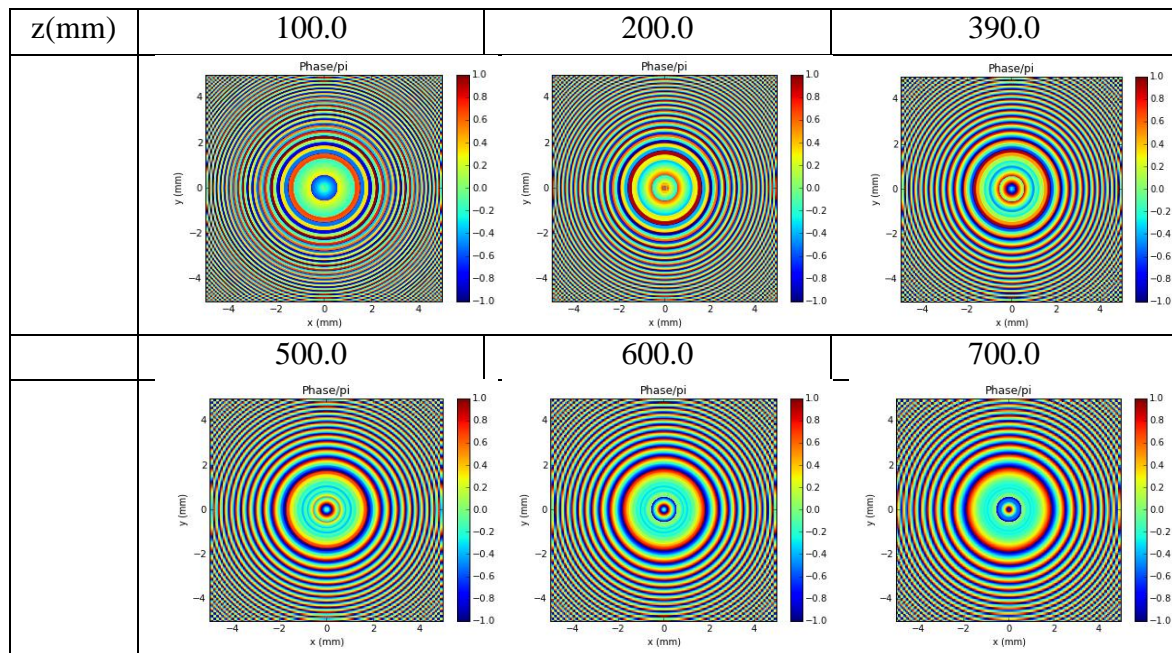


Figure 4.56: Beam phase after the circular glass for an Airy Ring beam with $r_0=1\text{mm}$, $w_0=0.13\text{mm}$ and $a=0.1$ which propagates in the presence of a circular glass for the case of π phase jump with different position z in z direction in every case ($z=100.0\text{mm}$, 200.0mm , 390.0mm , 500.0mm , 600.0mm , 700.0mm).

Figure 4.56 depicts beam phase after the circular glass for an Airy Ring beam. for the case of π phase jump. When the obstacle position in z direction is equal to $z=100.0\text{mm}$, we observe that the phase in the center of the beam has a low value in π units. Interestingly, when the obstacle position in z direction is equal to $z=390.0\text{mm}$, the phase in the center of the beam has higher value in π units than the previous one. For higher values of the obstacle position in z direction ($z>390.0\text{mm}$), we observe that as the value of the glass position in z direction is increased, a secondary phase peak appears. This peak is due to the diffraction from the transparent obstacle and at some point becomes stronger than the primary phase peak. In all the cases we observe some artifacts at the edges of the square.

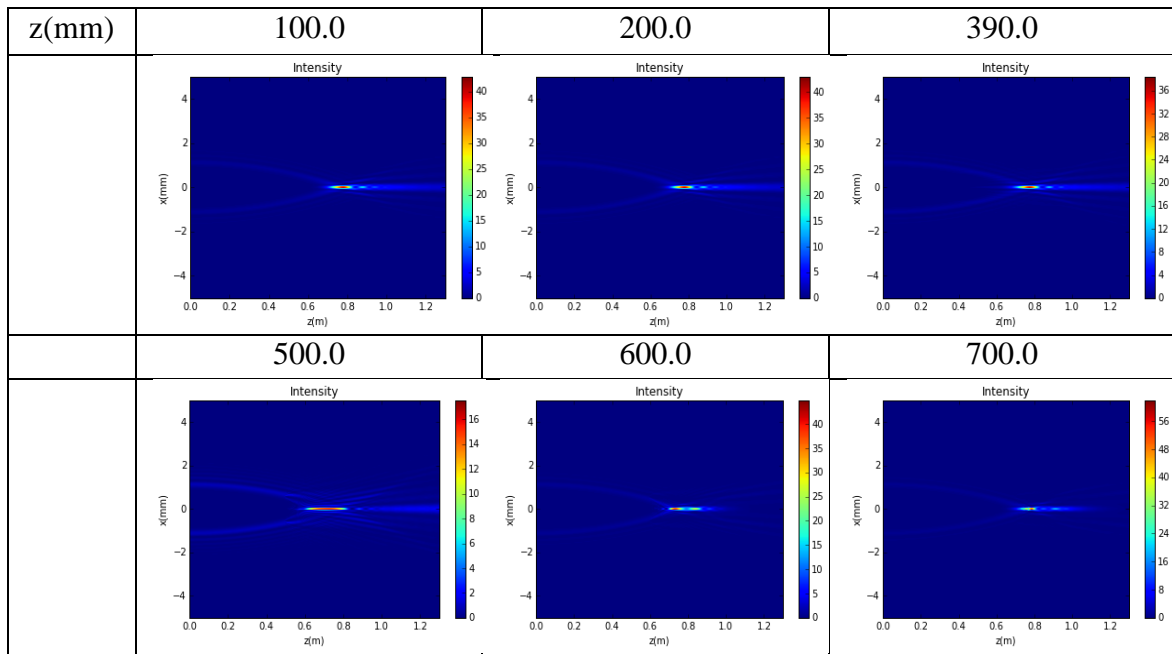


Figure 4.57: Intensity profile for an Airy Ring beam with $r_0=1\text{mm}$, $w_0=0.13\text{mm}$ and $a=0.1$ which propagates in the presence of a circular glass for the case of π phase jump with different position z in z direction in every case ($z=100.0\text{mm}$, 200.0mm , 390.0mm , 500.0mm , 600.0mm , 700.0mm).

In Figure 4.57 we observe that as the value of the glass obstacle position in z direction is increased, a secondary peak appears. This peak is due to the diffraction from the transparent obstacle but it does not become stronger than the primary intensity peak. We observe also that for low values of the obstacle position in z direction (z), the intensity value at the focus point of the beam is high. When the obstacle position in z direction has a value which is equal to $z=500.0\text{mm}$, we observe

that the beam scatters and deforms. For high values of the glass obstacle position in z direction ($z > 500.0\text{mm}$), we observe that the Airy Ring beam focuses and the intensity value at the focus point of the beam is high. We observe also that for high values of the glass obstacle position in z direction ($z > 500.0\text{mm}$), the focus point of the Airy Ring beam is moving. This is due to the diffraction from the transparent obstacle.

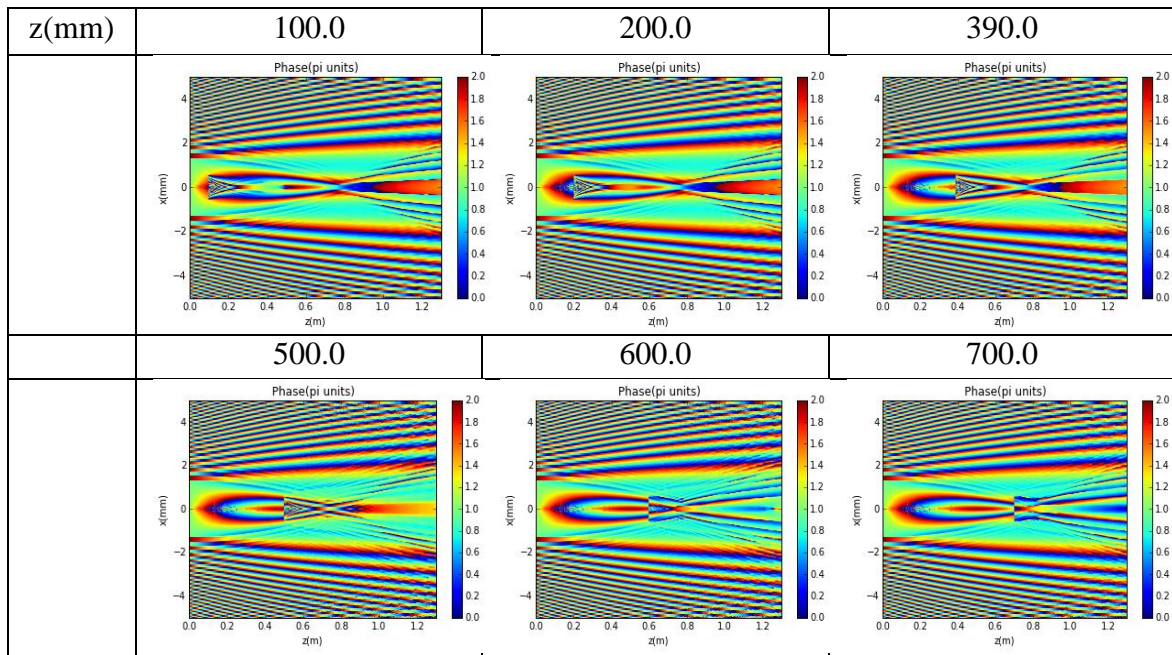


Figure 4.58: Phase profile for an Airy Ring beam with $r_0=1\text{mm}$, $w_0=0.13\text{mm}$ and $a=0.1$ which propagates in the presence of a circular glass for the case of π phase jump with different position z in z direction in every case ($z=100.0\text{mm}$, 200.0mm , 390.0mm , 500.0mm , 600.0mm , 700.0mm).

Figure 4.58 depicts phase profile of the propagated Airy Ring beam for different values of position in z direction of the circular glass (z) for the case of π phase jump. We observe at the Figure how the beam phase changes as the obstacle moves in z direction. The phase change is higher at the point where the glass obstacle is situated. For this case the phase jump at the point where the obstacle is situated is equal to π . As we can observe from the colorbars, the presence of a circular glass does not change much the Airy Ring beam phase. We can observe also the presence of artifacts.

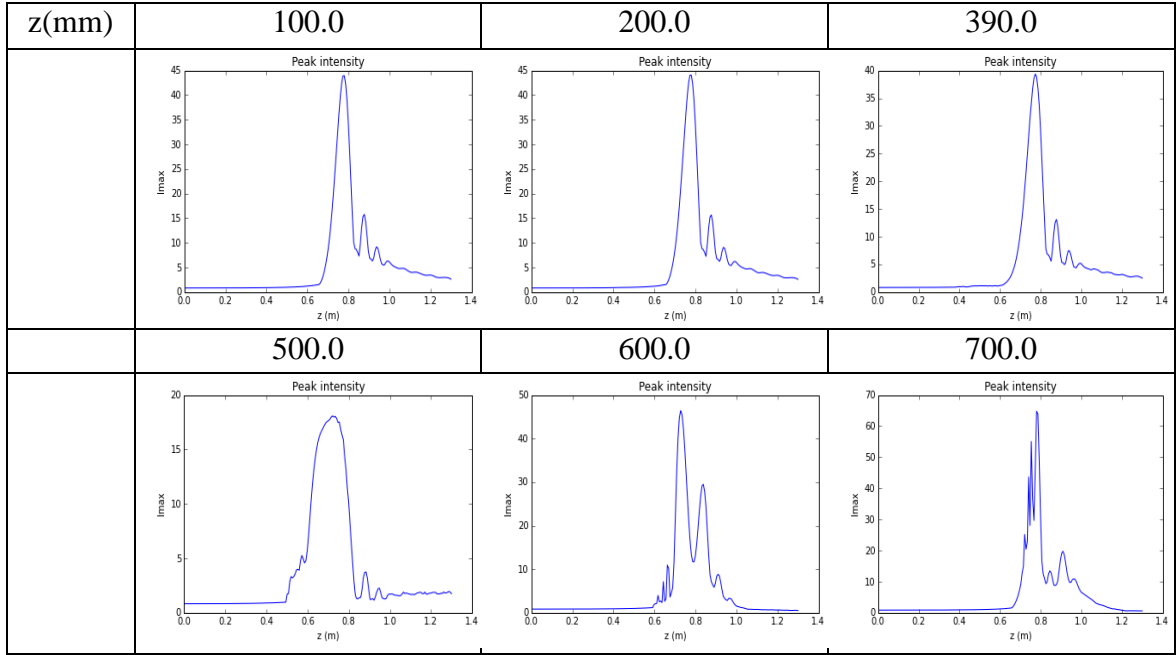


Figure 4.59: Maximum intensity profile for an Airy Ring beam with $r_0=1\text{mm}$, $w_0=0.13\text{mm}$ and $a=0.1$ which propagates in the presence of a circular glass for the case of π phase jump with different position z in z direction in every case ($z=100\text{ mm}$, 200 mm , 390 mm , 500 mm , 600mm , 700mm).

Figure 4.59 depicts maximum intensity profile of the propagated Airy Ring beam for different values of the circular glass position in z direction (z) for the case of π phase jump. It is shown that for lower values of z , the numerical and the theoretical maximum intensity profile have small discrepancy. For higher values of the obstacle position in z direction z , the discrepancy between the numerical and the theoretical maximum intensity profile is larger. For low values of the obstacle position in z direction ($z < 500.0\text{mm}$), we observe that the intensity at the focus point of the beam has a high value. For $z=500.0\text{mm}$, the intensity at the focus point of the beam has a low value. For high values of the obstacle position in z direction ($z > 500.0\text{mm}$), the intensity at the focus point of the beam has high value which is increased as the obstacle position in z direction increases. We observe also that a secondary intensity peak appears. This intensity peak is due to the diffraction from the transparent obstacle but it does not become stronger than the primary intensity peak.

In Figure 4.60, we compare the percentage change of focus contrast data results ($\Delta I (\%)$), as it is defined in Equation (4.1), from Airy Ring and Gaussian simulations for the case of π phase jump as a function of z position of the obstacle (z), which is

normalized over the Airy Ring focal distance (f_0)

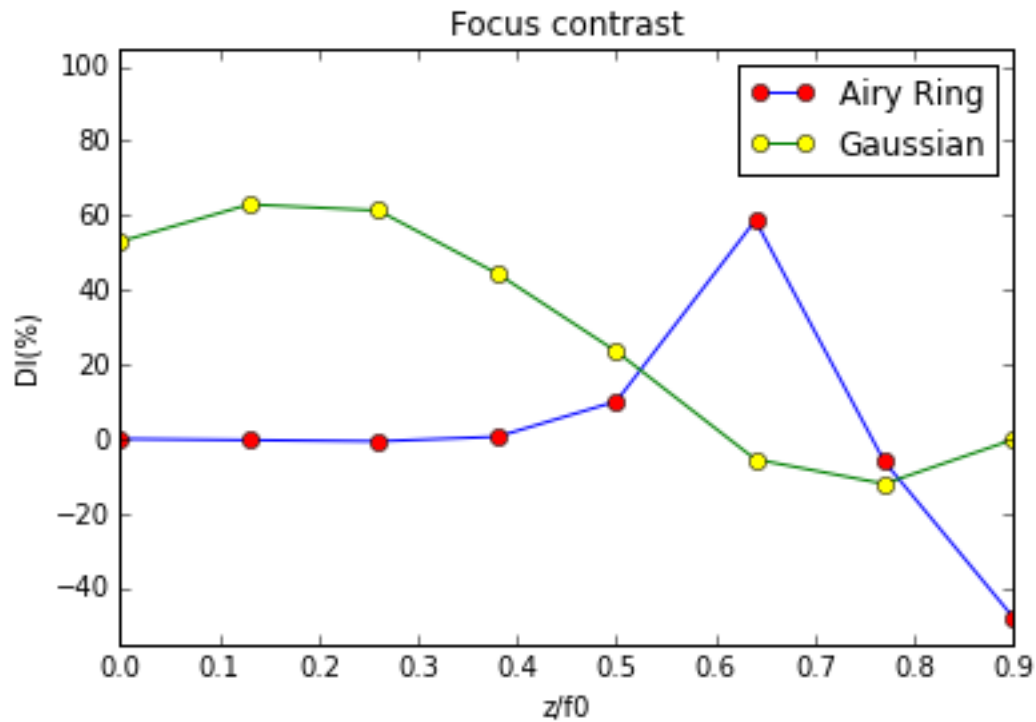


Figure 4.60: Comparison of the percentage change of focus contrast data results (ΔI (%)) from Airy Ring and Gaussian simulations for the case of π phase jump as a function of z position of the obstacle (z), which is normalized over the Airy Ring focal distance (f_0).

In Figure 4.60, for most of the values of the normalized obstacle position in z direction (z), Gaussian beam exhibit considerably higher percentage change of focus contrast data results (ΔI (%)), compared to the Airy Ring beam and so the losses in Gaussian beam are higher than the losses in Airy Ring beam. As a result, for most of the values of the normalized obstacle position in z direction, the Airy Ring beam is better than the Gaussian beam. So we prefer to use Airy Ring beam than the Gaussian beam because for most of the values of the normalized obstacle position in z direction (z), the losses in Airy Ring beam are lower than the losses in Gaussian beam.

Finally, in Figure 4.61, we compare the percentage change of focus position data results (ΔP (%)), as it is defined in Equation (4.2), from Airy Ring and Gaussian simulations for the case of π phase jump as a function of z position of the obstacle (z), which is normalized over the Airy Ring focal distance (f_0).

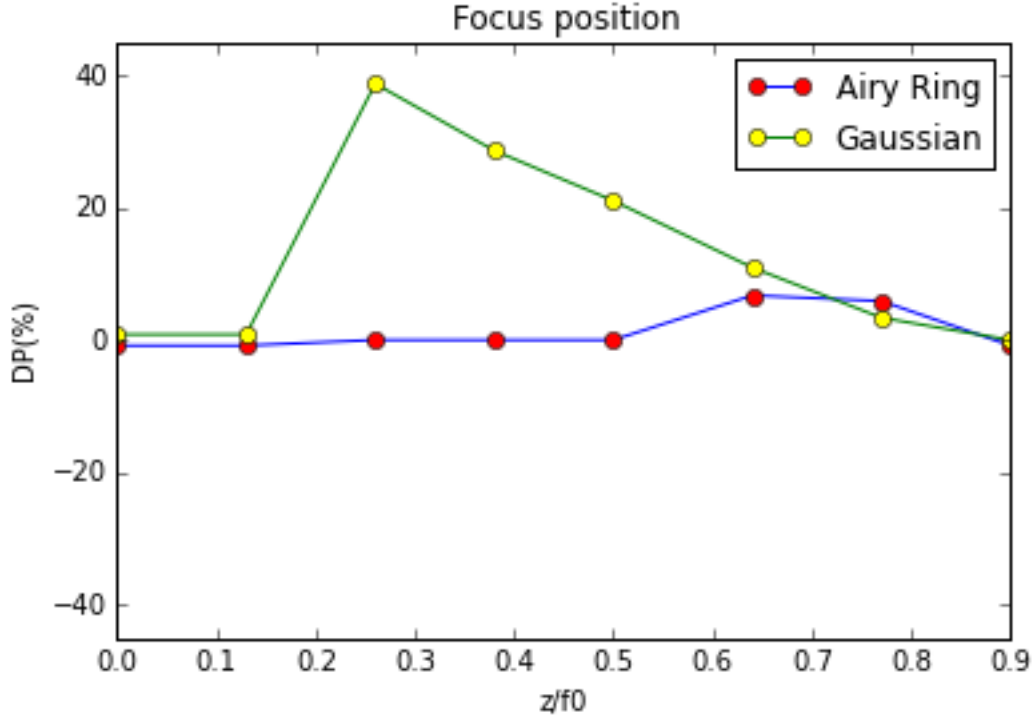


Figure 4.61: Comparison of the percentage change of focus position data results (ΔP (%)) from Airy Ring and Gaussian simulations for the case of π phase jump as a function of z position of the obstacle (z), which is normalized over the Airy Ring focal distance (f_0).

In Figure 4.61, for most of the values of the normalized obstacle position in z direction (z), Airy Ring beam exhibit considerably lower percentage change of focus position data results, compared to the Gaussian beam. For lower values of the normalized obstacle position in z direction (z), we observe a strong shift of the focus of the Gaussian beam. We observe this strong shift of the focus of the Gaussian beam because as the Gaussian beam passes through the glass obstacle, the diffraction phenomenon happens which moves the focus point of the Gaussian beam.

$\pi/2$ phase jump

Next, we follow the same steps as previous with the same Airy-Ring beam ($r_0=1\text{mm}$, $w_0=0.13\text{mm}$, $a=0.1$) but with a different circular glass. In this case the width of the glass is equal to $2*(r_0+w_0)$, the thickness of the glass is equal to $\lambda/4$ and its refractive index is equal to 1.0. This glass adds $\pi/2$ phase. In the following simulations the transverse coordinates (x,y) are discretized to 1024×1024 sampling points while 200 steps are used for the propagation along z direction. At following

graphs, we present the results of numerical simulation of the propagation of the Ring-Airy beam in the cases which the obstacle position z in z direction is different for every case. The obstacle position varies from the point $z=0$ up to Ring-Airy focus point. ($z=100.0\text{mm}$, 200.0mm , 390.0mm , 500.0mm , 600.0mm , 700.0mm).

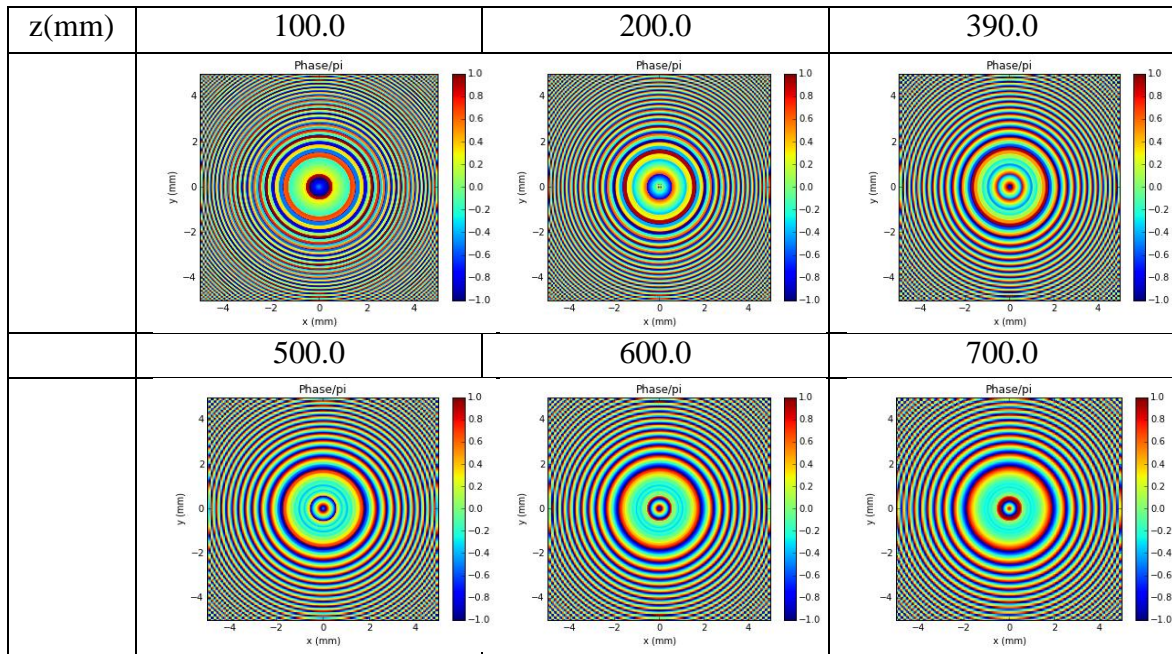


Figure 4.62: Beam phase after the circular glass for an Airy Ring beam with $r_0=1\text{mm}$, $w_0=0.13\text{mm}$ and $a=0.1$ which propagates in the presence of a circular glass for the case of $\pi/2$ phase jump with different position z in z direction in every case ($z=100.0\text{mm}$, 200.0mm , 390.0mm , 500.0mm , 600.0mm , 700.0mm).

Figure 4.62 depicts beam phase after the circular glass for an Airy Ring beam for the case of $\pi/2$ phase jump. When the obstacle position in z direction is equal to $z=100.0\text{mm}$, we observe that the phase in the center of the beam has a low value in π units. Interestingly, when the obstacle position in z direction is equal to $z=390.0\text{mm}$, the phase in the center of the beam has higher value in π units than the previous one. For higher values of the obstacle position in z direction ($z>390.0\text{mm}$), we observe that as the value of the glass position in z direction is increased, a secondary phase peak appears. This peak is due to the diffraction from the transparent obstacle and at some point becomes stronger than the primary phase peak. In all the cases we observe some artifacts at the edges of the square.

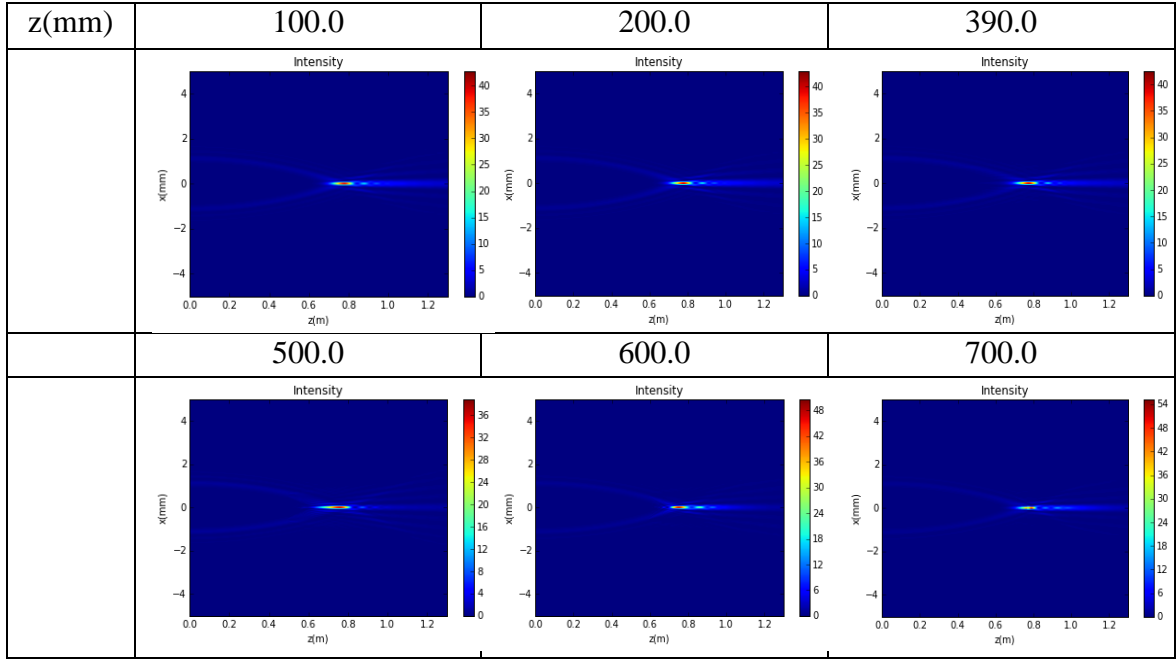


Figure 4.63: Intensity profile for an Airy Ring beam with $r_0=1\text{mm}$, $w_0=0.13\text{mm}$ and $a=0.1$ which propagates in the presence of a circular glass for the case of $\pi/2$ phase jump with different position z in z direction in every case ($z=100.0\text{mm}$, 200.0mm , 390.0mm , 500.0mm , 600.0mm , 700.0mm).

In Figure 4.63 we observe that as the value of the glass obstacle position in z direction is increased, a secondary peak appears. This peak is due to the diffraction from the transparent obstacle but it does not become stronger than the primary intensity peak. We observe also that for low values of the obstacle position in z direction (z), the intensity value at the focus point of the beam is high. When the obstacle position in z direction has a value which is equal to $z=500.0\text{mm}$, we observe that the beam scatters and deforms and the intensity at the focus point of the beam has a low value. For high values of the glass obstacle position in z direction ($z>500.0\text{mm}$), we observe that the Airy Ring beam focuses and the intensity value at the focus point of the beam is high. We observe also that for high values of the glass obstacle position in z direction ($z>500.0\text{mm}$), the focus point of the Airy Ring beam is moving. This is due to the diffraction from the transparent obstacle.

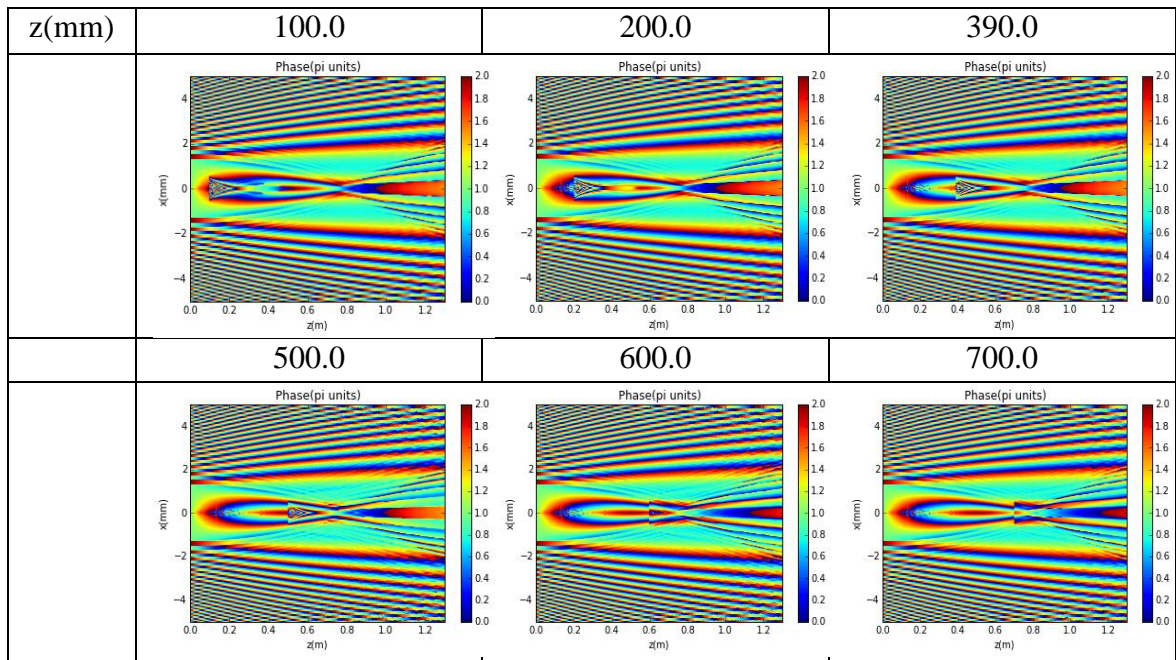


Figure 4.64: Phase profile for an Airy Ring beam with $r_0=1\text{mm}$, $w_0=0.13\text{mm}$ and $a=0.1$ which propagates in the presence of a circular glass for the case of $\pi/2$ phase jump with different position z in z direction in every case ($z=100.0\text{mm}$, 200.0mm , 390.0mm , 500.0mm , 600.0mm , 700.0mm).

Figure 4.64 depicts phase profile of the propagated Airy Ring beam for different values of position in z direction of the circular glass (z) for the case of $\pi/2$ phase jump. We observe at the Figure how the beam phase changes as the obstacle moves in z direction. The phase change is higher at the point where the glass obstacle is situated. For this case the phase jump at the point where the glass obstacle is situated is equal to $\pi/2$. As we can observe from the colorbars, the presence of a circular glass does not change much the Airy Ring beam phase. We can observe also the presence of artifacts.

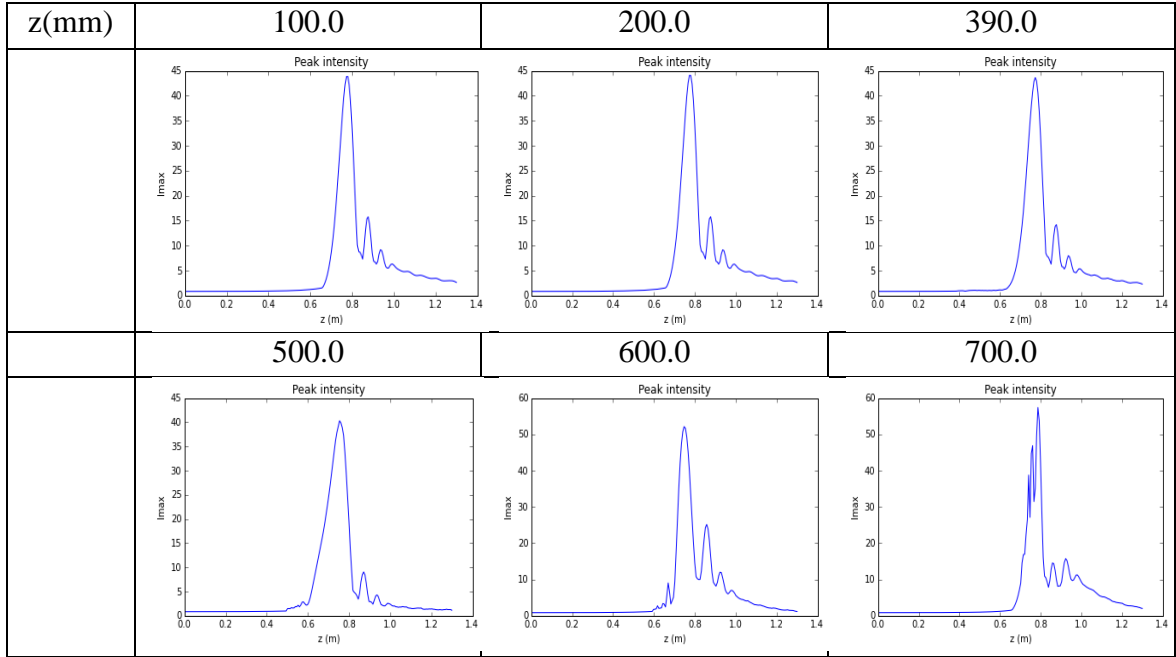


Figure 4.65: Maximum intensity profile for an Airy Ring beam with $r_0=1\text{mm}$, $w_0=0.13\text{mm}$ and $a=0.1$ which propagates in the presence of a circular glass for the case of $\pi/2$ phase jump with different position z in z direction in every case ($z=100.0\text{mm}$, 200.0mm , 390.0mm , 500.0mm , 600.0mm , 700.0mm).

Figure 4.65 depicts maximum intensity profile of the propagated Airy Ring beam for different values of the circular glass position in z direction (z) for the case of $\pi/2$ phase jump. It is shown that for lower values of z , the numerical and the theoretical maximum intensity profile have small discrepancy. For higher values of the obstacle position in z direction z , the discrepancy between the numerical and the theoretical maximum intensity profile is larger. For low values of the obstacle position in z direction ($z < 500.0\text{mm}$), we observe that the intensity at the focus point of the beam has a high value. For $z=500.0\text{mm}$, the intensity at the focus point of the beam has a low value. For high values of the obstacle position in z direction ($z > 500.0\text{mm}$), the intensity at the focus point of the beam has high value which is increased as the obstacle position in z direction increases. We observe also that a secondary intensity peak appears. This intensity peak is due to the diffraction from the transparent obstacle but it does not become stronger than the primary intensity peak.

In Figure 4.66, we compare the percentage change of focus contrast data results (ΔI (%)), as it is defined in Equation (4.1), from Airy Ring and Gaussian simulations for the case of $\pi/2$ phase jump as a function of z position of the obstacle (z), which is normalized over the Airy Ring focal distance (f_0).

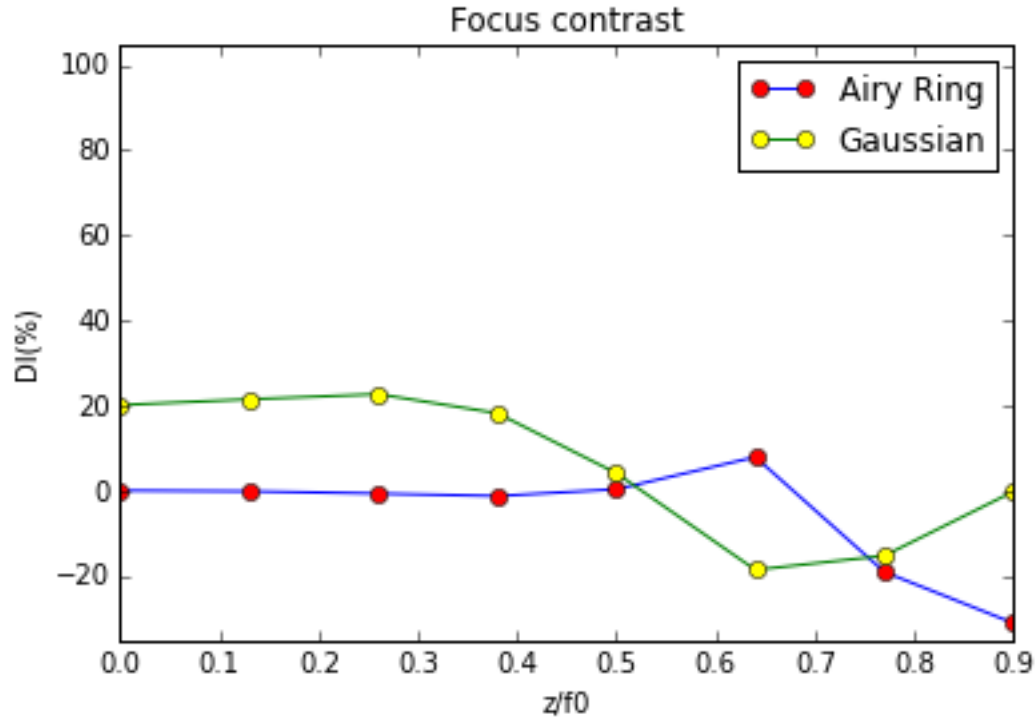


Figure 4.66: Comparison of the percentage change of focus contrast data results (ΔI (%)) from Airy Ring and Gaussian simulations for the case of $\pi/2$ phase jump as a function of z position of the obstacle (z), which is normalized over the Airy Ring focal distance (f_0).

In Figure 4.66, for most of the values of the normalized obstacle position in z direction (z), Gaussian beam exhibit considerably higher percentage change of focus contrast data results (ΔI (%)), compared to the Airy Ring beam and so the losses in Gaussian beam are higher than the losses in Airy Ring beam. As a result, for most of the values of the normalized obstacle position in z direction, the Airy Ring beam is better than the Gaussian beam. So we prefer to use Airy Ring beam in this case because the losses in Airy Ring beam are lower than the losses in Gaussian beam for most of the values of the normalized obstacle position in z direction (z).

Finally, in Figure 4.67, we compare the percentage change of focus position data results (ΔP (%)), as it is defined in Equation (4.2), from Airy Ring and Gaussian simulations for the case of $\pi/2$ phase jump as a function of z position of the obstacle (z), which is normalized over the Airy Ring focal distance (f_0).

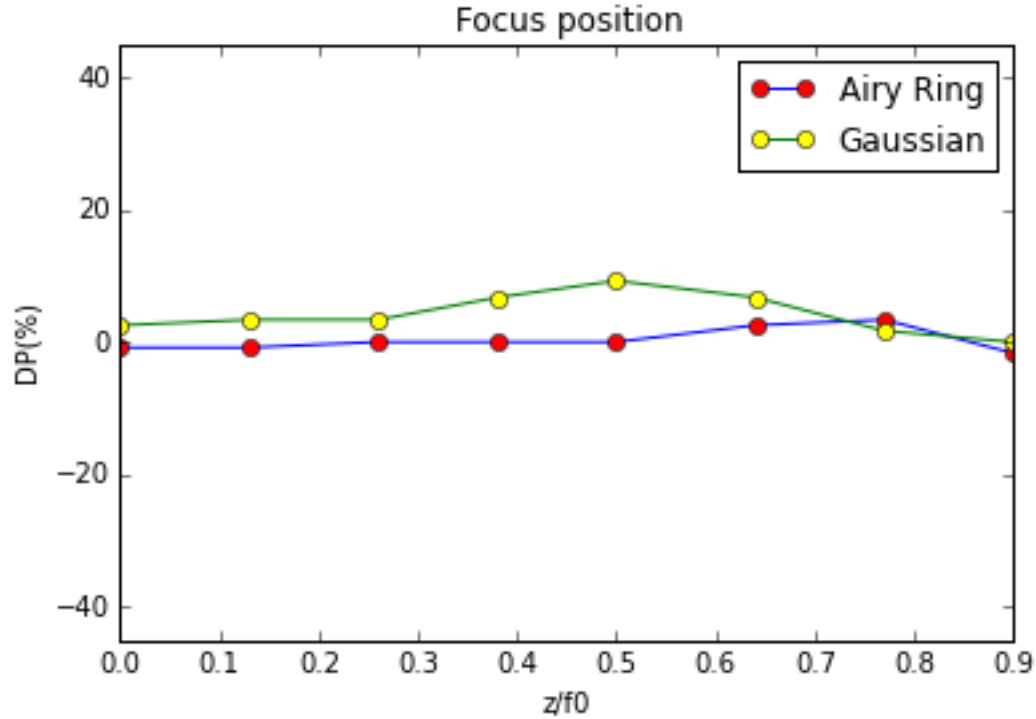


Figure 4.67: Comparison of the percentage change of focus position data results (ΔP (%)) from Airy Ring and Gaussian simulations for the case of $\pi/2$ phase jump as a function of z position of the obstacle (z), which is normalized over the Airy Ring focal distance (f_0).

In Figure 4.67, for most of the values of the normalized obstacle position in z direction (z), Airy Ring beam exhibit considerably lower percentage change of focus position data results, compared to the Gaussian beam. We observe that for high values of the normalized glass obstacle position in z direction, the focus point of the Airy Ring beam is moving far away from the focus point of the beam in the absence of the obstacle. This is due to the diffraction from the transparent obstacle.

c. Variable transverse position

π phase jump

The next step is to study the propagation of the same Ring-Airy beam as previous in which the circular glass has width which is equal to $2*(r_0+w_0)$, thickness which is equal to $\lambda/2$ and refractive index which is equal to 1.0. This glass adds π phase and we have put it in the middle between $z=0$ and the Ring-Airy focus point. In these

simulations the transverse coordinates (x,y) are also discretized to 1024x1024 sampling points while 200 steps are used for the propagation along z direction. At following graphs, we present the results of numerical simulation of the propagation of the Ring-Airy in the cases which the obstacle position x in x direction is different for every case.(x=0.26mm, 0.65mm, 1.04mm, 1.3mm, 1.69mm, 1.95mm).

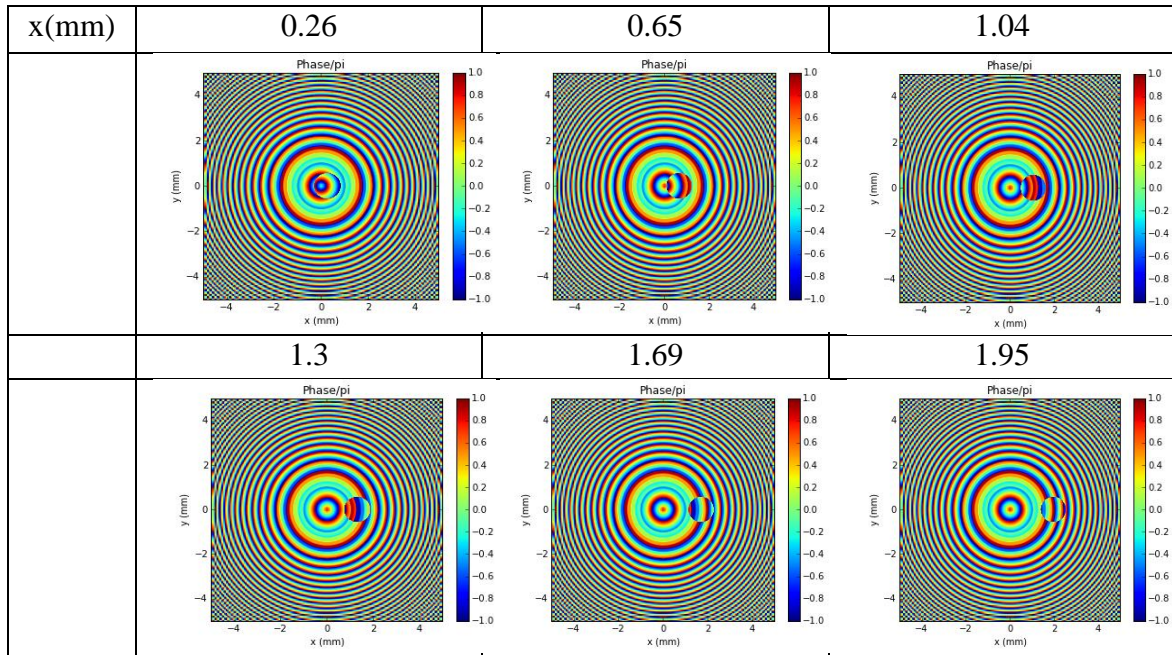


Figure 4.68: Beam phase after the circular glass for an Airy Ring beam with $r_0=1\text{mm}$, $w_0=0.13\text{mm}$ and $a=0.1$ which propagates in the presence of a circular glass for the case of π phase jump with different position x in x direction in every case (x=0.26mm, 0.65mm, 1.04mm, 1.3mm, 1.69mm, 1.95mm).

Figure 4.68 depicts beam phase after the circular glass for an Airy Ring beam for the case of π phase jump. In this Figure we observe a circle in the square which represents the circular glass. When the obstacle position in x direction has a value of $x=0.26\text{mm}$, the obstacle has been moved from the center of the beam a distance which is equal to 0.26mm. The Airy Ring beam has a hole in the center of it and as the obstacle moves far away from the center of the beam, it cuts more energy which does not reach at the focus point of the beam. As the value of obstacle position in x direction (x) increases, the movement of the circular glass from the center of the beam also increases. We observe that the phase values in pi units in colorbars remain constant which means that as the glass obstacle moves in x direction, the beam phase does not change enough. In all cases we observe some artifacts.

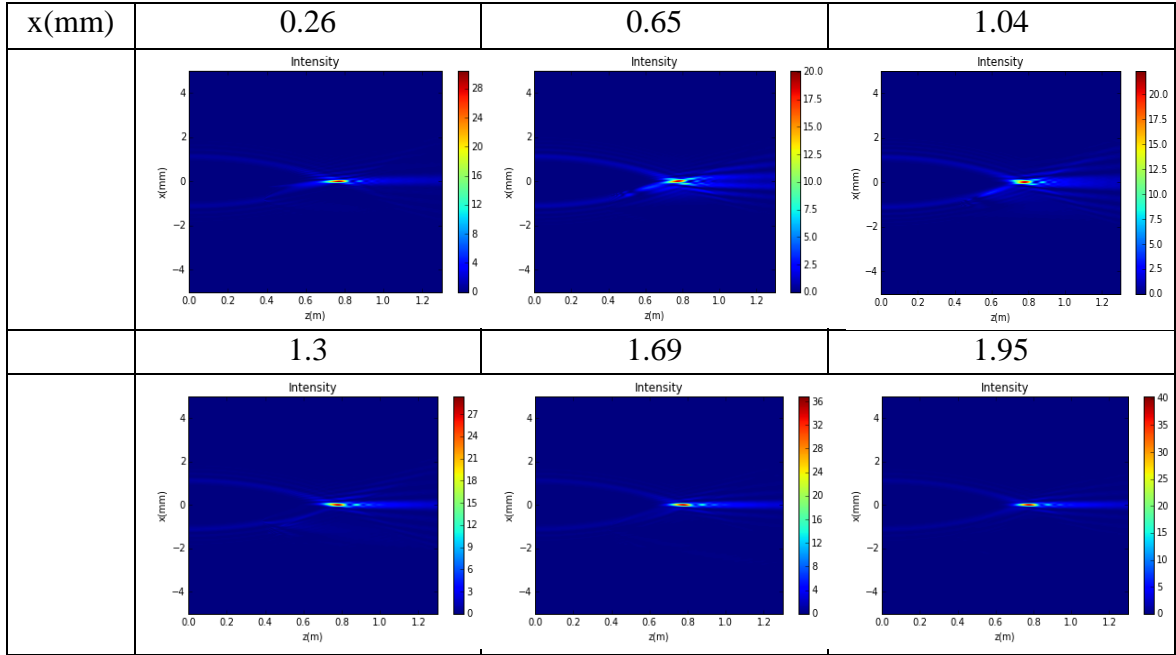


Figure 4.69: Intensity profile for an Airy Ring beam with $r_0=1\text{mm}$, $w_0=0.13\text{mm}$ and $a=0.1$ which propagates in the presence of a circular glass for the case of π phase jump with different position x in x direction in every case ($x=0.26\text{mm}$, 0.65mm , 1.04mm , 1.3mm , 1.69mm , 1.95mm).

Figure 4.69 depicts intensity profile of the propagated Airy Ring beam for different values of position in x direction of the circular glass (x) for the case of π phase jump. It is shown that for lower values of x , the beam scatters and deforms, whereas for higher values of x it focuses. For the case which the obstacle position in x direction is equal to $x=0.26\text{mm}$, we observe a high value of intensity at the focus point of the beam which is decreased when the obstacle position in x direction is equal to $x=0.65\text{mm}$. For high values of obstacle position in x direction, we observe that a secondary peak appears. This peak is due to the diffraction from the transparent obstacle but it does not become stronger than the primary intensity peak.

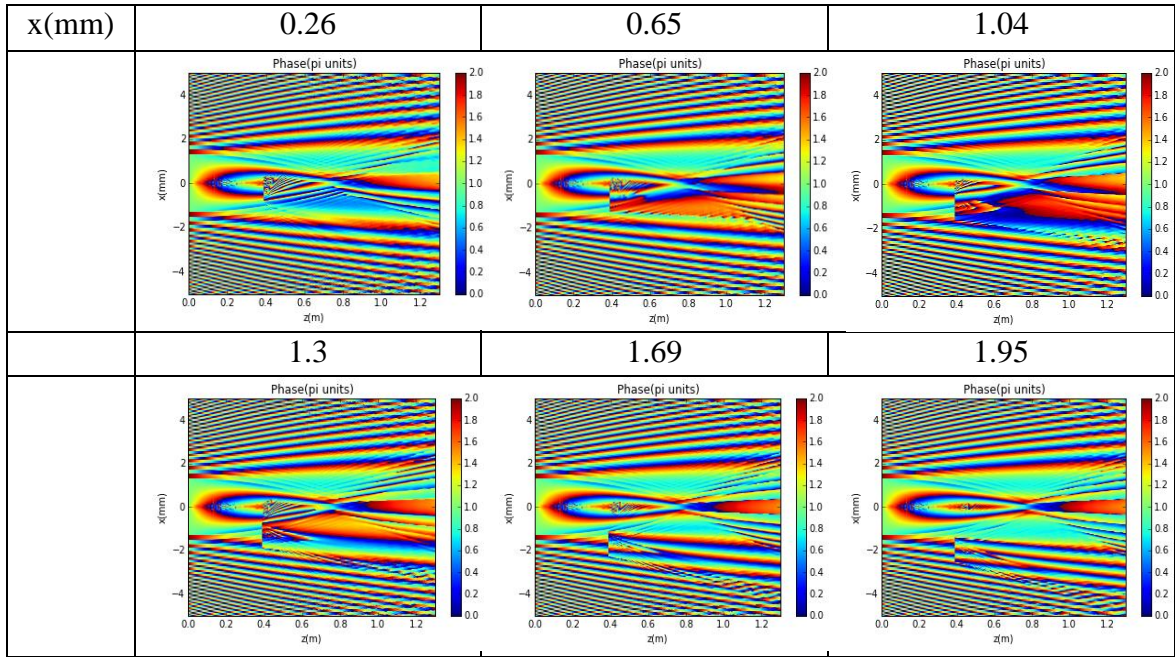


Figure 4.70: Phase profile for an Airy Ring beam with $r_0=1\text{mm}$, $w_0=0.13\text{mm}$ and $a=0.1$ which propagates in the presence of a circular glass for the case of π phase jump with different position x in x direction in every case ($x=0.26\text{mm}$, 0.65mm , 1.04mm , 1.3mm , 1.69mm , 1.95mm).

Figure 4.70 depicts phase profile of the propagated Airy Ring beam for different values of position in x direction of the circular glass (x) for the case of π phase jump. It is shown that for lower values of x , the beam scatters and deforms, whereas for higher values of x it focuses. We observe at the Figure how the beam phase changes as the obstacle moves in x direction. As we can observe from the colorbars, the presence of a circular glass does not change much the Airy Ring beam phase. We can observe also the presence of artifacts.

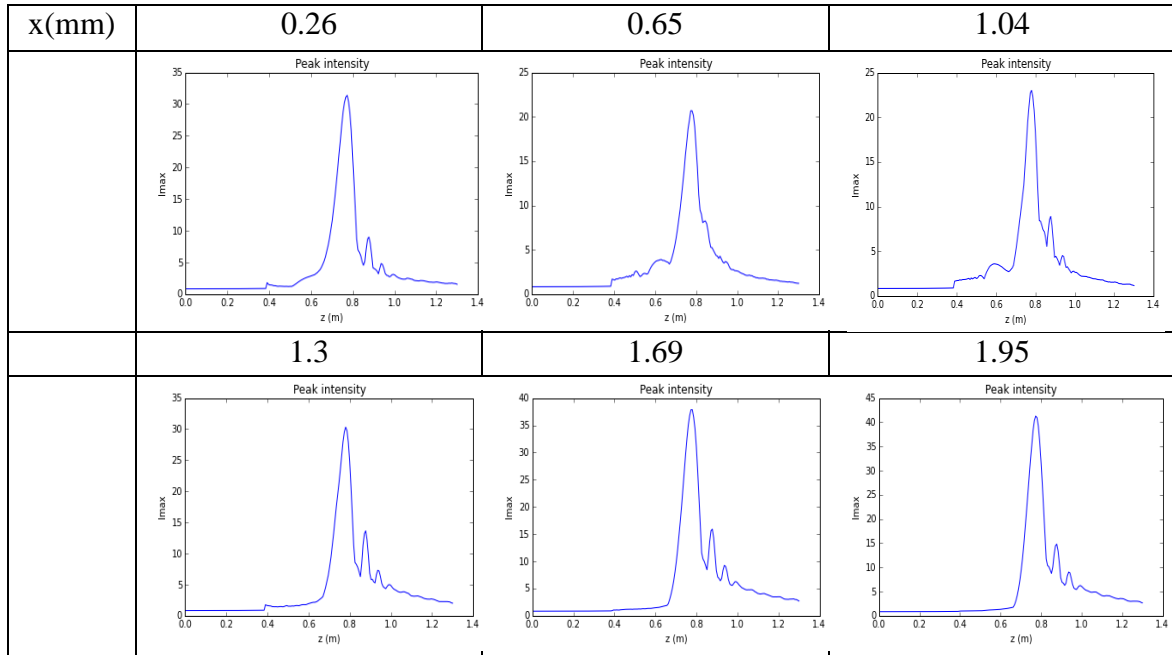


Figure 4.71: Maximum intensity profile for an Airy Ring beam with $r_0=1\text{mm}$, $w_0=0.13\text{mm}$ and $a=0.1$ which propagates in the presence of a circular glass for the case of π phase jump with different position x in x direction in every case ($x=0.26\text{mm}$, 0.65mm , 1.04mm , 1.3mm , 1.69mm , 1.95mm).

Figure 4.71 depicts maximum intensity profile of the propagated Airy Ring beam for different values of position in x direction of the circular glass (x) for the case of π phase jump. It is shown that for lower values of x , the numerical and the theoretical maximum intensity profile have large discrepancy. For higher values of the obstacle position in x direction, the discrepancy between the numerical and the theoretical maximum intensity profile is smaller. For the case which the obstacle position in x direction is equal to $x=0.26\text{mm}$, we observe a high value of intensity at the focus point of the beam which is decreased when the obstacle position in x direction is equal to $x=0.65\text{mm}$. It happens because the Airy Ring beam has a hole in the center of it and as the obstacle moves far away from the center of the beam, it cuts more energy which does not reach at the focus point of the beam. For higher values of the obstacle position in x direction ($x>0.65\text{mm}$) we observe that as the value of obstacle position in x direction increases, the peak intensity at the focus point of the beam also increases. This happens because as the obstacle is moving far away from the center of the beam, it cuts less energy and so more energy reaches at the focus point of the beam.

In Figure 4.72, we compare the percentage change of focus contrast data results (ΔI (%)), as it is defined in Equation (4.1), from Airy Ring and Gaussian simulations for the case of π phase jump as a function of x position of the obstacle (x), which is normalized over the ring radius of the Airy Ring beam (r_0+w_0).

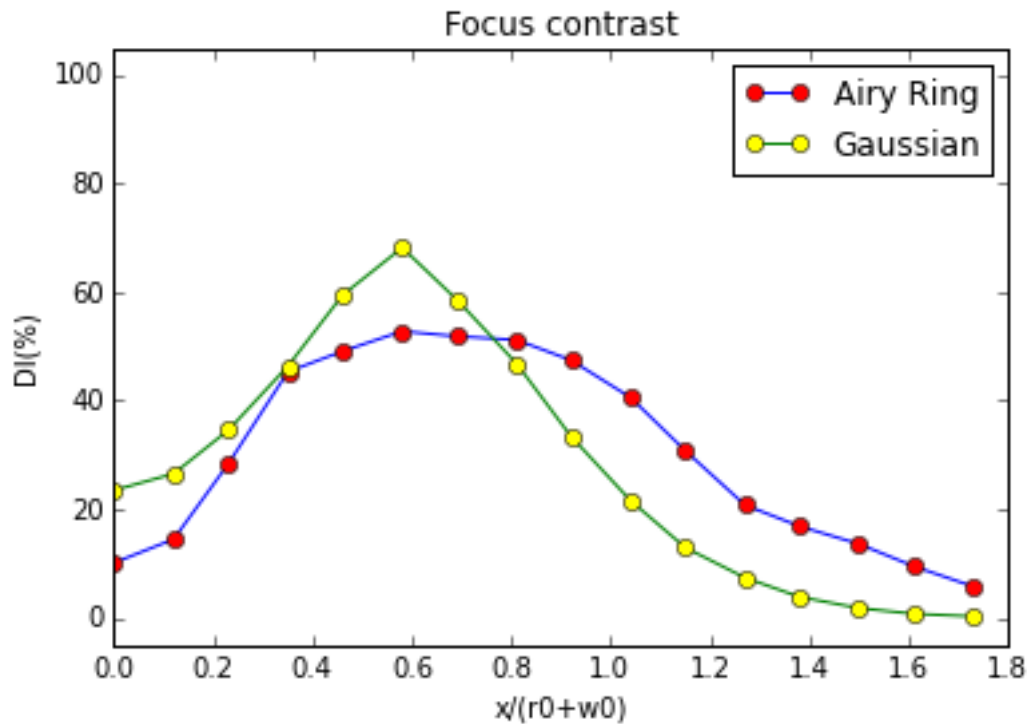


Figure 4.72: Comparison of the percentage change of focus contrast data results (ΔI (%)) from Airy Ring and Gaussian simulations for the case of π phase jump as a function of x position of the obstacle (x), which is normalized over the ring radius of the Airy Ring beam (r_0+w_0).

In Figure 4.72, at lower values of the normalized obstacle position in x direction (x), Gaussian beam exhibit considerably higher percentage change of focus contrast data results (ΔI (%)), compared to the Airy Ring beam and so the losses in Gaussian beam are higher than the losses in Airy Ring beam. Interestingly, at higher values of the normalized obstacle position in x direction (x), Airy Ring beam exhibit considerably higher percentage change of focus contrast data results, compared to the Gaussian beam and so the losses in Airy Ring beam are higher than the losses in Gaussian beam. As a result, for low values of the normalized obstacle position in x direction, the Airy Ring beam is better than the Gaussian beam but for high values of the normalized obstacle position in x direction, the Gaussian beam is better than the Airy Ring beam. So for low values of the normalized obstacle position in x direction

we prefer to use Airy Ring beam but for high values of the normalized obstacle position in x direction we prefer to use Gaussian beam.

Finally, in Figure 4.73, we compare the percentage change of focus position data results (ΔP (%)), as it is defined in Equation (4.2), from Airy Ring and Gaussian simulations for the case of π phase jump as a function of x position of the obstacle (x), which is normalized over the ring radius of the Airy Ring beam (r_0+w_0).

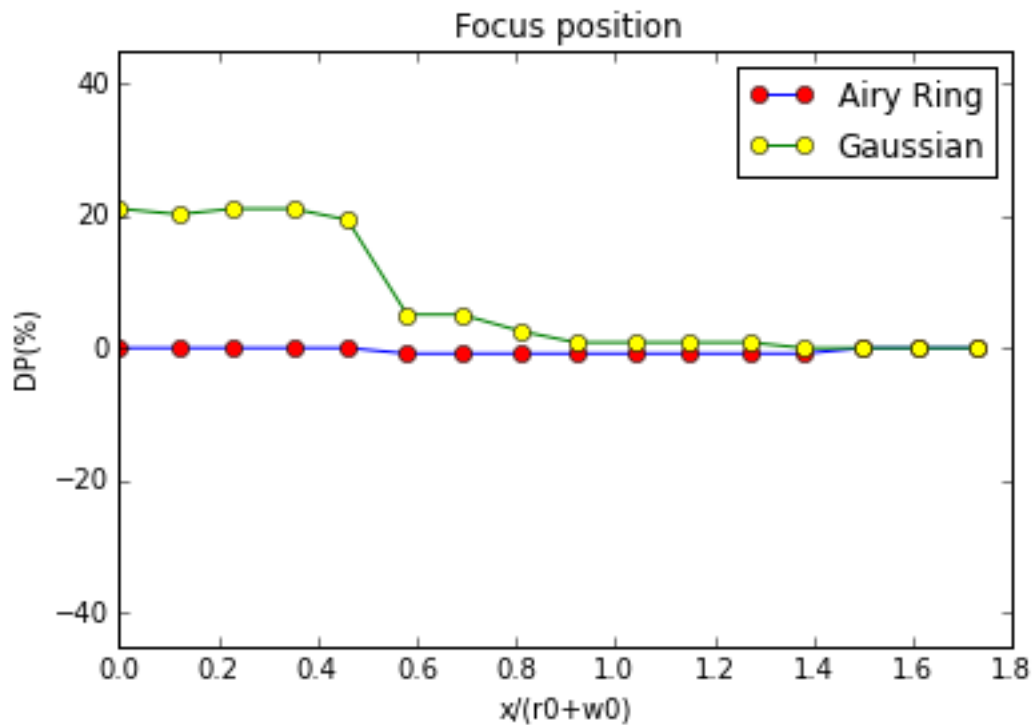


Figure 4.73: Comparison of the percentage change of focus position data results (ΔP (%)) from Airy Ring and Gaussian simulations for the case of π phase jump as a function of x position of the obstacle (x), which is normalized over the ring radius of the Airy Ring beam (r_0+w_0).

In Figure 4.73, at lower values of the normalized obstacle position in x direction (x), Airy Ring beams exhibit considerably lower percentage change of focus position data results, compared to the Gaussian beams. At higher values of the normalized obstacle position in x direction (x), Airy Ring and Gaussian beams have around the same values of percentage change of focus position data results. We observe that the focus point of the Gaussian beam shifts because as the Gaussian beam passes through the glass obstacle, the diffraction phenomenon happens which moves the focus point of the Gaussian beam.

$\pi/2$ phase jump

Next, we follow the same steps as previous with the same Airy-Ring beam ($r_0=1\text{mm}$, $w_0=0.13\text{mm}$, $a=0.1$) but with a different circular glass. In this case the width of the glass is equal to $2*(r_0+w_0)$, the thickness of the glass is equal to $\lambda/4$ and its refractive index is equal to 1.0. This glass adds $\pi/2$ phase. In the following simulations the transverse coordinates (x,y) are discretized to 1024×1024 sampling points while 200 steps are used for the propagation along z direction. At following graphs, we present the results of numerical simulation of the propagation of the Ring-Airy beam in the cases which the obstacle position x in x direction is different for every case. ($x=0.26\text{mm}$, 0.65mm , 1.04mm , 1.3mm , 1.69mm , 1.95mm).

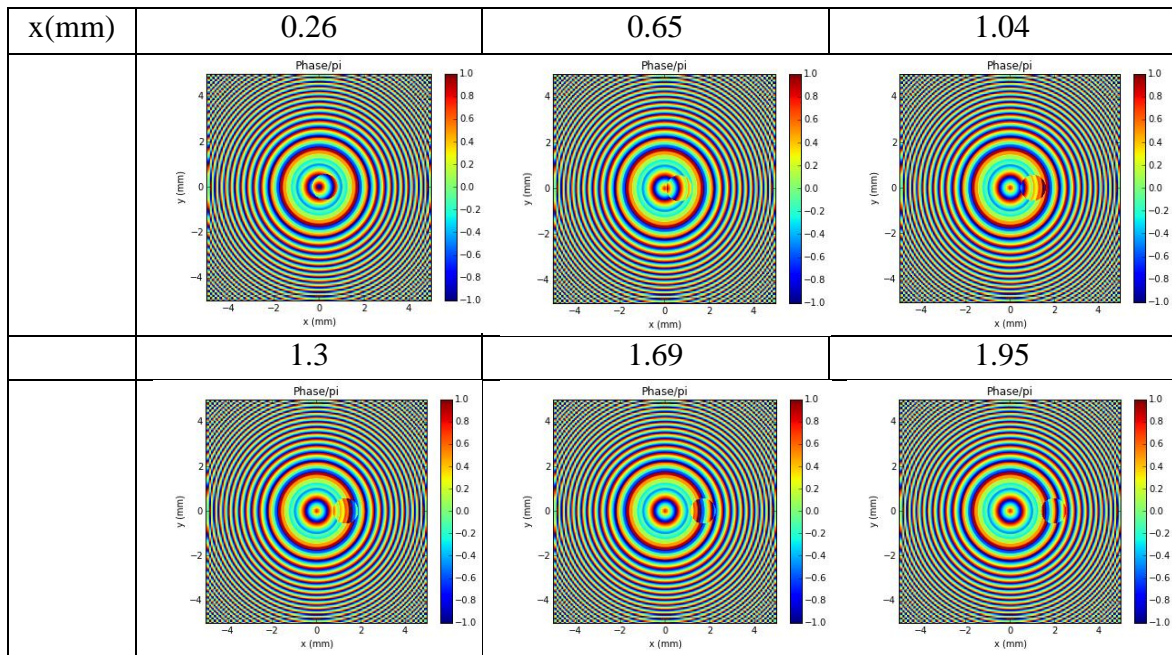


Figure 4.74: Beam phase after the circular glass for an Airy Ring beam with $r_0=1\text{mm}$, $w_0=0.13\text{mm}$ and $a=0.1$ which propagates in the presence of a circular glass for the case of $\pi/2$ phase jump with different position x in x direction in every case ($x=0.26\text{mm}$, 0.65mm , 1.04mm , 1.3mm , 1.69mm , 1.95mm).

Figure 4.74 depicts beam phase after the circular glass for an Airy Ring beam for the case of $\pi/2$ phase jump. In this Figure we observe a circle in the square which represents the circular glass. When the obstacle position in x direction has a value of $x=0.26\text{mm}$, the obstacle has been moved from the center of the beam a distance which is equal to 0.26mm . The Airy Ring beam has a hole in the center of it and as the

obstacle moves far away from the center of the beam, it cuts more energy which does not reach at the focus point of the beam. As the value of obstacle position in x direction (x) increases, the movement of the circular glass from the center of the beam also increases. We observe that the phase values in pi units in colorbars remain constant which means that as the glass obstacle moves in x direction, the beam phase does not change enough. In all cases we observe some artifacts.

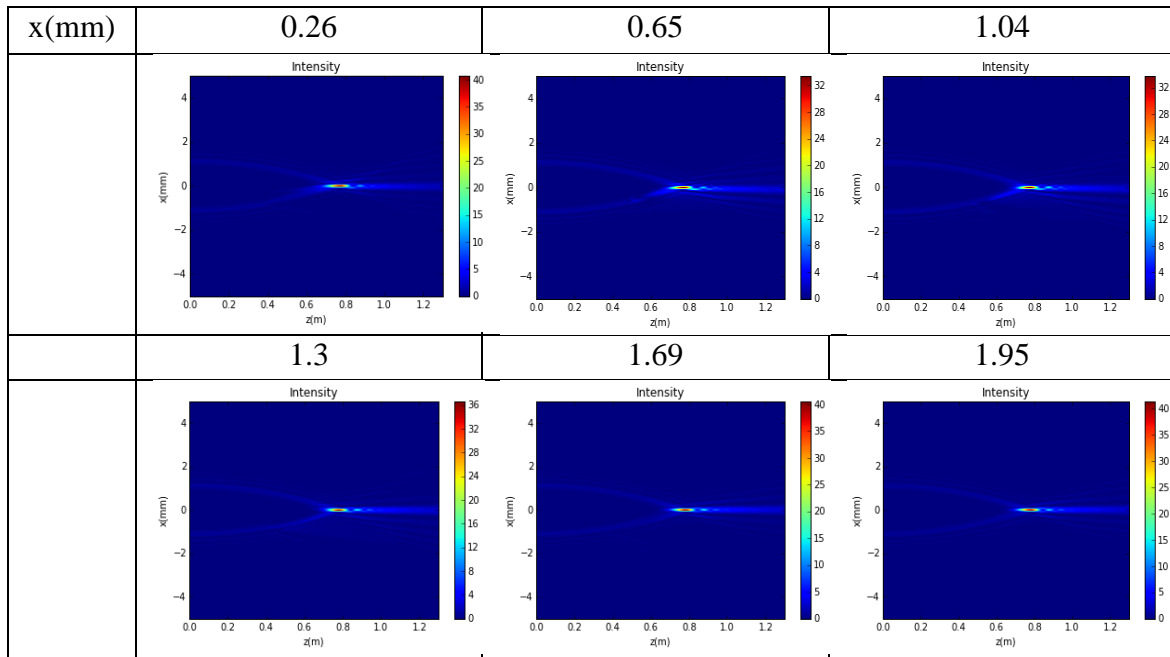


Figure 4.75: Intensity profile for an Airy Ring beam with $r_0=1\text{mm}$, $w_0=0.13\text{mm}$ and $a=0.1$ which propagates in the presence of a circular glass for the case of $\pi/2$ phase jump with different position x in x direction in every case ($x=0.26\text{mm}$, 0.65mm , 1.04mm , 1.3mm , 1.69mm , 1.95mm).

Figure 4.75 depicts intensity profile of the propagated Airy Ring beam for different values of position in x direction of the circular glass (x) for the case of $\pi/2$ phase jump. It is shown that for lower values of x, the beam scatters and deforms, whereas for higher values of x it focuses. For the case which the obstacle position in x direction is equal to $x=0.26\text{mm}$, we observe a high value of intensity at the focus point of the beam which is higher than the intensity value for the case of π phase jump. It is decreased when the obstacle position in x direction is equal to $x=0.65\text{mm}$ but this intensity value is also higher than the intensity value for the case of π phase jump. For high values of obstacle position in x direction, we observe that a secondary

peak appears. This peak is due to the diffraction from the transparent obstacle but it does not become stronger than the primary intensity peak.

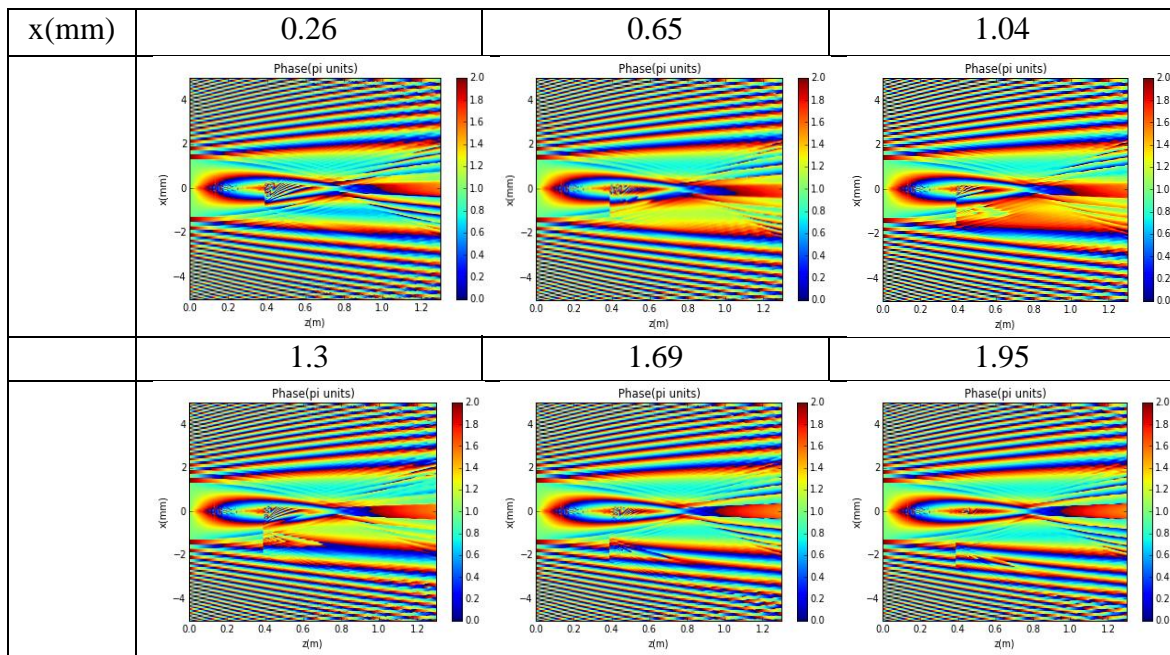


Figure 4.76: Phase profile for an Airy Ring beam with $r_0=1\text{mm}$, $w_0=0.13\text{mm}$ and $a=0.1$ which propagates in the presence of a circular glass for the case of $\pi/2$ phase jump with different position x in x direction in every case ($x=0.26\text{mm}$, 0.65mm , 1.04mm , 1.3mm , 1.69mm , 1.95mm).

Figure 4.76 depicts phase profile of the propagated Airy Ring beam for different values of position in x direction of the circular glass (x) for the case of $\pi/2$ phase jump. It is shown that for lower values of x , the beam scatters and deforms, whereas for higher values of x it focuses. We observe at the Figure how the beam phase changes as the obstacle moves in x direction. As we can observe from the colorbars, the presence of a circular glass does not change much the Airy Ring beam phase. We can observe also the presence of artifacts.

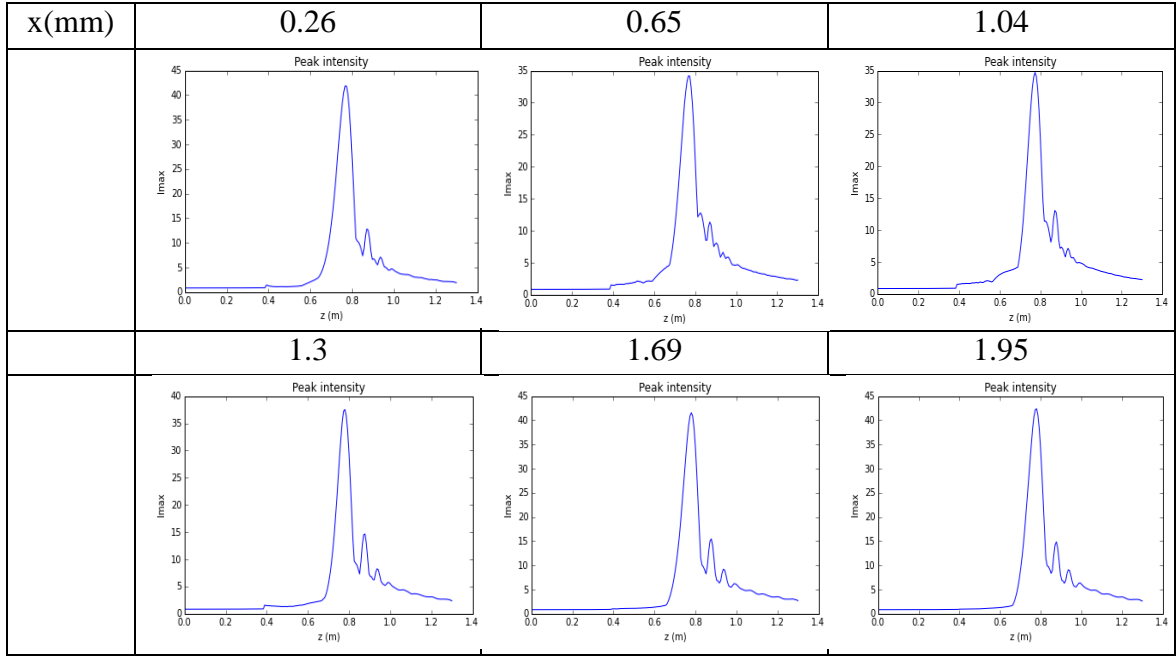


Figure 4.77: Maximum intensity profile for an Airy Ring beam with $r_0=1\text{mm}$, $w_0=0.13\text{mm}$ and $a=0.1$ which propagates in the presence of a circular glass for the case of $\pi/2$ phase jump with different position x in x direction in every case ($x=0.26\text{mm}$, 0.65mm , 1.04mm , 1.3mm , 1.69mm , 1.95mm).

Figure 4.77 depicts maximum intensity profile of the propagated Airy Ring beam for different values of position in x direction of the circular glass (x) for the case of $\pi/2$ phase jump. It is shown that for lower values of x , the numerical and the theoretical maximum intensity profile have large discrepancy. For higher values of the obstacle position in x direction, the discrepancy between the numerical and the theoretical maximum intensity profile is smaller. For the case which the obstacle position in x direction is equal to $x=0.26\text{mm}$, we observe a high value of intensity at the focus point of the beam which is decreased when the obstacle position in x direction is equal to $x=0.65\text{mm}$. It happens because the Airy Ring beam has a hole in the center of it and as the obstacle moves far away from the center of the beam, it cuts more energy which does not reach at the focus point of the beam. For higher values of the obstacle position in x direction ($x>0.65\text{mm}$) we observe that as the value of obstacle position in x direction increases, the peak intensity at the focus point of the beam also increases. This happens because as the obstacle is moving far away from the center of the beam, it cuts less energy and so more energy reaches at the focus point of the beam.

In Figure 4.78, we compare the percentage change of focus contrast data results (ΔI (%)), as it is defined in Equation (4.1), from Airy Ring and Gaussian simulations for the case of $\pi/2$ phase jump as a function of x position of the obstacle (x), which is normalized over the ring radius of the Airy Ring beam (r_0+w_0).

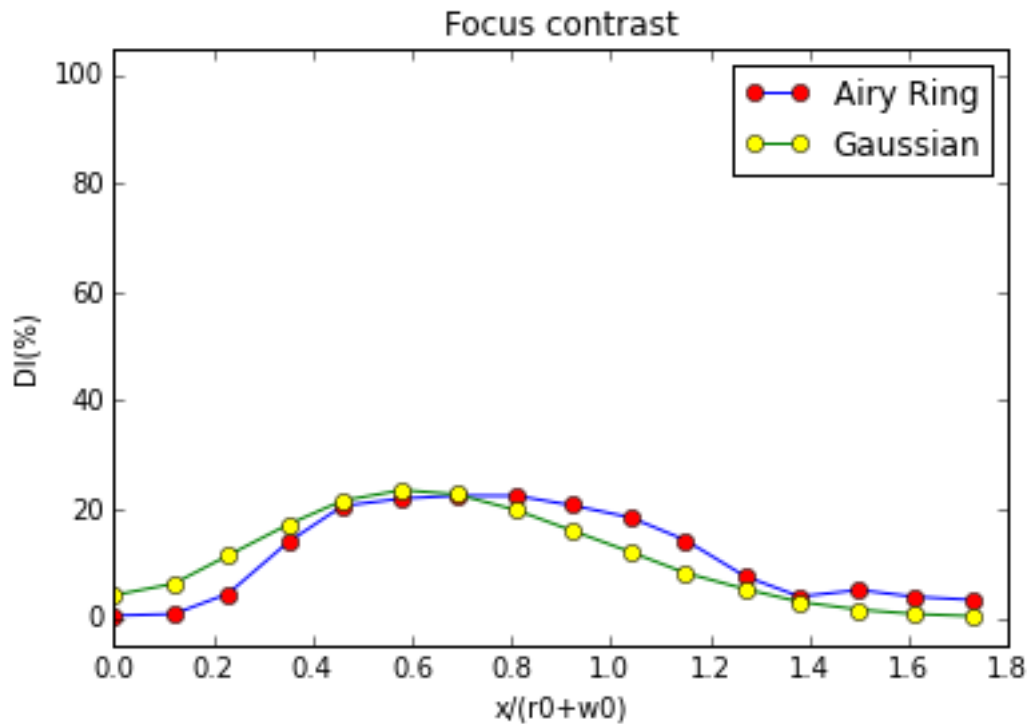


Figure 4.78: Comparison of the percentage change of focus contrast data results (ΔI (%)) from Airy Ring and Gaussian simulations for the case of $\pi/2$ phase jump as a function of x position of the obstacle (x), which is normalized over the ring radius of the Airy Ring beam (r_0+w_0).

In Figure 4.78, at lower values of the normalized obstacle position in x direction (x), Gaussian beams exhibit considerably higher percentage change of focus contrast data results (ΔI (%)), compared to the Airy Ring beams and so the losses in Gaussian beams are higher than the losses in Airy Ring beams. Interestingly, at higher values of the normalized obstacle position in x direction (x), Airy Ring beams exhibit considerably higher percentage change of focus contrast data results, compared to the Gaussian beams and so the losses in Airy Ring beams are higher than the losses in Gaussian beams. As a result, for low values of the normalized obstacle position in x direction, the Airy Ring beam is better than the Gaussian beam but for high values of the normalized obstacle position in x direction, the Gaussian beam is better than the Airy Ring beam. So for low values of the normalized obstacle position in x direction

we prefer to use Airy Ring beam but for high values of the normalized obstacle position in x direction we prefer to use Gaussian beam.

Finally, in Figure 4.79, we compare the percentage change of focus position data results (ΔP (%)), as it is defined in Equation (4.2), from Airy Ring and Gaussian simulations for the case of $\pi/2$ phase jump as a function of x position of the obstacle (x), which is normalized over the ring radius of the Airy Ring beam (r_0+w_0).

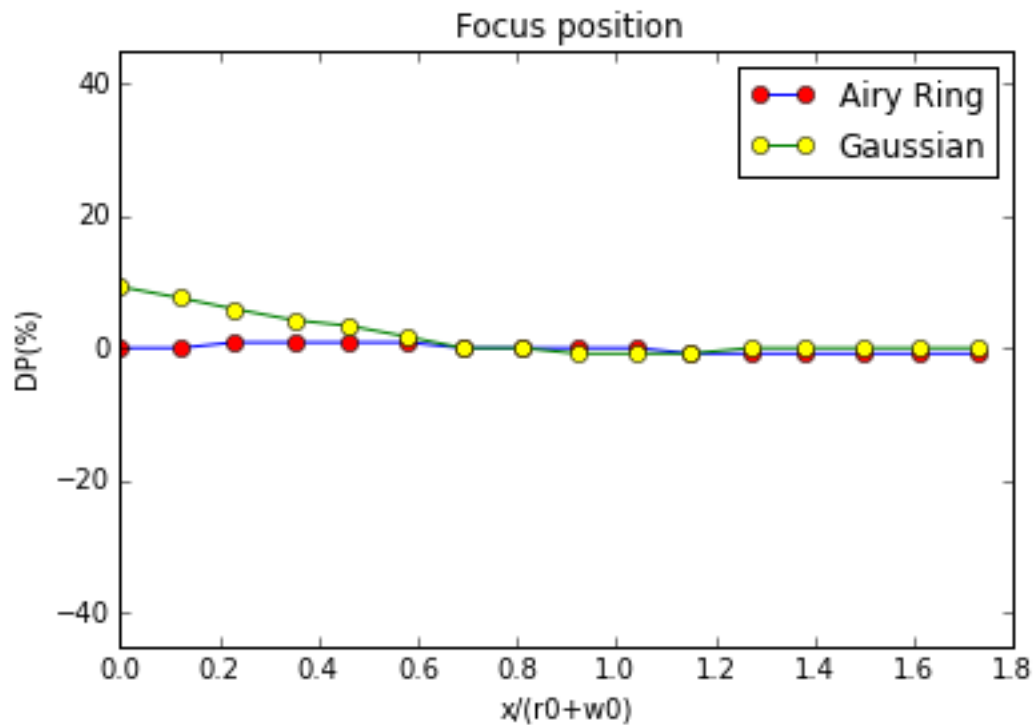


Figure 4.79: Comparison of the percentage change of focus position data results (ΔP (%)) from Airy Ring and Gaussian simulations for the case of $\pi/2$ phase jump as a function of x position of the obstacle (x), which is normalized over the ring radius of the Airy Ring beam (r_0+w_0).

In Figure 4.79, at lower values of the normalized obstacle position in x direction (x), Airy Ring beams exhibit considerably lower percentage change of focus position data results, compared to the Gaussian beams. At higher values of the normalized obstacle position in x direction (x), Airy Ring and Gaussian beams have around the same values of percentage change of focus position data results which drop to 0. This means that for higher values of the normalized obstacle position in x direction, the focus position of every of the two beams drops to the focus position of the beam in the absence of the obstacle.

5. Conclusions

As a conclusion, our numerical experiments show that obstacles, depending on their type and position, lead to a different type of behavior in the propagation of Gaussian and Airy Ring beams. In the case of absorbing obstacles their effect is strongly depending on their location. The blocked part of the beam leads to less energy at the focus and thus less intensity. Ring Airy beams, although affected, are more resilient to this type of obstacles. One reason for this is that the Airy Ring beam is hollow with its energy distributed over a large area, in contrast to Gaussian beams where the energy is distributed around their center. For a Gaussian beam, the amount of blocked energy is roughly proportional to the obstacle's surface area. In the case of ring-Airy beam this holds only in the case of medium to large sized, compared to the primary ring radius, obstacles.

On the other hand, in the case of refracting obstacles, the energy is redirected, mainly due to diffraction,; leading to secondary intensity peaks. Under certain conditions this secondary peak can become stronger than the primary intensity peak. Ring –Airy beams, as well as Gaussian beams are affected by the presence of refracting obstacles. The qualitative behavior though is different. Furthermore, the qualitative behavior depends on the strength of such obstacles as it is expressed by the phase change. Comparing the π and $\pi/2$ phase change cases, we observe that in the case of π phase change, the diffracted part of the beam interferes destructively with the non-diffracted part and leads to a reduction of the intensity in the focus. On the other hand this effect is minimized in the case of the $\pi/2$ phase jump.

Appendix A

Simple, not optimized, code of Python for Gaussian 2D propagation in free space:

```
#Angular spectrum Gaussian 2D propagation in free space

import math
import numpy as np
import datetime
from sympy import exp, I, pi
from tempfile import TemporaryFile
outfile = TemporaryFile()

import Angular_spectrum_initialization_2D as init

#Gaussian beam definition with parameter FWHM wg
def Gaussian(di,dii,wg):
c=float(math.e**(-4*math.log(2)*((Xs[di]**2+Ys[dii]**2)/wg**2)))
return c

#Gaussian beam definition with parameter beam waist w0
def Gaussian(di,dii,w0):
c=float(math.e**(-((Xs[di]**2+Ys[dii]**2)/w0**2)))
return c

#physical parameters
k0=(2*math.pi)/init.lamda #evaluation of wavenumber
w0=float(init.wg/math.sqrt(4*math.log(2))) #evaluation of beam waist
zR=float(math.pi*(init.w0)**2/init.lamda) #evaluation of confocal
#parameter

Xmax=float(init.window/2) #Maximum x value
Ymax=float(init.window/2) #Maximum y value

dx=float(init.window/init.Nx) #x resolution (meters/pixel)
dy=float(init.window/init.Ny) #y resolution (meters/pixel)

dz=float(init.Zmax/init.Nz) #z resolution (meters/step)
dkx=float(math.pi/Xmax) #k space resolution (meters^-1/pixel) in x
#direction
dky=float(math.pi/Ymax) #k space resolution (meters^-1/pixel) in y #direction

kxmax=float(dkx*init.Nx/2) #Maximum spatial frequency in x #direction
kymax=float(dky*init.Ny/2) #Maximum spatial frequency in y #direction

#preparation of kx,ky and x,y space lists
Kx=np.array([float(-kxmax+dkx*(di-1))for di in range (1,init.Nx+1)])
Ky=np.array([float(-kymax+dky*(di-1))for di in range (1,init.Ny+1)])
Xs=np.array([float(-Xmax+dx*(di-1))for di in range (1,init.Nx+1)])
Ys=np.array([float(-Ymax+dy*(di-1))for di in range (1,init.Ny+1)])

#create a discretized Gaussian beam
DBeam=np.empty((init.Nx, init.Ny),np.complex128)
```

```

for di in range(0, init.Nx):
    for dii in range(0, init.Ny):
        DBeam[di,dii]=Gaussian(di,dii,init.w0)

#Propagators
#paraxial propagator kernel
Tpr=np.empty((init.Nx, init.Ny),np.complex128)
for di in range(0, init.Nx):
    for dii in range(0, init.Ny):
        Tpr[di,dii]=exp(-1*init.lamda/(4*pi))*dz*(Kx[di]**2+Ky[dii]**2)

#Main iteration routine
Chess=np.empty((init.Nx,init.Ny),np.complex128)
for di in range(0,init.Nx):
    for dii in range(0,init.Ny):
        Chess[di,dii]=(-1)**(di+dii)

#initialize lists to store results
PrBeam=np.empty(shape=[init.Nz+2,init.Nx,init.Ny],dtype=np.complex128)
lmax=np.empty(shape=[init.Nz+2],dtype=np.float64)
PrBeam[0]=DBeam
gmax=np.amax(PrBeam[0])
lmax[0]=abs(gmax)**2

#iteration core
for dj in range (0,init.Nz+1):
    FBeam0=np.fft.fft2(DBeam*Chess)
    DBeam=np.fft.ifft2(FBeam0*Tpr)*Chess
    PrBeam[dj+1]=DBeam
    lmax[dj+1]=np.amax(abs(DBeam)**2)

#Intensity(x,y) over all z steps
# evaluation of slice position
YSlicePos=round((init.YSlice+Ymax)/dy)+1
Vis2=np.empty(shape=[init.Nz+2,init.Nx],dtype=np.complex128)
for di in range(0,init.Nz+2):
    for dii in range(0,init.Nx):
        Vis2[di,dii]=PrBeam[di,dii,YSlicePos]

mydate =datetime.datetime.now().strftime("%d-%m-%y-%H-%M-%S")

#Save Vis2 elements in a Results_l{Time_Stamp}.txt file
np.savetxt('Results_l%s.txt'%mydate,Vis2.view(float))

#Save lmax elements in a Results_lmax{Time_Stamp}.txt file
np.savetxt('Results_lmax%s.txt'%mydate,lmax)

#Read Results Gaussian 2D propagation in free space python file

import numpy as np
import matplotlib.pyplot as plt
from tempfile import TemporaryFile
outfile = TemporaryFile()

```

```

from scipy.optimize import curve_fit

import Angular_spectrum_initialization_2D as init

new_data = np.loadtxt('Results_I07-08-15-14-39-59.txt').view(complex)
new_data1=np.loadtxt('Results_Imax07-08-15-14-39-59.txt')
Xmax=float(init.window/2)

#Visualization

#Max(Intensity(x)) as a function of z
plt.close("all")
plt.figure(1)
x=np.empty(shape=[init.Nz+2],dtype=np.float64)
for di in range(0,init.Nz+2):
    x[di]=di*(init.Zmax/(init.Nz+1))
plt.plot(x,new_data1)
plt.title("Peak intensity")
plt.xlabel('z(m)')
plt.ylabel('Imax')
plt.show

#Fitting Imax data
def fit_func(x,zR):
    return 1/(1+(x/zR)**2)
popt, pcov= curve_fit(fit_func, x, new_data1)
plt.plot(x, fit_func(x, *popt), 'r-')
print ("Η πειραματική τιμή του μήκους Rayleigh είναι zR=", popt[0])
#Intensity
iml=np.transpose(np.absolute(new_data)**2)

#Draw Intensity
plt.figure(2)
plt.imshow(iml,extent=[0,init.Zmax,-Xmax*1000,Xmax*1000])
plt.colorbar()
plt.title("Intensity")
plt.xlabel('z(m)')
plt.ylabel('x(mm)')
plt.show

#Phase in pi units
ph=np.transpose(1+np.angle(new_data)/np.pi)

#Draw Phase
plt.figure(3)
plt.imshow(ph,extent=[0,init.Zmax,-Xmax*1000,Xmax*1000])
plt.colorbar()
plt.title("Phase(π units)")
plt.xlabel('z(m)')
plt.ylabel('x(mm)')
plt.show

```

Appendix B

Efficient code of Python for Gaussian and Ring-Airy 2D propagation in free space or in the presence of obstacles:

```
#Angular spectrum Gaussian and Ring-Airy 2D propagation in free space or in the
#presence of obstacles

import math
import numpy as np
from scipy.special import airy
import datetime
import matplotlib.pyplot as plt

from sympy import exp, I, pi
from tempfile import TemporaryFile

outfile = TemporaryFile()

import Angular_spectrum_initialization_2D_dpapa_obstacles as init

print('Estimated      Ring      Airy      focus      position:      {}
m'.format(4*np.pi*init.w0**2/init.lamda*np.sqrt(init.r0/init.w0+1)))

# Auxilary functions

# Rectangular function
def rect(x):
    if np.abs(x) < 0.50:
        dummy=1.0
    else:
        dummy=0.0
    return dummy
vrect=np.vectorize(rect)

def RectWindow(Xs,Ys,Nx,Ny,X0,Y0,WidthX,WidthY):
    dummy=np.fromfunction(lambda di, dj: vrect((Xs-X0)/WidthX)*vrect((Ys-
Y0)/WidthY),(Nx,Ny),dtype=int)
    return dummy

#Hole function
def HoleWindow(Xs,Ys,Nx,Ny,X0,Y0,WidthX):
    dr=np.sqrt((Xs-X0)**2+(Ys-Y0)**2)/WidthX
    dummy=np.fromfunction(lambda di,dj: vrect(dr),(Nx,Ny),dtype=int)
    return dummy

#Beam definitions

#Gaussian beam definition with parameter FWHM wg
def Gaussian(Xs,Ys,Nx,Ny,wg):
    dummy=np.full((Nx, Ny), -4*math.log(2)/wg**2, dtype=np.complex)
    return np.exp(dummy*(Xs**2+Ys**2))
```

```

#Ring-Airy beam definition
def Ai(x):
    (ai, ai_prime, bi, bi_prime) = airy(x)
    return ai

def RingAiry(Xs,Ys,Nx,Ny,w0,r0,alpha):
    dr=(r0-np.sqrt(Xs**2+Ys**2))/w0
    dexp=np.exp(alpha*dr,dtype=np.complex)
    dai=np.fromfunction(lambda di,dj: Ai(dr[di,dj])/Ai(-1.), (Nx,Ny),dtype=int)
    return dai*dexp

#code diagnostics
start_Time = datetime.datetime.now()

#physical parameters
k0=(2*math.pi)/init.lamda #evaluation of wavenumber
w0=float(init.wg/math.sqrt(4*math.log(2))) #evaluation of beam waist
zR=float(math.pi*(w0)**2/init.lamda) #evaluation of confocal #parameter

Xmax=float(init.window/2) #Maximum x value
Ymax=float(init.window/2) #Maximum y value

dx=float(init.window/init.Nx) #x resolution (meters/pixel)
dy=float(init.window/init.Ny) #y resolution (meters/pixel)

dz=float(init.Zmax/init.Nz) #z resolution (meters/step)
dkx=float(math.pi/Xmax) #k space resolution (meters^-1/pixel) in x #direction
dky=float(math.pi/Ymax) #k space resolution (meters^-1/pixel) in y #direction

kxmax=float(dkx*init.Nx/2) #Maximum spatial frequency in x #direction
kymax=float(dky*init.Ny/2) #Maximum spatial frequency in y #direction

#preparation of x,y and kx,ky space lists
Xs,Ys=np.meshgrid(np.arange(-Xmax,Xmax,dx),np.arange(-Ymax,Ymax,dy))
Kx,Ky=np.meshgrid(np.arange(-kxmax, kxmax, dkx),np.arange(-kymax, kymax,
dky))

#preparation of obstacle screens
dObstPos=round(init.ObstacleZPosition/dz)
#ObstacleXYPosition=np.sqrt((init.ObstacleXPosition)**2+(init.ObstacleYPosition)*
*2)

if init.ObstacleType=="Aperture":
    if init.ObstacleShape=="Rect":

dObst=RectWindow(Xs,Ys,init.Nx,init.Ny,init.ObstacleXPosition,init.ObstacleYPosi
tion,init.ObstacleWidth/2,init.ObstacleWidth/2)
        elif init.ObstacleShape=="Disk":

dObst=HoleWindow(Xs,Ys,init.Nx,init.Ny,init.ObstacleXPosition,init.ObstacleYPosi
tion,init.ObstacleWidth/2)
        else:

```

```

dObst=RectWindow(Xs,Ys,init.Nx,init.Ny,init.ObstacleXPosition,init.ObstacleYPosition,init.ObstacleWidth/2,init.ObstacleWidth/2)

elif init.ObstacleType=="Block":
    if init.ObstacleShape=="Rect":

dObst=RectWindow(Xs,Ys,init.Nx,init.Ny,init.ObstacleXPosition,init.ObstacleYPosition,init.ObstacleWidth,init.ObstacleWidth)
    dObst=np.ones_like(dObst)-dObst
    elif init.ObstacleShape=="Disk":

dObst=HoleWindow(Xs,Ys,init.Nx,init.Ny,init.ObstacleXPosition,init.ObstacleYPosition,init.ObstacleWidth)
    dObst=np.ones_like(dObst)-dObst
    else:

dObst=RectWindow(Xs,Ys,init.Nx,init.Ny,init.ObstacleXPosition,init.ObstacleYPosition,init.ObstacleWidth,init.ObstacleWidth)
    dObst=np.ones_like(dObst)-dObst

elif init.ObstacleType=="Glass":
    dphisor=(1*2*np.pi/init.lamda)*init.ObstacleThickness*init.GlassRefrIndex

    if init.ObstacleShape=="Rect":

dObst=RectWindow(Xs,Ys,init.Nx,init.Ny,init.ObstacleXPosition,init.ObstacleYPosition,init.ObstacleWidth/2,init.ObstacleWidth/2)
    dObst=np.ones_like(dObst)-dObst
    dObst=np.exp(dphisor*dObst,dtype=np.complex)

    elif init.ObstacleShape=="Disk":

dObst=HoleWindow(Xs,Ys,init.Nx,init.Ny,init.ObstacleXPosition,init.ObstacleYPosition,init.ObstacleWidth/2)
    dObst=np.ones_like(dObst)-dObst
    dObst=np.exp(dphisor*dObst,dtype=np.complex)
    else:

dObst=RectWindow(Xs,Ys,init.Nx,init.Ny,init.ObstacleXPosition,init.ObstacleYPosition,init.ObstacleWidth/2,init.ObstacleWidth/2)
    dObst=np.ones_like(dObst)-dObst
    dObst=np.exp(dphisor*dObst,dtype=np.complex)

else:
    dObstPos=-100
    dObst=np.full((init.Nx,init.Ny), 1, dtype=int)

#create a discretized Gaussian or Ring-Airy beam
DBeam=Gaussian(Xs,Ys,init.Nx, init.Ny,init.wg)
DBeam=RingAiry(Xs,Ys,init.Nx,init.Ny,init.w0,init.r0,init.alpha)

#Propagators
# paraxial propagator
dpr=np.full((init.Nx, init.Ny), -1*(init.lamda/(4.*np.pi))*dz, dtype=np.complex)

```

```

Tpr=np.exp(dpr*(Kx**2+Ky**2))

# Prepare chess pattern
Chess=np.fromfunction(lambda di, dj: (-1)**(di+dj), (init.Nx, init.Ny), dtype=int)

#Main iteration routine

#initialize lists to store results
if dObstPos==0:
    DBeam=DBeam*dObst

YSlicePos=round((init.YSlice+Ymax)/dy)+1
Vis2=np.empty(shape=[init.Nz+1,init.Nx],dtype=np.complex128)

lmax=np.empty(shape=[init.Nz+1],dtype=np.float64)
gmax=np.amax(DBeam)
lmax[0]=abs(gmax)**2
Vis2[0]=DBeam[YSlicePos]

#iteration core
for dj in range (1,init.Nz+1):
    if dj==dObstPos:
        DBeam=DBeam*dObst          # apply obstacle
        if init.PreviewOn:         # visualize obstacle effect
            plt.close("all")
            plt.figure(figsize=(12,4.5))
            plt.subplot(121)
            plt.title('Amplitude')
            plt.xlabel('x (mm)')
            plt.ylabel('y (mm)')
            plt.imshow(abs(DBeam),extent=[-Xmax*1000,Xmax*1000,-
Ymax*1000,Ymax*1000],aspect='auto')
            plt.colorbar()

            plt.subplot(122)
            plt.xlabel('x (mm)')
            plt.ylabel('y (mm)')
            plt.title('Phase/pi')
            plt.imshow(np.angle(DBeam)/np.pi,extent=[-Xmax*1000,Xmax*1000,-
Ymax*1000,Ymax*1000],aspect='auto')
            plt.colorbar()
            plt.show

        FBeam0=np.fft.fft2(DBeam*Chess)
        DBeam=np.fft.ifft2(FBeam0*Tpr)*Chess
        lmax[dj]=np.amax(abs(DBeam)**2)
        Vis2[dj]=DBeam[YSlicePos]

print('Propagation executed in: {}'.format(datetime.datetime.now() - start_Time))

mydate =datetime.datetime.now().strftime("%d-%m-%y-%H-%M-%S")

#Save Vis2 elements in a Results_1{Time_Stamp}.txt file
np.savetxt('Results_1.txt',Vis2.view(float))

```

```

#Save I_max elements in a Results_I_max{Time_Stamp}.txt file
np.savetxt('Results_I_max.txt',I_max)

#Read Results Gaussian and Ring-Airy 2D propagation in free space or in the
#presence of obstacles python file

import matplotlib.pyplot as plt
import numpy as np

from tempfile import TemporaryFile
outfile = TemporaryFile()

import Angular_spectrum_initialization_2D_dpapa_obstacles as init

new_data = np.loadtxt('Results_I.txt').view(complex)
new_data1=np.loadtxt('Results_I_max.txt')
Xmax=float(init.window/2)

#Visualization

#Max(Intensity(x)) as a function of z
plt.close("all")
Zi=np.linspace(0,init.Zmax,init.Nz+1)
plt.figure(1)
plt.plot(Zi,new_data1)
plt.title("Peak intensity")
plt.xlabel('z (m)')
plt.ylabel('I_max')

#Intensity
iml=np.transpose(abs(new_data)**2)

#Draw Intensity
plt.figure(2)
plt.imshow(iml,extent=[0,init.Zmax,-Xmax*1000,Xmax*1000],aspect='auto')
plt.colorbar()
plt.title("Intensity")
plt.xlabel('z(m)')
plt.ylabel('x(mm)')

#Phase in pi units
ph=np.transpose(1+np.angle(new_data)/np.pi)

#Draw Phase
plt.figure(3)
plt.imshow(ph,extent=[0,init.Zmax,-Xmax*1000,Xmax*1000],aspect='auto')
plt.colorbar()
plt.title("Phase(pi units)")
plt.xlabel('z(m)')
plt.ylabel('x(mm)')
plt.show

```

BIBLIOGRAPHY

1. Efremidis, N.K. and D.N. Christodoulides, *Abruptly autofocusing waves*. Opt. Lett., 2010. **35**(23): p. 4045-4047.
2. Papazoglou, D.G., et al., *Tunable intense Airy beams and tailored femtosecond laser filaments*. Physical Review A, 2010. **81**(6): p. 061807.
3. Papazoglou, D.G., et al., *Observation of abruptly autofocusing waves*. Opt. Lett., 2011. **36**(10): p. 1842-1844.
4. Panagiotopoulos, P., et al., *Sharply autofocused ring-Airy beams transforming into non-linear intense light bullets*. Nat Commun, 2013. **4**: p. 2622.
5. Siviloglou, G.A. and D.N. Christodoulides, *Accelerating finite energy Airy beams*. Opt. Lett., 2007. **32**(8): p. 979-981.
6. Siviloglou, G.A., et al., *Observation of Accelerating Airy Beams*. Physical Review Letters, 2007. **99**(21): p. 213901.
7. Eugene Hecht, "*Optics*", 4th edition. Addison Wesley, San Francisco, 2002, p.:104-106.
8. Joseph W. Goodman, "*Introduction to Fourier Optics*". The McGraw-Hill Companies, Second Edition, (1996), Chapter 3.10, p.:55-61.
9. David G. Voelz, "*Computational Fourier Optics: A MATLAB Tutorial*". SPIE Tutorial Texts Vol.TT89, 2011, Chapter 5, p.:63-87.
10. Okan K. Ersoy, "*Diffraction, Fourier Optics and Imaging*". John Wiley & Sons, Inc., Hoboken, New Jersey, 2007, Chapters 4,10.
11. https://www.photonics.ethz.ch/fileadmin/user_upload/Courses/EM_FieldsAndWaves/AngularSpectrumRepresentation.pdf
12. https://www.photonics.ethz.ch/fileadmin/user_upload/Courses/PhysicalOpticsII/notes13.pdf
13. Papazoglou, D.G., Notes in Course OpticsI, Optiki_I_HandNotes.pdf